

[Handwritten scribble]

① LEVEL II



CHARACTERISTICS OF A STEADILY OPERATING METAL COMBUSTOR

AD A104659

Technical Report

DTIC
ELECTE
SEP 25 1981
S B

Sponsored by

Advanced Research Projects Agency
ARPA Order No. 2150
Program Code No. 2N10
Contract No. N00600-74-C-0033

Prepared by
E. G. Groff, G. M. Faeth

The Pennsylvania State University
College of Engineering
Department of Mechanical Engineering
University Park, Pennsylvania

August, 1976

DISTRIBUTION STATEMENT A
Approved for public release;
Distribution Unlimited

81 9 25 056

DTIC FILE COPY

UNCLASSIFIED

SECURITY CLASSIFICATION OF THIS PAGE (When Data Entered)

REPORT DOCUMENTATION PAGE		READ INSTRUCTIONS BEFORE COMPLETING FORM
1. REPORT NUMBER	2. GOVT ACCESSION NO.	3. RECIPIENT'S CATALOG NUMBER
	AD-A104 659	
4. TITLE (and Subtitle)	5. TYPE OF REPORT & PERIOD COVERED	
Characteristics of a Steadily Operating Metal Combustor.	Interim report Sep 73 to May 76	
	6. PERFORMING ORG. REPORT NUMBER	
7. AUTHOR(s)	8. CONTRACT OR GRANT NUMBER(s)	
Edward G. Groff Gerard M. Faeth	N00600-74-C-0033 ARPA Order-2150	
9. PERFORMING ORGANIZATION NAME AND ADDRESS	10. PROGRAM ELEMENT, PROJECT, TASK AREA & WORK UNIT NUMBERS	
Department of Mechanical Engineering The Pennsylvania State University University Park, Penna. 16802	62105E, 2N10 Other DOD-ARPA, 2724-510-50	
11. CONTROLLING OFFICE NAME AND ADDRESS	12. REPORT DATE	
Defense Advanced Research Projects Agency 1400 Wilson Blvd., Arlington, Va. 22209	August 1976	
	13. NUMBER OF PAGES	
	156	
14. MONITORING AGENCY NAME & ADDRESS (if different from Controlling Office)	15. SECURITY CLASS. (of this report)	
David W. Taylor Naval Ship R&D Center Annapolis, Maryland 21402	U	
	15a. DECLASSIFICATION/DOWNGRADING SCHEDULE	
16. DISTRIBUTION STATEMENT (of this Report)		
Approved for Public Release; distribution unlimited.		
17. DISTRIBUTION STATEMENT (of the abstract entered in Block 20, if different from Report)		
18. SUPPLEMENTARY NOTES		
A Ph.D. Thesis in Mechanical Engineering, directed by Gerard M. Faeth		
19. KEY WORDS (Continue on reverse side if necessary and identify by block number)		
Liquid Metal Combustor; Liquid Metal Reactor		
20. ABSTRACT (Continue on reverse side if necessary and identify by block number)		
Over		

DD FORM 1 JAN 73 1473

EDITION OF 1 NOV 65 IS OBSOLETE
S/N 0102-014-6601

SECURITY CLASSIFICATION OF THIS PAGE (When Data Entered)

Enclosure (1)
DTNSRDC ltr 2721:DEI 4330:3

UNCLASSIFIED

SECURITY CLASSIFICATION OF THIS PAGE (When Data Entered)

ABSTRACT. The overall objective of the present study was to investigate analytically and experimentally the characteristics of a steadily operating liquid metal thermal energy source employing the lithium-sulfur hexafluoride reactant combination. A steady metal combustor apparatus was designed, fabricated and operated in the temperature range of 1110 to 1255°K with power outputs ranging up to 25.2 kW. Steady-state conditions were established by continuously supplying fuel and oxidizer to the reaction chamber while continuously removing the reaction products through a trap arrangement in the bottom of the chamber. Procedures were developed to obtain bath liquid density values and to remove and analyze samples by wet chemical methods. Thermal performance data were generated at a bath temperature of $1197 \pm 3^\circ\text{K}$ over a range of load conditions. The capability of the system to operate under variable load range, idling and restart conditions was also demonstrated for operating times of 10 hours. No corrosion problems were observed with the type 316 stainless steel components. Thermal efficiencies ranged from 86.4 to 84.0% in the bath temperature range of 1110 to 1250°K. Fuel utilization exceeded 99% at 1200°K because the fuel solubility in the reaction products is less than 0.5% by mole fraction. A thermodynamic model for the reaction permitted calculation of liquid phase solubilities, liquid phase densities, gas phase partial pressures, and thermal performance values which were in good agreement with experimental results.

Accession For	
NTIS GRA&I	<input checked="checked" type="checkbox"/>
DTIC TAB	<input type="checkbox"/>
Unannounced	<input type="checkbox"/>
Justification	
By	
Distribution/	
Availability Codes	
Dist	Avail and/or Special
A	

UNCLASSIFIED

SECURITY CLASSIFICATION OF THIS PAGE (When Data Entered)

CHARACTERISTICS OF A STEADILY OPERATING METAL COMBUSTOR

Technical Report

August 1976

Sponsored by
Advanced Research Projects Agency
ARPA Order No. 2150
Program Code No. 2N10
Contract No. N00600-74-C-0033

The views and conclusions contained in this document are those of the authors and should not be interpreted as necessarily representing the official policies, either expressed or implied, of the Advanced Research Projects Agency of the U.S. Government.

Prepared by

E. G. Groff, telephone (814) 865-0901
G. M. Faeth, telephone (814) 865-3743

Mechanical Engineering Department
The Pennsylvania State University
University Park, Pennsylvania 16802

ACKNOWLEDGMENT

This research was supported by David W. Taylor Naval Ship Research and Development Center, Annapolis Laboratory, as Technical Agent for Defense Advanced Research Projects Agency, under contract number N00600-74-C-0033.

TABLE OF CONTENTS

	<u>Page</u>
ACKNOWLEDGMENTS	11
LIST OF TABLES	vii
LIST OF FIGURES	viii
NOMENCLATURE.	x
I. INTRODUCTION	1
1.1 General Statement of the Problem.	1
1.2 Description of the Process.	2
1.2.1 Reaction Characteristics	2
1.2.2 Pot-Type Combustor Concept	3
1.2.3 Steady Combustor Concept	7
1.3 Previous Related Studies.	9
1.3.1 Thermodynamics	9
1.3.2 Liquid Metal Combustion Studies.	11
1.4 Specific Statement of the Problem	12
II. THEORETICAL CONSIDERATIONS	14
2.1 Existing Theory	14
2.2 The Thermodynamic Model	18
2.2.1 Assumptions.	18
2.2.2 Gibbs Free Energy of Mixing.	18
2.2.3 Activity Coefficients.	22
2.2.4 Mixture Enthalpy	23
2.2.5 Mixture Density.	24
2.2.6 Gas Phase.	25
2.2.7 Summary of the Thermodynamic Model	28
2.3 Prediction of Liquid Phase Solubilities of a Steady Metal Combustor	29
III. DETERMINATION OF THE THERMODYNAMIC MODEL PARAMETERS. . .	31
3.1 Introduction.	31
3.2 Lithium-Lithium Fluoride Binary	31
3.3 Lithium-Lithium Sulfide Binary.	33
3.4 Lithium Fluoride-Lithium Sulfide Binary	39
3.5 Summary	43

TABLE OF CONTENTS (CONTINUED)

	<u>Page</u>
IV. EXPERIMENTAL APPARATUS AND PROCEDURE	44
4.1 Introduction.	44
4.2 Air-Cooled Combustor Apparatus.	45
4.2.1 Reaction Chamber and Heat Exchanger.	45
4.2.2 Fuel Pump and Fuel Tank.	51
4.2.3 Product Collection Tank.	52
4.2.4 Exhaust Filter	54
4.2.5 Control System	54
4.3 Radiative Combustor Apparatus	56
4.3.1 Reaction Chamber	56
4.3.2 Product Collection Tank.	57
4.4 Instrumentation	57
4.4.1 Flow Measurement	57
4.4.2 Temperature Measurement.	59
4.4.3 Fuel Level Measurement	59
4.4.4 Sampling System.	60
4.5 Experimental Procedure.	61
4.5.1 Reactants.	61
4.5.2 Pre-Test Preparation Procedure	61
4.5.3 Normal Operating Procedure	61
4.5.4 Post-Test Shutdown Procedure	63
4.5.5 Bath Sampling Procedure.	63
4.5.6 Bath Sample Analysis Procedure	64
4.5.7 Bath Density Measurement Procedure	65
4.5.8 Thermal Performance Measurement Procedure.	66
V. EXPERIMENTAL AND THEORETICAL RESULTS	68
5.1 General Experimental Observations	68
5.1.1 Radiative Combustor Tests.	68
5.1.2 Air-Cooled Combustor Tests	72
5.1.3 Nature of the Reaction Products.	77
5.2 Liquid Phase Solubility Results	80
5.3 Liquid Phase Density Results.	87
5.4 Gas Phase Partial Pressure Results.	90

TABLE OF CONTENTS (CONTINUED)

	<u>Page</u>
5.5 Oxidizer Utilization Efficiency Results	93
5.6 Thermal Performance Results	93
5.6.1 Energy Release	93
5.6.2 Energy Utilization	96
5.6.3 Bath Temperature Effects on System Performance.	98
VI. SUMMARY AND CONCLUSIONS.	101
6.1 Summary	101
6.2 Conclusions	103
6.3 Recommendations for Further Study	104
BIBLIOGRAPHY.	106
APPENDIX A: COMPUTER PROGRAM AND NEWTON-RAPHSON METHOD USED TO SOLVE THE THERMODYNAMIC MODEL EQUATIONS.	111
APPENDIX B: THERMOCHEMICAL PROPERTY DATA	128
B.1 Thermodynamic Properties of Li(s,l,g) , $\text{Li}_2(\text{g})$, LiF(s,l,g) , $\text{Li}_2\text{F}_2(\text{g})$, $\text{Li}_3\text{F}_3(\text{g})$, and $\text{SF}_6(\text{g})$	128
B.2 Thermodynamic Properties of $\text{Li}_2\text{S(s,l,g)}$	128
B.2.1 Thermodynamic Properties of $\text{Li}_2\text{S(s)}$	128
B.2.2 Thermodynamic Properties of $\text{Li}_2\text{S(l)}$	129
B.2.3 Thermodynamic Properties of $\text{Li}_2\text{S(g)}$	131
B.3 Densities of Li(l) , LiF(l) and $\text{Li}_2\text{S(l)}$	138
APPENDIX C: THEORETICAL DEVELOPMENT OF EXPRESSIONS USED TO DETERMINE THERMODYNAMIC MODEL PARAMETERS	140
C.1 Expressions Relating to Solid-Liquid Equilibria	140
C.2 Expressions Relating to Two Equilibrated Liquid Phases.	143
APPENDIX D: BATH SAMPLE ANALYSIS PROCEDURE	145
D.1 Lithium Fluoride and Lithium Sulfide Determination.	145
D.1.1 Sulfide Separation	145
D.1.2 Lithium Sulfide Determination.	147
D.1.3 Lithium Fluoride Determination	148

TABLE OF CONTENTS (CONTINUED)

	<u>Page</u>
D.2 Lithium Determination	148
D.2.1 Product-Rich Samples	149
D.2.2 Fuel-Rich Samples.	150
APPENDIX E: OXIDIZER UTILIZATION TESTS	152
E.1 Apparatus and Procedure	152
E.2 Results	153
APPENDIX F: APPARATUS AND PROCEDURE FOR INVESTIGATING THE WET-TANK PRODUCT COLLECTION METHOD	154
F.1 Apparatus	154
F.2 Procedure	154
F.3 Results	156

LIST OF TABLES

<u>Table</u>	<u>Title</u>	<u>Page</u>
1	Summary of Radiative Combustor Tests.	69
2	Summary of Air-Cooled Combustor Tests	73
3	Fuel-Rich Liquid Solubility Data.	82
4	Product-Rich Liquid Solubility Data	85
5	Bath Liquid Density Data.	89
6	Vibrational Frequency Data for Triatomic and Diatomic Molecules.	132
7	Effects of Various Assumptions on the Thermodynamic Properties.	137

LIST OF FIGURES

<u>Figure</u>	<u>Caption</u>	<u>Page</u>
1	Pot-Type Combustor Concept.	4
2	Steady Combustor Concept.	8
3	Lithium-Lithium Fluoride Binary Parameters.	32
4	Lithium-Lithium Fluoride Solubility Results	34
5	Lithium-Lithium Sulfide Solubility Results.	36
6	Lithium Fluoride-Lithium Sulfide Solubility Results . .	41
7	Schematic of Air-Cooled Steady Combustor Apparatus. . .	46
8	Photograph of Air-Cooled Steady Combustor Apparatus . .	47
9	Sketch of the Coaxial Injector.	50
10	Performance Curves of the Argon Lift Pump	53
11	Flow Control System	55
12	Radiative Combustor Run Data (Test LSR-8)	71
13	Air-Cooled Combustor Run Data (Test PPC-9).	76
14	Air-Cooled Combustor Run Data (Test PPC-10)	78
15	Photograph of Reaction Products	79
16	Photograph of Wet-Tank Reaction Products.	79
17	Fuel-Rich Liquid Solubilities	81
18	Product-Rich Liquid Solubilities.	84
19	Bath Densities.	88
20	Theoretical Gas Phase Partial Pressures	91
21	Wick-Type Combustor Total Pressure Results.	92
22	Performance Results	94
23	Energy Flow Diagram for Apparatus	97
24	Effects of Bath Temperature on System Performance . . .	99

LIST OF FIGURES (CONTINUED)

<u>Figure</u>	<u>Caption</u>	<u>Page</u>
25	Distillation Apparatus.	146
26	Wet-Tank Product Collection Apparatus	155

NOMENCLATURE

<u>Symbol</u>	<u>Description</u>
a	Thermodynamic model parameter, Equation (C.12), (dimensionless)
a_i	Chemical activity, Equation (2.6), (dimensionless)
A	Thermodynamic model parameter, Equation (3.3), (J/mole)
A_{ij}	Thermodynamic model parameter, Equation (2.12), (J/mole)
A_{ij}'	Thermodynamic model parameter, Equation (2.12), (J/cc)
b	Thermodynamic model parameter, Equation (C.12), ($^{\circ}\text{K}^{-1}$)
b_i	Thermodynamic model parameter, Equation (2.10), (cc/mole)
B	Thermodynamic model parameter, Equation (3.3), (J/mole- $^{\circ}\text{K}$)
B_i	Thermodynamic model parameter, Equation (2.13), (dimensionless)
B'	Rotational constant, Equation (B.17), (cm^{-1})
c	Speed of light, Equation (B.13), (2.99793×10^{10} cm/sec)
C	Generic constant, Equation (A.11), (J/mole)
c_p	Specific heat at constant pressure, Equation (C.9), (J/mole- $^{\circ}\text{K}$)
D_{ij}	Matrix coefficient, Equation (A.13), (J/mole or dimensionless)
D'	Products of moments of inertia, Equation (B.22), ($\text{gm}^3\text{-cm}^6$)
f	Molar Gibbs free energy, Equation (2.1), (J/mole)
F	Gibbs free energy, Equation (2.4), (J)
G_i	Matrix coefficient, Equation (A.13), (J/mole, or dimensionless)
h	Molar enthalpy, Equation (2.3), (J/mole)
h'	Planck's constant, Equation (B.13), (6.62517×10^{-34} J-sec)
H	Enthalpy, Equation (2.21), (J)
I	Moment of inertia, Equation (B.17), (gm-cm^2)

NOMENCLATURE (CONTINUED)

<u>Symbol</u>	<u>Description</u>
k	Boltzmann's constant, Equation (B.13), $(1.38044 \times 10^{-23} \text{ J/}^\circ\text{K})$
\bar{k}_i	Relative molal heat content, Equation (C.7), (J/mole)
K_i	Equilibrium constant, Equation (2.36), (dimensionless)
M_i	Molecular weight, Equation (2.31), (gm/mole)
n_i	Number of moles of a component, Equation (2.1), (mole)
N_i	Generic chemical species symbol, Equation (2.35)
P_i	Partial pressure, Equation (2.40), $(\text{atm} = 1.01325 \text{ bar})$
P	Pressure, Equation (2.2), (bar)
R	Universal gas constant, Equation (B.5), $(8.3147 \text{ J/mole-}^\circ\text{K})$
s	Molar entropy, Equation (2.3), $(\text{J/mole-}^\circ\text{K})$
S	Entropy, Equation (2.24), $(\text{J/}^\circ\text{K})$
T	Temperature, Equation (2.1), $(^\circ\text{K})$
u_i	Defined molecular vibrational constant, Equation (B.9), (dimensionless)
w_i	Natural logarithm of mole fraction, Equation (A.2), (dimensionless)
x_i	Mole fraction, Equation (2.8), (dimensionless)
X_i	Generic constant, Equation (3.4), (J/mole)
y_i	Mole fraction, Equation (2.43), (dimensionless)
Y_i	Generic constant, Equation (3.4), (J/mole)
z_i	Natural logarithm of mole fraction, Equation (A.1), (dimensionless)
γ_i	Activity coefficient, Equation (2.2), (dimensionless)
Γ_i	Reference state chemical activity, Equation (2.8), (dimensionless)
ω_i	Vibrational degeneracy, Equation (B.9), (dimensionless)

NOMENCLATURE (CONTINUED)

<u>Symbol</u>	<u>Description</u>
ω_e	Diatomic molecule vibrational constant, Table 6, (cm^{-1})
$\omega_e x_e$	Diatomic molecule anharmonicity constant, Table 6, (cm^{-1})
σ	Symmetry number, Equation (B.18), (dimensionless)
θ	Defined temperature difference, Equation (C.11), ($^{\circ}\text{K}$)
ν_i	Molecular vibrational frequency, Equation (B.9), (cm^{-1})
ν_i'	Stoichiometric coefficient of reactants, Equation (2.35), (dimensionless)
ν_i''	Stoichiometric coefficient of products, Equation (2.35), (dimensionless)
ρ_i	Density, Equation (2.31), (kg/m^3)

Subscripts

b	Boiling point
f	Fusion point
i	Generic subscript usually denoting species i
j	Generic subscript usually denoting species j
k	Generic subscript
A, B, C	Molecular rotational axes
T	Total quantity
T_f	Fusion temperature
T_b	Boiling temperature
compound	Participating compounds
elements	Participating elements
form	Formation from elements in standard states
ideal	Contribution from ideal mixing
mix	Contribution from mixing

NOMENCLATURE (CONTINUED)

<u>Subscripts</u>	<u>Description</u>
rot	Rotational contribution
trans	Translational contribution
vib	Vibrational contribution
o	Initial value
<u>Superscripts</u>	
o	Pure component in standard state
E	Excess thermodynamic quantity
-	Partial molal quantity
'	Generic superscript
"	Generic superscript
T _f	Standard heat of fusion at fusion point

ABSTRACT

Two metal combustor system concepts employing the lithium-sulfur hexafluoride reactant combination are currently under development. One concept is the batch or pot-type combustor (where fuel and combustion products remain within the combustion chamber), and the other is the steady combustor (where fuel continuously enters and products continuously leave the combustion chamber). Both concepts are desirable for application as a thermal energy source for underwater power systems utilizing closed thermodynamic cycles since the lithium-sulfur hexafluoride reactant combination has a high energy density and no requirement for combustion product exhaust to the ambient environment. The steady combustor concept is advantageous for long duration operation, where the volume of the fuel inventory is large in comparison to the volume required to provide sufficient heat exchanger area and reaction volume. In this situation, the use of a pot-type combustor requires the presence of an excessive quantity of fuel in the active zone of the combustor.

This report documents the results of a developmental program concerning steady metal combustors. Two combustors are described which have demonstrated operation for periods of up to ten hours at power levels up to 25 kW. The thermodynamic characteristics of the ternary immiscible liquid mixture present in the reaction chamber were examined analytically by developing a theoretical model for the mixture, and experimentally by generating density and solubility data. The model permits prediction of system characteristics at operating conditions not examined experimentally, and is useful in the analyses

of other combustor concepts. The energy release rate of the system was measured and compared to the theoretical value.

CHAPTER I

INTRODUCTION

1.1 General Statement of the Problem

The increased use of closed thermodynamic heat-power cycles for mechanical power in underwater applications has motivated development of thermal energy sources. A thermal energy source is a source of heat at an elevated temperature, and can be provided by exothermic nuclear or chemical reactions. A thermal energy source can be combined with various closed thermodynamic heat-power cycles (e.g., Rankine, Brayton, Stirling, etc.) to provide a mechanical or electrical power system. The objective of the present study was to investigate both analytically and experimentally the characteristics of a steadily operating metal combustor thermal energy source.

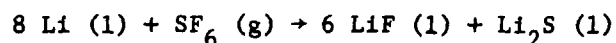
Features which make a thermal energy source attractive for underwater applications include the following: a) the reactant combination should have a high energy density on both a mass and volumetric basis; b) the reaction products should be nongaseous with a volume approximately equal to that of the reactants; c) the reaction process should be controllable within temperature limits of available construction materials; d) the reactants and products should be nontoxic; e) the reactants and products should be compatible with the construction materials; f) the reactants should be stable and storable for extended periods of time; and g) the reactants should be

inexpensive. Features (a) and (b) are particularly important for deep depth operation, where large vehicle volumes and the design of product exhaust systems for gaseous combustion products become problematical.

Thermal energy sources having these features are provided by the general class of chemical reactions between alkali metals and the halogen or halogenated gases. The particular member of this class considered in the present study is the reaction between lithium metal and sulfur hexafluoride gas, proposed by Pauliukonis [1]. The lithium-sulfur hexafluoride system was chosen due to its extremely good mass and volumetric energy density and the nontoxic nature of the oxidant. Van der Sluijs [2] reviewed the many possible reactant combinations and concluded that the combination chosen for study is the best for application as an underwater thermal energy source.

1.2 Description of the Process

1.2.1 Reaction Characteristics. The reaction is conducted in a combustion chamber containing the molten fuel. The oxidizer enters the chamber as a gas through an injector. The overall stoichiometry of the lithium-sulfur hexafluoride reaction is



The products of the reaction are liquids for the usual range of operating conditions, i.e., bath temperatures greater than approximately 1075°K. The volume of the products is approximately 96% of the volume of the original fuel at a temperature of 1200°K.

Characteristic of the phase equilibria between liquid alkali metals and their salts is the formation of an immiscible liquid region.

At normal operating temperatures of the combustor, 1090°K-1260°K, the combustor bath is within this immiscible liquid region, and the bath splits into two phases. The fuel-rich phase has a molar concentration of fuel greater than 95%, and the product-rich phase has a molar concentration of products greater than 99%. The density of the product-rich phase is more than three times that of the fuel-rich phase and the products settle under the action of gravity to the bottom of the combustion chamber where they can be allowed to accumulate (pot-type combustor concept), or can be continuously removed while fuel is continuously added (steady combustor concept). The chemical energy released by the reaction is transferred to the power cycle by means of heat exchanger surfaces located at the walls of the combustion chamber.

1.2.2 Pot-Type Combustor Concept. The pot-type combustor is illustrated schematically in Figure 1. The combustion chamber is sized to carry the entire fuel inventory for the particular application. Operation is terminated when all the fuel is consumed and the combustor is filled with reaction products. The oxidizer is introduced to the combustion chamber through an injector. Both single-passage injectors which can be cooled to decrease the susceptibility of the injector to corrosive attack by the oxidizer; and coaxial injectors, which utilize a secondary flow of argon gas in a shroud tube around the oxidizer core tube to prevent contact of the oxidizer with the outer injector parts, have been reported in the literature. In the case where a single-passage injector is used, the combustion chamber can be sealed and the chamber pressure will be equal to the

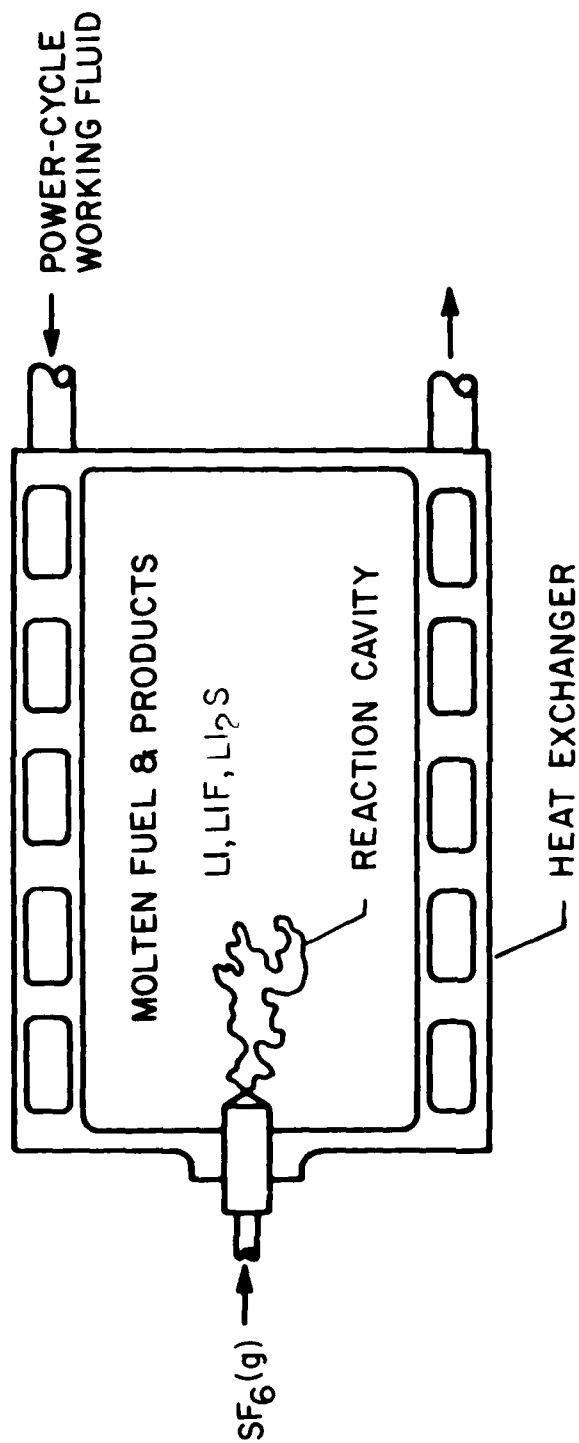


Figure 1 Pot-Type Combustor Concept

vapor pressure of the liquid mixture. In the case where a coaxial injector is used, the combustion chamber must be vented to remove the shroud argon flow and the combustion chamber pressure is controlled as desired. Thermal energy is transferred through the walls of the combustion chamber to the working fluid of the power cycle through the use of a heat exchanger which is usually integral with the combustion chamber walls.

Several pot-type combustor systems are discussed in the literature. The earliest documented design is described in a United States Patent by Percival [3], who proposed the use of Freon,* which contains fluorine, as the oxidizer. Distinguishing features of the design include submerged injection through a dispersion pipe containing multiple nozzles, and energy removal from the bath by a direct contact heat exchanger, where the working fluid for the heat engine cycle passes directly through the combustion chamber.

Uhlemann, Spigt and Hermans [4] have described the development of a pot-type metal combustor system employing lithium and sulfur hexafluoride for use with a Stirling engine. Bierman [5] has also discussed a lithium-sulfur hexafluoride combustor system to be used in conjunction with a Stirling engine. In this system the inside walls of the reaction chamber were covered with a capillary wick which was completely filled with lithium. The oxidizer was injected into the gas phase region of the chamber and reacted at the surface of the wick. In this manner, the reaction chamber walls were protected from corrosive attack by the oxidizer. The reaction products formed

*Registered trademark, E. I. duPont de Nemours and Company.

droplets on the surface of the wick and fell to the bottom of the reaction chamber. The energy of reaction was removed by a heat exchanger located behind the wick.

Mattavi, Heffner and Miklos [6] also discussed the use of metal combustion systems in combination with a Stirling heat engine. Several oxidizers were investigated including sulfur hexafluoride. The oxidizer was injected above the molten lithium surface for some tests; on other occasions a submerged injector was used. The authors presented system performance information in terms of system weight versus run length and average power level.

Van der Sluijs [2] presented a discussion of a lithium-sulfur hexafluoride combustion system to be used as the thermal energy source for a Stirling engine. The lithium fuel was contained in a reactor vessel along with a quantity of sodium, and the oxidizer was injected through a submerged injector. The injector design consisted of a orifice opening which could be closed by a needle. The needle position was controlled by the oxidizer supply pressure acting on a sealed piston, and on-off operation of the injector could be controlled by the position of an oxidizer control valve. The heat transport to the Stirling engine was accomplished by evaporation of the sodium contained in the reactor bath and subsequent condensation on the engine heater tubes. The condensed sodium was then transported back to the reactor bath using an electromagnetic pump.

Faeth and co-workers [7, 8] investigated pot-type combustors employing the lithium-sulfur hexafluoride reactant combination. Particular emphasis was placed on long term operation (order of hours) with highly variable thermal load requirements. Both vented and

unvented combustor configurations were studied. Various injector configurations were examined including cooled and uncooled single-passage injectors and coaxial injectors. Thermal energy was removed both by heating air as a working fluid and by direct radiation from the combustion chamber walls to the surroundings.

1.2.3 Steady Combustor Concept. For long duration operation, the volume of the fuel inventory can become large in comparison to the volume required to provide sufficient heat exchanger area and reaction volume. In this situation, the use of a pot-type combustor requires the presence of an excessive quantity of fuel in the active zone of the combustor. A large combustion chamber volume causes several problems: poor thermal response; excessive parasitic heat loss; structural difficulties of large-size high-temperature components; system size and weight penalties; potentially poor bath heat transfer characteristics; and potentially poor fuel utilization.

An improved approach over the pot-type combustor system for long-duration operation involves the steady combustor concept, illustrated schematically in Figure 2. In this case, the fuel and oxidizer enter the combustor and the products are drawn off in a continuous fashion. The size of the combustion chamber can be optimized with respect to heat exchanger area or reaction volume requirements -- whichever is limiting.

The operation of the steady combustor involves the use of the immiscibility characteristics of the fuel and product [9]. In the absence of strong stirring, the heavy product liquid settles to the bottom of the combustor where it is removed through a trap. Fuel

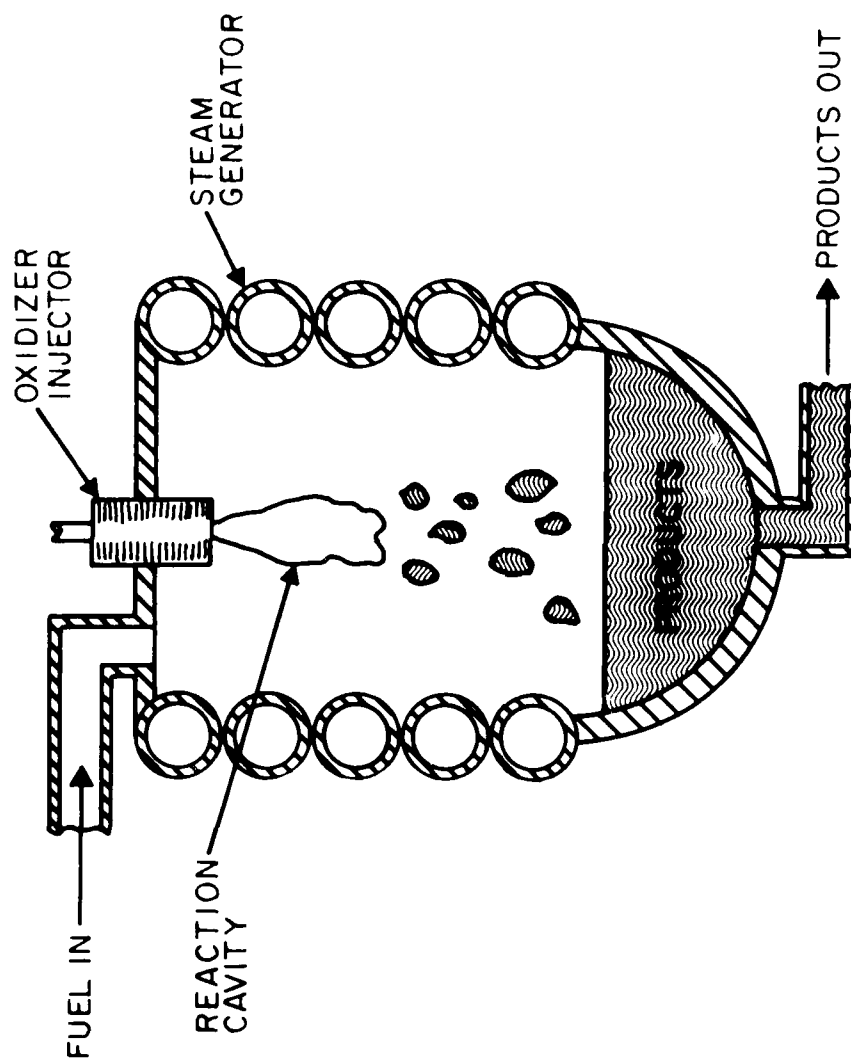


Figure 2 Steady Combustor Concept

can be added steadily, or intermittantly since a small change in product level in the trap can accommodate relatively large changes in combustor fuel level (since the product liquid density is approximately three times the density of the fuel liquid). Both single-passage and coaxial injectors can be used with the system. The thermal energy is removed by a heat exchanger installed at the combustion chamber walls. Details of the particular steady combustor to be used in the course of the present study will be described in Chapter IV.

A search of the literature revealed no previous studies concerning a steady metal combustor system other than the concept presented by Feath [9]. Preliminary work for this study is reported in References [7] and [8].

1.3 Previous Related Studies

1.3.1 Thermodynamics. The performance of the lithium-sulfur hexafluoride system in terms of energy release rate has been discussed in the literature. Van der Sluijs [2] presented an estimate of the thermal energy released by the reaction and investigated system performance for a pot-type combustor system. Biermann [5] presented performance information for a particular pot-type combustion chamber in terms of energy release rate per volume and per surface area of the combustion chamber. Mattavi, et al., [6] investigated the overall performance of a pot-type combustor system with respect to total system mass and system volume as a function of run length and average power requirements.

The results of the performance studies discussed above are generally limited in applicability to a particular combustor system,

and are not easily extended to the analyses of other systems. Another limitation is the lack of consideration of the thermodynamic properties of the liquid and gas phases present in the combustor. The thermodynamic information is important in analyses of all combustor systems. For example, knowledge of the fuel solubility in the product-rich phase is required since the fuel dissolved in the product potentially represents a fuel loss in the steady combustor concept and fuel unavailable for combustion in the pot-type combustor concept.

Information is available concerning the thermodynamic properties of a majority of the reactants and products in the lithium-sulfur hexafluoride reaction. The thermodynamic properties of sulfur hexafluoride, lithium fluoride and lithium are tabulated in the JANAF Thermochemical Tables [10]. The densities of lithium fluoride and lithium as a function of temperature are given by Janz [11] and Davison [12], respectively.

The information on lithium sulfide is less abundant. The heat of formation of solid lithium sulfide was calculated by Morris [13], and determined experimentally by Juza and Uphoff [14]. The melting and boiling points were determined experimentally by Cunningham, et al., [15] and Mott [16], respectively. The density of solid lithium sulfide at a temperature of 298°K has been reported by Mourlot [17], Zintl, et al., [18], and Beck [19].

Dworkin, Bronstein, and Bredig [20] presented solubility data for the immiscible liquid region of the lithium-lithium fluoride system. The lithium-lithium sulfide and lithium fluoride-lithium sulfide systems have received less attention. Faeth [21] investigated the freezing point depression of pure lithium upon the addition of

lithium sulfide. These findings were supplemented by the investigations of Cunningham, et al., [15]. Faeth [21] also determined the liquidus line representing the freezing point depression of pure lithium fluoride upon the addition of lithium sulfide.

Various thermodynamic models exist for multicomponent solutions and will be discussed in Chapter II. Avery [22] employed the van Laar regular solution model for lithium-lithium fluoride and sodium-sodium chloride binary solutions. Nakanishi [23] employed the Margules model to compute the eutectic point of various ternary molten salt mixtures.

1.3.2 Liquid Metal Combustion Studies. Several studies are reported which are concerned with the combustion of liquid metals with halogen or halogenated gases. Mattavi [24] investigated analytically and experimentally the reaction characteristics of a chlorine bubble moving through liquid sodium. Little [25] examined the reaction characteristics of a static molten lithium metal surface during the first few seconds after exposure to nitrogen, oxygen, dichlorodifluoromethane, octofluorocyclobutane, and sulfur hexafluoride. Avery [22, 26] developed a correlation for the combustion length of an oxidizer jet discharging from a choked submerged injector by using data on a chlorine jet discharging into a bath of sodium and sodium chloride. The results of this study are of interest in combustion chamber design, since the oxidizer jet must remain within the confines of the bath if corrosive damage to the combustion chamber is to be avoided.

1.4 Specific Statement of the Problem

Previous studies of liquid metal combustion have been concerned with general hardware development and specific details of the combustion process. No attempt has been made to develop an adequate thermodynamic model for the liquid and gas phases present in the combustion chamber. Essential design information, such as combustor bath composition and density, the cover gas composition, and system performance are also unknown at this time.

The present investigation considers the development of a thermodynamic model for the ternary immiscible liquid mixture present in the reaction chamber of a combustor using the lithium-sulfur hexafluoride reactant combination. The data required to test the model have been generated using a steady vented combustor, which provides steady state conditions for the measurements. Steady state conditions allow accurate performance measurements to be made, and meaningful bath samples to be taken. The present investigation also demonstrates long term operation of a steady metal combustion system, which had not been achieved previously.

The thermodynamic model developed in the course of this study will be useful for the analyses of other combustion processes and combustor concepts involving the lithium-sulfur hexafluoride reactant combination. An example of such an application is the pot-type combustor described earlier. Additionally, the model will permit the thermodynamic characteristics of the present system to be predicted at operating conditions not examined experimentally.

The specific objectives of the present study can be summarized as follows:

1. Measure bath densities, bath compositions, and thermal performance for temperatures typical of metal combustor operation.
2. Develop a thermodynamic model for the bath liquids and compare the model predictions with the measurements.
3. Examine continuous operation of a complete steady combustor system with varying thermal load requirements for extended periods of time.

The study was limited to the lithium-sulfur hexafluoride reactant combination.

CHAPTER II

THEORETICAL CONSIDERATIONS

2.1 Existing Theory

Several techniques exist for the calculation of thermodynamic properties of multicomponent solutions. In general, all techniques provide an equation to represent the excess Gibbs free energy of mixing, f^E . An excess thermodynamic quantity of mixing is defined as the deviation of that quantity from the value given by Raoult's law which governs an ideal mixing process. The excess Gibbs free energy of mixing can therefore be defined as:

$$f^E = \frac{\Delta F_{\text{mix}}}{n_T} - \frac{RT}{n_T} \sum_i n_i \ln x_i \quad (2.1)$$

The two important thermodynamic properties of the mixture, enthalpy and component activities, can be obtained from the excess Gibbs free energy of mixing expression. The activity coefficients of each component are given by the following exact thermodynamic relation:

$$RT \ln \gamma_i = \left(\frac{\partial [n_T f^E]}{\partial n_i} \right)_{T, P, \text{all } n_j (j \neq i)} \quad (2.2)$$

Similarly, an expression can be derived for the mixture enthalpy as a function of the excess Gibbs free energy of mixing.

The excess Gibbs free energy of mixing can be related to the excess entropy and enthalpy of mixing as follows:

$$f^E = h^E - Ts^E \quad (2.3)$$

The simplest model is the ideal solution treatment which involves setting f^E equal to zero. It is noted that for an ideal solution Equation (2.2) gives an activity coefficient of unity for all components. This approach was not considered in the present study since the immiscibility of the system under study indicates that it is strongly nonideal. Methods appropriate to nonideal solutions include regular solution models (where s^E is equated to zero), and athermal models (where h^E is equated to zero). The equations which form the thermodynamic models contain empirical coefficients, the number of which is dependent on the particular model under consideration and the number of components in the multicomponent system. The advantage of the models is that the empirical coefficients are determined from solubility data on the constituent binary systems, and in this manner permit the binary system data to be extended to predict the properties of more complex systems. The thermodynamic models available in the literature for this purpose are reviewed in the following paragraphs.

Wohl [27] provided a review of three two-parameter equations referred to as the van Laar, the Margules, and the Scatchard-Hamer types. The van Laar equation has been the most widely used, and is commonly known as the regular solution treatment.

Wilson [28] developed a new type of two-parameter equation based on the athermal model for the excess free energy and semitheoretical considerations. Applications of this equation to multicomponent mixtures were presented by Orye and Prausnitz [29]. A great disadvantage of the two-parameter Wilson equation is that it cannot predict the phase separation of immiscible mixtures, but this

inadequacy can be removed by the inclusion of a third empirical parameter forming a three-parameter equation. The three-parameter Wilson equation was derived by Hiranuma [30] in a manner which gave some physical significance to the third parameter. Nagata and Yamada [31] modified the two-parameter Wilson equation by expressing each empirical parameter as a quadratic function of temperature and yielding a six-parameter equation. Since the system under study is known to be immiscible, the two-parameter Wilson equation was not considered for use.

Renon and Prausnitz [32] developed a three-parameter equation based on the two-liquid theory of binary mixtures which includes the effects of the nonrandomness of mixing. The equation is referred to as the NRTL (nonrandom, two-liquid) equation. Marina and Tassios [33, 34] reduced the NRTL equation to a two-parameter equation by fixing the value of negative unity for one of the basic NRTL parameters. The resulting equation is referred to as the LEMF (local effective mole fraction) equation.

Bruin [35] presented three additional two-parameter equations which were developed by considering various approximations to the excess Gibbs free energy expression, Equation (2.3), and employing basic van Laar and Wilson solubility parameters. These equations are known as the EVL (extended van Laar), the enthalpic Wilson, and the Orye equations.

The above review indicates that numerous thermodynamic models exist for the excess Gibbs free energy of a mixture. The models were developed for mixtures composed of pure components showing properties associated with normal liquids (see Appendix 1 of

Reference [38]). The question of whether the models can be applied to the system under study was partially answered by Pitzer [36] who examined various alkali halide-metal systems, and concluded that such systems display thermodynamic properties similar to those expected for mixtures of normal non-polar molecular liquids. The possible models for the structure of the alkali halide-metal mixtures were examined by Lumsden [37], who concluded that the most plausible model in the light of Pitzer's results is the existence of metal atoms and salt molecules. It was concluded from these findings that the models discussed above could be applied to the present system of alkali metal and molten salts.

The data available on the individual binary systems composing the ternary system under study are limited and do not justify the use of the more complex models employing more than two parameters per binary. Therefore, only the two-parameter models were considered for use in the present study. Most applications of the models have been limited to systems composed of water and organic compounds including hydrocarbons, since the models were developed primarily for use in the analyses of industrial separation operations. The two applications found in the literature which are related to the present study used forms of the van Laar equation. Nakanishi [23] computed the eutectic point of ternary molten salt mixtures using the Margules equation, which is effectively a one-parameter van Laar equation resulting from setting one of the empirical parameters equal to unity. The results indicates that the Margules equation computed the eutectic compositions of the mixtures to within 1-4 mole %.

Avery [22] successfully employed the two-parameter van Laar equation in correlating the solubility characteristics of binary sodium-sodium chloride and lithium-lithium fluoride mixtures. The van Laar equation was selected for use in the present study because it has been used to model similar systems, and its simple mathematical form minimizes the difficulty of evaluating the empirical parameters. The development of the various expressions resulting from the van Laar equation is discussed below.

2.2 The Thermodynamic Model

2.2.1 Assumptions. The major assumptions of the present analysis are summarized as follows:

1. The van Laar expression for the excess Gibbs free energy of mixing is used in the liquid phases.
2. The gas phase is assumed to be an ideal mixture.
3. The argon cover gas is assumed to be insoluble in the liquids.
4. The change in activity of the liquid phase components with pressure is neglected.
5. The reaction chamber pressure is taken to equal one atmosphere (1.013 bar).
6. The liquid phase densities are computed assuming no volume change on mixing.
7. In the analysis of binary phase diagram data, it is assumed that no solid solutions are formed.

2.2.2 Gibbs Free Energy of Mixing. The total free energy, F , of a homogeneous solution is written as

$$F = \sum_i n_i f_i^0 + RT \sum_i n_i \ln x_i + \sum_i n_i [f^E] \quad (2.4)$$

where f^E is the excess free energy of mixing. If a standard state is chosen as the pure liquid component i , then the activity is set equal to unity in this state, and we have for any other state

$$RT \ln a_i = \bar{f}_i - f_i^0 \quad (2.5)$$

By differentiating Equation (2.4) with respect to n_i to yield \bar{f}_i , and rearranging, it can be shown that

$$RT \ln a_i = RT \ln x_i + \left. \frac{\partial [n_T f^E]}{\partial n_i} \right|_{T, P, \text{all } n_j (j \neq i)} \quad (2.6)$$

where

$$n_T = \sum_i n_i \quad (2.7)$$

The activity coefficient is defined as follows:

$$\gamma_i = \frac{a_i}{\Gamma_i x_i} \quad (2.8)$$

The effect of pressure on the activity of all components in the reference state, Γ_i , was neglected since the change of activity with pressure is small for liquids and the system pressure is always close to atmospheric. By substitution of Equation (2.8) into Equation (2.6), an exact equation for the activity coefficient results:

$$RT \ln \gamma_i = \left(\frac{\partial [n_T f^E]}{\partial n_i} \right)_{T, P, \text{all } n_j (j \neq i)} \quad (2.9)$$

As discussed in the previous section, the van Laar expression for the excess free energy of mixing is employed. This expression is given by Wohl [27] and Lewis and Randall [34], and is written for a binary system composed of components i and j as follows:

$$f^E = \frac{n_i n_j b_i b_j A_{ij}'}{n_T (n_i b_i + n_j b_j)} \quad (2.10)$$

Since only two-body molecular interactions were considered in the development of the binary expression, the expression can be extended to the multicomponent case by a summation procedure without affecting the level of approximation as follows:

$$f^E = \frac{\frac{1}{2} \sum_i \sum_j n_i n_j b_i b_j A_{ij}'}{n_T \sum_i n_i b_i} \quad (2.11)$$

It is noted that in Equation (2.11) and in all equations to follow,

$$A_{ij}' = A_{ji}' \text{ and } A_{ii}' = A_{jj}' = 0.$$

The parameters b_i are interpreted as molecular-volume or quasilattice parameters, and can be approximated by molar volumes for some solutions. The parameters A_{ij}' are interpreted as interaction energies and are a measure of the deviation from ideal-solution behavior. Typically both types of parameters are positive, but the interaction energies can be negative for some solutions.

Equations (2.11) result in three and six-parameter representations of binary and ternary systems, respectively. The binary expressions are reduced to two-parameter equations and the ternary expression to a five-parameter equation by the following redefinition of parameters:

$$A_{ij} = b_i A_{ij}' \quad (2.12)$$

$$B_1 = \frac{b_1}{b_2} \quad B_2 = \frac{b_2}{b_3} \quad B_3 = \frac{b_1}{b_3} \quad (2.13)$$

The quantities defined by Equations (2.12) and (2.13) may be functions of temperature. For most systems the B_i parameter is nearly temperature invariant, especially if it closely equals the ratio of the molal volumes; and the A_{ij} parameter usually has a small temperature dependence. It is noted that the dissymmetry of two of the three binary pairs composing the ternary system defines the dissymmetry of the third pair. In equation form the dissymmetry relationship is stated as

$$B_1 = \frac{B_3}{B_2} \quad (2.14)$$

Substitution of the parameters defined by Equations (2.12) and (2.13) into Equations (2.10) and (2.11) results in the following expressions for the excess free energy of the three binary systems and the ternary system:

Binary 1-2:

$$f^E = \frac{n_1 n_2 A_{12}}{n_T (B_1 n_1 + n_2)} \quad n_T = n_1 + n_2 \quad (2.15)$$

Binary 2-3:

$$f^E = \frac{n_2 n_3 A_{23}}{n_T (B_2 n_2 + n_3)} \quad n_T = n_2 + n_3 \quad (2.16)$$

Binary 1-3:

$$f^E = \frac{n_1 n_3 A_{13}}{n_T (B_3 n_1 + n_3)} \quad n_T = n_1 + n_3 \quad (2.17)$$

Ternary:

$$f^E = \frac{n_1 n_2 B_2 A_{12} + n_2 n_3 A_{23} + n_1 n_3 A_{13}}{n_T (B_3 n_1 + B_2 n_2 + n_3)} \quad n_T = n_1 + n_2 + n_3 \quad (2.18)$$

The set of van Laar equations described above are referred to as the unsymmetric van Laar treatment since the equations include effects of the different molecular sizes of the pure components. The symmetric treatment, Margules equation, results if all the B_i parameters are set equal to unity.

2.2.3 Activity Coefficients. The van Laar equations for the activity coefficients result by substitution of Equations (2.10) and (2.11) into Equation (2.9). The general expression is written as follows prior to the substitution of the parameters defined by Equations (2.12) and (2.13):

$$\ln \gamma_k = \frac{b_k \sum_i \sum_j (A_{ik}' - \frac{1}{2} A_{ij}') b_i b_j n_i n_j}{\sum_i (n_i b_i)^2} \quad (2.19)$$

The two-parameter representation of a binary system composed of components 1 and 2 is written as follows:

$$\ln \gamma_1 = \frac{A_{12}}{RT} \left(\frac{x_2}{B_1 x_1 + x_2} \right)^2$$

$$\ln \gamma_2 = \frac{A_{12}}{B_1 RT} \left(\frac{B_1 x_1}{B_1 x_1 + x_2} \right)^2 \quad (2.20)$$

Similar expressions result for the remaining two binary systems and the ternary system.

2.2.4 Mixture Enthalpy. The total enthalpy of a multicomponent mixture is defined as

$$H = H_{\text{ideal}} + \Delta H_{\text{mix}} \quad (2.21)$$

where

$$H_{\text{ideal}} = \sum_i n_i h_i^{\circ} \quad (2.22)$$

$$\Delta H_{\text{mix}} = \Delta F_{\text{mix}} + T \Delta S_{\text{mix}} \quad (2.23)$$

and

$$\Delta S_{\text{mix}} = - \left. \frac{\partial \Delta F_{\text{mix}}}{\partial T} \right|_{P, n_i} \quad (2.24)$$

$$\Delta F_{\text{mix}} = F - F_{\text{ideal}} \quad (2.25)$$

Substitution of Equation (2.4) into Equation (2.25) results in

$$\Delta F_{\text{mix}} = \sum_i (RT n_i \ln x_i + n_i f^E) \quad (2.26)$$

Substitution of Equation (2.26) into Equation (2.24) results

in

$$\Delta S_{\text{mix}} = - \sum_i \left(R n_i \ln x_i - n_i \left. \frac{\partial f^E}{\partial T} \right|_{P, n_j} \right) \quad (2.27)$$

Substitution of Equations (2.26) and (2.27) into Equation (2.23) yields

$$\Delta H_{\text{mix}} = n_T \left(f^E - T \left. \frac{\partial f^E}{\partial T} \right|_{P, n_i} \right) \quad (2.28)$$

This quantity is an excess quantity by definition since the heat of mixing of an ideal solution is zero.

The following expression results for the molar enthalpy of the solution by dividing Equation (2.21) by n_T after substitution of Equation (2.28):

$$h = \sum_i x_i h_i^o + \left(f^E - T \left. \frac{\partial f^E}{\partial T} \right|_{P, n_i} \right) \quad (2.29)$$

The van Laar expression for the excess free energy of mixing, Equation (2.11), is substituted into Equation (2.29) to yield

$$h = \sum_i x_i h_i^o + \frac{\frac{1}{2} \sum_i \sum_j n_i n_j b_i b_j A_{ij}}{n_T \sum_i n_i b_i} \left[1 + T \frac{\sum_i n_i \frac{\partial b_i}{\partial T}}{\sum_i n_i b_i} \right] - T \frac{\sum_i \sum_j n_i n_j \left(b_i b_j \frac{\partial A_{ij}}{\partial T} + b_i A_{ij} \frac{\partial b_j}{\partial T} + b_j A_{ij} \frac{\partial b_i}{\partial T} \right)}{n_T \sum_i n_i b_i} \quad (2.30)$$

All partial derivatives in Equation (2.30) are taken at constant pressure and composition.

2.2.5 Mixture Density. The density of the mixture was calculated by neglecting the volume change of mixing. Hildebrand, Prausnitz and Scott [39] presented an expression for the change in molal volume of a component upon mixing that requires knowledge of the internal pressure, $\left. \frac{\partial E}{\partial V} \right|_T$, of the pure component. This correction was not used since the internal pressures of the substances under study are not known; and the calculation results in only a small correction to the pure component value in most systems. The density of the mixture is therefore written as

$$\rho = \frac{\sum_i M_i X_i}{\sum_i \frac{M_i X_i}{\rho_i}} \quad (2.31)$$

where M_i and ρ_i are the molecular weight and density of pure component i , respectively.

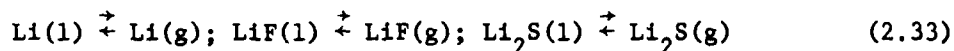
The pure component properties used in Equations (2.30) and (2.31) are either taken from the literature or estimated when the necessary information was absent. Appendix B presents the sources of the property data and discusses the methods used to estimate property data not available in the literature.

2.2.6 Gas Phase. The gas phase is assumed to be an ideal gas mixture, and therefore the fugacity of each species is equal to its partial pressure, p_i . The standard state of a pure liquid component is defined as discussed in Section 2.2.2. In a state of equilibrium the fugacity of a component is the same in all phases. Therefore

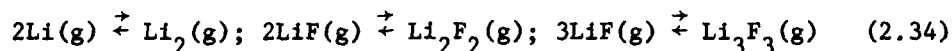
$$a_i = \frac{p_i}{p_i^o} \quad (2.32)$$

where p_i^o is the vapor pressure of pure component i . Equation (2.19) is employed to calculate the activity of component i in the solution. Equations (2.32) result in one equation for each of the three components, lithium, lithium fluoride and lithium sulfide, in the ternary system under study.

The vapor pressures of the pure components in the above equations are found from the equilibrium equations for vaporization of the pure liquids. Again a set of three equations results:



Data from the JANAF Thermochemical Tables [10] and the experimental data of Berkowitz and Chupka [40] indicate the formation of polymeric species in the gas phase. The following equations are written to include the polymeric species:



The processes described by Equations (2.33) and (2.34) can be written in general form as

$$\nu_i' N_i = \nu_j'' N_j \quad (2.35)$$

The general form of the equilibrium constant for a process described by Equation (2.35) is as follows:

$$K_j = \frac{a_j^{\nu_j'}}{a_i^{\nu_i''}} \quad (2.36)$$

The equilibrium constants of Equations (2.36) can be also expressed as

$$\Delta f_i - \Delta f_i^0 = RT \ln K_i \quad (2.37)$$

At equilibrium $\Delta f_i = 0$ and therefore:

$$\Delta f_i^0 = -RT \ln K_i \quad (2.38)$$

For the process represented by Equations (2.35), the following expressions result:

$$K_j = \exp [(\nu_i' f_i^0 - \nu_j'' f_j^0)/RT] \quad (2.39)$$

The pure component properties used in Equations (2.30) are either taken from the literature or estimated as discussed in Appendix B.

The change in the activities of the pure liquid components with pressure was neglected, and the activities were taken to equal unity. The standard state for the gaseous species was taken as the state where the fugacity equalled one atmosphere (1.013 bar) to permit the use of tabulated thermodynamic data employing the same standard state [10]. Therefore, under the ideal gas assumption it follows that

$$a_i(g) = p_i \text{ (atm)} \quad (2.40)$$

The partial pressures in Equation (2.40) are denoted by p_i^0 when the equation is applied to Equations (2.33) representing the vaporization of the pure liquids.

Substitution of Equations (2.40) and (2.32) into Equations (2.36) results in the following expressions for the vapor pressures of the various species in units of atmospheres:

$$\begin{aligned} p_{Li} &= K_{Li} a_{Li} & p_{Li_2} &= K_{Li}^2 a_{Li}^2 \\ p_{LiF} &= K_{LiF} a_{LiF} & p_{Li_2F_2} &= K_{Li_2F_2} K_{LiF}^2 a_{LiF}^2 \\ p_{Li_2S} &= K_{Li_2S} a_{Li_2S} & p_{Li_3F_3} &= K_{Li_3F_3} K_{LiF}^3 a_{LiF}^3 \end{aligned} \quad (2.41)$$

Where the activities are computed from Equations (2.19) and the equilibrium constants are computed from Equations (2.39).

In addition to the gaseous species treated above, argon exists in the system as a cover gas. Thormeier [41] investigated the solubility of helium and argon in liquid sodium, and provided a correlation based on a solubility parameter which permitted

prediction of the solubility of noble gases in other liquid metals. After the correlation was substantiated by testing it against the data of Slotnick, et al., [42] for the solubility of helium in lithium; it was used to predict that the solubility of argon in lithium was in the range of 10^{-10} to 10^{-11} on a mole fraction basis at 1200°K. The mole fraction of argon in a mixture of lithium, sodium and potassium fluorides (46.5-11.5-42.0 mole percent) was extrapolated from data presented by Blander [43] to be in the range of 10^{-6} to 10^{-7} at 1200°K. Based on these results, the solubility of the argon cover gas in the liquid mixture was neglected. For the case where the combustor is vented to atmospheric pressure, the total pressure of the gas phase equals one atmosphere, and the partial pressure of the argon is given by the following:

$$P_A = 1 - P_{Li} - P_{Li_2} - P_{LiF} - P_{Li_2F_2} - P_{Li_3F_3} - P_{Li_2S} \quad (2.42)$$

2.2.7 Summary of the Thermodynamic Model. The van Laar thermodynamic model developed in the previous sections permits the calculation of the excess Gibbs free energy of mixing of the ternary system from data on the solubility characteristics of the constituent binary systems. The formulation permits the calculation of other thermodynamic properties such as liquid phase activities, densities, and enthalpies, and gas phase partial pressures. The model parameters can be calculated from binary solid-liquid equilibria data, vapor-liquid equilibria data, or data on two equilibrated liquid phases. The procedures utilized to determine the parameters in the present investigation are described in Appendix C, and the binary results are presented in Chapter III. The activity expressions

are utilized in the following section to predict the liquid phase solubilities of a steady metal combustor system.

2.3 Prediction of Liquid Phase Solubilities of a Steady Metal Combustor

The design of a steady metal combustor system is based on the continual removal of the product-rich phase or the phase rich in lithium fluoride and lithium sulfide, and the continual addition of lithium to replenish the fuel-rich phase. Separation of the combustor bath liquid into the two immiscible phases occurs if the fugacity of each component is identical in each phase. Since the standard state for each component is the same in each phase, the condition for phase separation implies that the activity of each component is identical in each of the two phases. The two phases are indicated by mole fractions x_i and y_i , and the requirement for phase separation is stated in equation form as

$$a_i(x_i) = a_i(y_i) \quad (2.43)$$

Since the mole fractions in each phase must sum to unity, two additional equations result:

$$\sum_i x_i = 1 \quad (2.44)$$

$$\sum_i y_i = 1 \quad (2.45)$$

Under steady state conditions, the fuel and oxidizer flow rates are in stoichiometric proportion, and the products of the reaction are removed in a mole fraction ratio controlled by the

stoichiometry of the reaction. The stoichiometry of a chemical reaction can be expressed as

$$\sum_{i=1}^n \nu_i' N_i \rightarrow \sum_{i=1}^n \nu_i'' N_i \quad (2.46)$$

where N_i represents the chemical symbol of species i , and ν_i represents the number of moles. For such a reaction the mole fraction ratio of any two product species can be expressed as follows:

$$\frac{x_i}{x_j} = \frac{\nu_i''}{\nu_j''} \quad (2.47)$$

For the reaction under study the stoichiometric equation is



Therefore, the mole fractions of lithium fluoride and lithium sulfide in the product-rich phase are related as follows:

$$\frac{x_{\text{LiF}}}{x_{\text{Li}_2\text{S}}} = 6 \quad (2.49)$$

Equations (2.43), (2.44), (2.45), and (2.49) provide a set of six equations to solve simultaneously for the six unknown mole fractions. The procedure used to solve the set of nonlinear equations is described in Appendix A. Following the solution for the unknown mole fractions, the equations previously developed were employed to compute other mixture properties such as density and enthalpy, and the gas phase composition.

CHAPTER III

DETERMINATION OF THE THERMODYNAMIC MODEL PARAMETERS

3.1 Introduction

The thermodynamic model for the ternary system presented in Chapter II contains five empirical parameters which were determined from data on the constituent binary systems. The three systems are lithium-lithium fluoride, lithium fluoride-lithium sulfide, and lithium-lithium sulfide. The methods used to obtain and analyze the data on each binary pair are described in the following sections.

3.2 Lithium-Lithium Fluoride Binary

The solubility data for the immiscible liquid region of the lithium-lithium fluoride system presented by Dworkin, et al., [20] were utilized to determine the two empirical parameters associated with this binary pair. The components of the ternary system were labeled such that subscripts 1, 2, and 3 represented components lithium, lithium fluoride and lithium sulfide, respectively. Employing this convention, the empirical parameters representing the lithium-lithium fluoride binary are indicated by A_{12} and B_1 .

The procedure used to determine the parameters is outlined in Section C.2 of Appendix C. Specifically, the data taken from Reference [20] was substituted into Equations (C.17) and (C.18) to yield values of the parameters over a range of temperatures. The results are shown in Figure 3, along with a linear least squares fit for each parameter. The equations for the parameters are

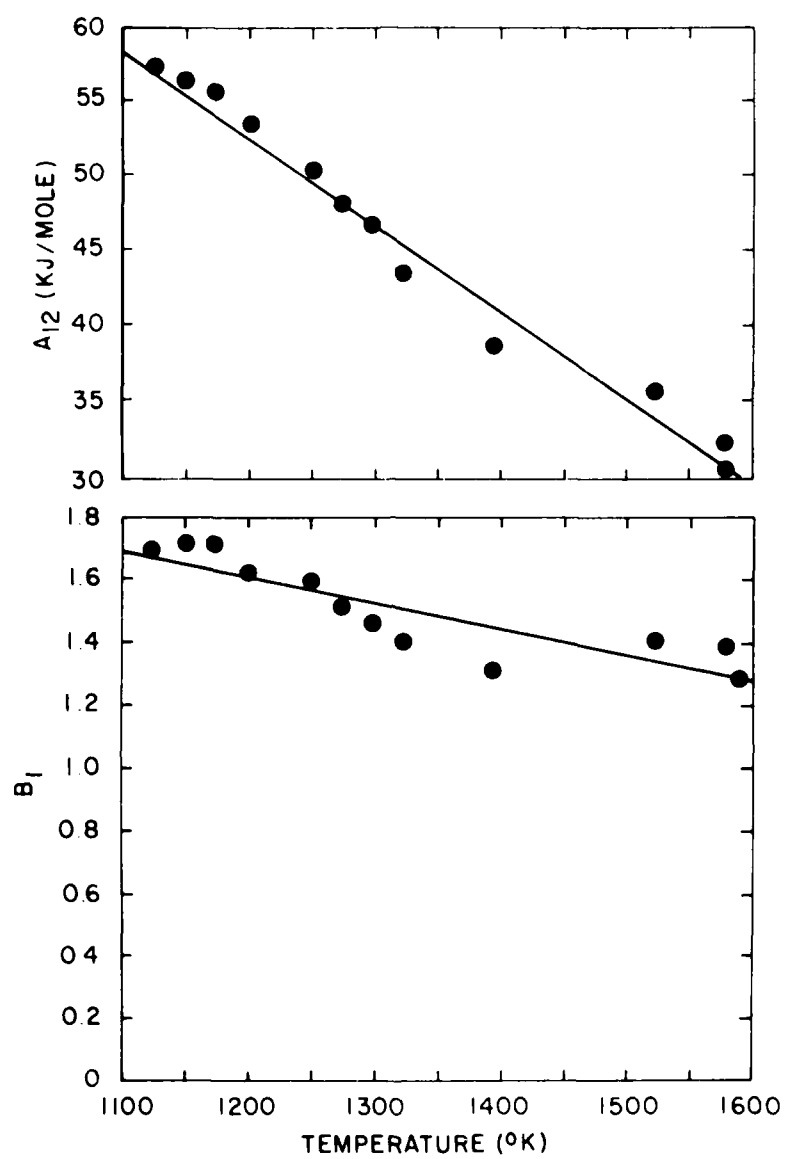


Figure 3 Lithium-Lithium Fluoride Binary Parameters

$$A_{12} = 121.53 - 0.05730T \text{ (kJ/mole)} \quad (3.1)$$

$$B_1 = 2.5846 - 8.132 \times 10^{-4}T \quad (3.2)$$

The estimated standard deviations of the A_{12} and B_1 parameters about the regression lines are 1.36 kJ and 0.08, respectively. It is noted that the interaction energy parameter, A_{12} , has a stronger temperature dependence than the quasilattice parameter, B_1 . Since the B_1 parameter is associated with the sizes of the molecules, it is not expected to vary greatly with temperature.

The parameters given by Equations (3.1) and (3.2) were employed with the binary van Laar model to compute the solubility characteristics of the immiscible liquid region utilizing a procedure similar to that described in Section 2.3. In Figure 4 the results are compared to the data taken from Reference [20]; the agreement is good over the complete temperature range including the consolute point.

3.3 Lithium-Lithium Sulfide Binary

No data were available in the literature concerning the lithium-lithium sulfide binary system. Therefore tests were conducted in this study to determine the solubility characteristics of the region of the phase diagram consisting of solid lithium sulfide and a lithium-rich liquid.

The tests consisted of stabilizing a bath containing the two components at the desired temperature, sampling the bath, and subjecting the samples to the wet-test chemical analysis procedures described in Appendix D. The bath was contained in a type 316

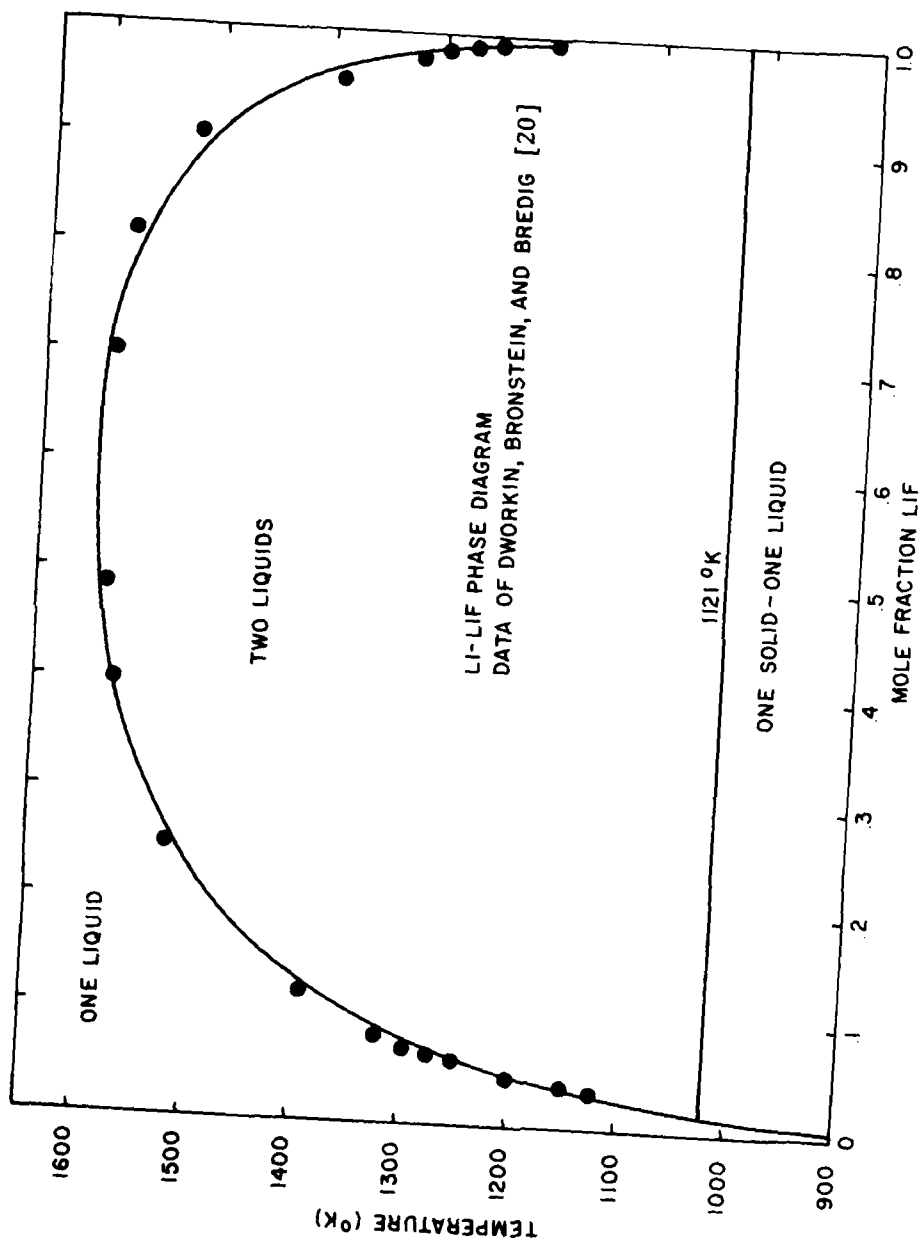


Figure 4 Lithium-Lithium Fluoride Solubility Results

stainless steel vessel, 6.27 cm in diameter and 26.0 cm in length. The vessel was installed in a Lindberg Hevi-Duty crucible furnace, type 56622, controlled by a type 59344 temperature controller. Temperatures were measured with chromel-alumel thermocouples inserted into the bath, and recorded with either a Leeds and Northrup model 8686 millivolt potentiometer or a Leeds and Northrup Speedomax-H null-balance recorder.

The lithium and lithium sulfide reagents used in the tests were produced by the Lithium Corporation of America and Research Organic/Inorganic Chemical Corporation, respectively. The purities were listed as 99.9% for the lithium with the major contaminants being sodium (0.007%) and silicon (0.006%), and 98% for the lithium sulfide with the contaminants not specified. Approximately 30.5 gm of lithium sulfide and 166 gm of lithium were added to the vessel for each of the three test sequences.

Bath saturation was insured by maintaining the components at a given temperature condition for approximately 23 hours. The bath was stirred with an argon bubbler for the first 19 hours of the period and maintained stagnant under an argon cover for the remaining time.

The solubility test results are plotted as mole fraction lithium sulfide versus temperature in Figure 5. The data were employed to compute the two empirical parameters, A_{13} and B_3 , associated with this binary pair.

The solid-liquid equilibria expression, Equation (C.10), developed in Appendix C was used to evaluate the empirical parameters.

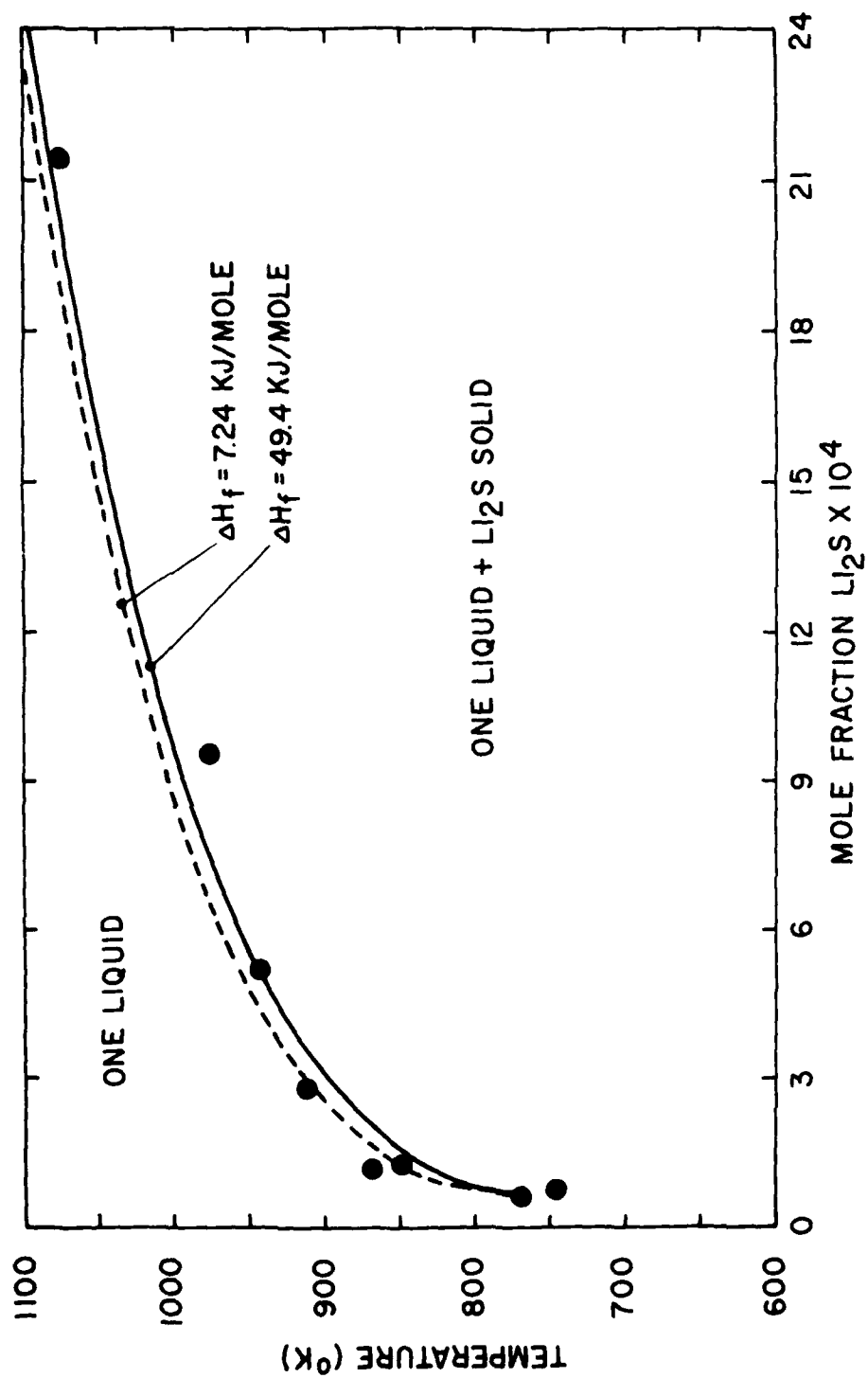


Figure 5 Lithium-Lithium Sulfide Solubility Results

The parameter B_3 was taken to be temperature invariant, and A_{13} was assumed to be a linear function of temperature as follows:

$$A_{13} = A + B T \quad (3.3)$$

In the range where the lithium sulfide (component 3) mole fraction is negligible compared to unity, Equation (C.10) yields a one-to-one relationship between the parameters A/B_3 and B/B_3 at each temperature-mole fraction condition. The equation was rearranged into the form

$$Y_1 = \frac{A}{B_3} + \frac{B}{B_3} X_1 \quad (3.4)$$

where X_1 and Y_1 are constants determined from the temperature-mole fraction data. Least squares regression techniques were applied to the set of X_1 and Y_1 determined from the data to obtain values for A/B_3 and B/B_3 .

Data on the melting temperature, heat of fusion, and heat capacity of lithium sulfide are required to evaluate the constants X_1 and Y_1 . The melting temperature is known [15], but the heat of fusion and heat capacity information was not available in the literature. Estimates of both these quantities were made using the procedures described in Appendix B. The difference between the partial molal heat capacity of lithium sulfide in solution and the molal heat capacity of solid lithium sulfide was taken to be 4.18 J/mole in the temperature range of interest. The value was estimated from the estimated heat capacities of the pure liquid and solid. The heat-capacity term in Equation (C.10) is dominated by the heat-of-fusion term, and therefore the heat capacity estimates are not critical to the calculation. The heat of fusion of lithium sulfide

was estimated to be 7.24 KJ/mole. During the analysis of the lithium fluoride-lithium sulfide binary, evidence indicated that a higher heat of fusion could be associated with the compound. The higher value of 49.4 KJ/mole was also carried through the analysis.

The data obtained on the lithium-lithium sulfide binary could not be used to firmly fix the value of the quasilattice parameter B_3 . Additional data in the lithium sulfide-rich portion of the phase diagram is required to determine B_3 . Information could be obtained on the B_3 parameter by making a comparison to the lithium-lithium fluoride binary. It was expected that the parameter would be somewhat smaller than the corresponding value of 1.61 (at 1200°K) determined for the lithium-lithium fluoride binary because the molar volume of lithium sulfide is larger than that of lithium fluoride. The effects of the parameter B_3 on the ternary solubility predictions were examined. It was found that the experimental data was predicted most accurately with a B_3 value which yielded an interaction energy approximately equal to that of the lithium-lithium fluoride binary. It is not unexpected that the two systems have similar interaction energies since it is strongly suspected, although not verified, that the lithium-lithium sulfide system has immiscibility characteristics similar to the lithium-lithium fluoride system. The parameter B_3 was determined by equating the interaction energy parameter A_{13} to the corresponding parameter in the lithium-lithium fluoride binary, A_{12} , at a temperature of 1200°K. The values determined in this manner were 1.24 for the low heat of fusion case, and 1.36 for the high heat of fusion case. Both values are lower than the corresponding value for the lithium-lithium fluoride binary.

The parameters for the low heat of fusion case are

$$A_{13} = 88.291 - 0.02975T \text{ (kJ/mole)} \quad (3.5)$$

$$B_3 = 1.24 \quad (3.6)$$

and for the high heat of fusion case are

$$A_{13} = 53.287 - 4.00 \times 10^{-4}T \text{ (kJ/mole)} \quad (3.7)$$

$$B_3 = 1.36 \quad (3.8)$$

The standard deviation of the variable Y_1 in Equation (3.4) gives an indication of the precision of the parameter A_{13} . For the low heat of fusion case, the estimated standard deviation of Y_1 is 1.39 kJ/mole for values ranging from 47.64 to 59.58 kJ/mole. For the high heat of fusion case, the estimated standard deviation of Y_1 is 1.44 kJ/mole for values ranging from 37.14 to 41.62 kJ/mole. Changes in the parameter B_3 affect the ternary predictions of lithium solubility in the products. A B_3 variation of ± 0.05 results in approximately a $\pm 5\%$ variation in the lithium solubility prediction. The solid-liquid equilibria results computed from Equation (C.10) are shown in Figure 5 for the two cases examined.

3.4 Lithium Fluoride-Lithium Sulfide Binary

The solubility characteristics of the lithium fluoride-lithium sulfide binary were experimentally examined by Faeth [21] using a thermal analysis procedure. The procedure involved measuring the thermal effects in the time-temperature curves of prepared samples of different compositions during cooling cycles. The thermal effects

consisted of constant temperature periods or hold-ups at sample temperatures where phase transitions occurred. During the phase transition, the temperature of the sample remained constant as the energy loss from the sample was balanced by the enthalpy change associated with the phase transition.

The samples were contained in a type 316 stainless steel capsule, 2.22 cm in diameter and 15.2 cm in length. The capsules were heated in a furnace to a temperature of 1303°K and allowed to stand for a period of five hours. The furnace was then turned off, and the time-temperature curve of the sample was recorded. Two thermal effects were observed; the effects represented the initial solidification of lithium fluoride from the mixture and the solidification of lithium fluoride and lithium sulfide at the eutectic temperature. Two tests were run for each condition, and the reproducibility was reported to be within 1°K.

The data obtained from the tests are plotted in Figure 6 as mole fraction lithium sulfide versus temperature. For lithium sulfide concentrations greater than the eutectic composition, only one of the two expected thermal effects was observed. The absence of the higher temperature thermal effect associated with the solidification of lithium sulfide was believed to be caused by experimental difficulties due to supercooling of lithium sulfide [21].

Equation (C.10) was used in conjunction with the data to determine the empirical constants associated with this binary system, A_{23} and B_2 . The required thermodynamic data needed in the analysis are available in the literature for lithium fluoride and the sources are presented in Appendix B. The results yielded a value of A_{23}

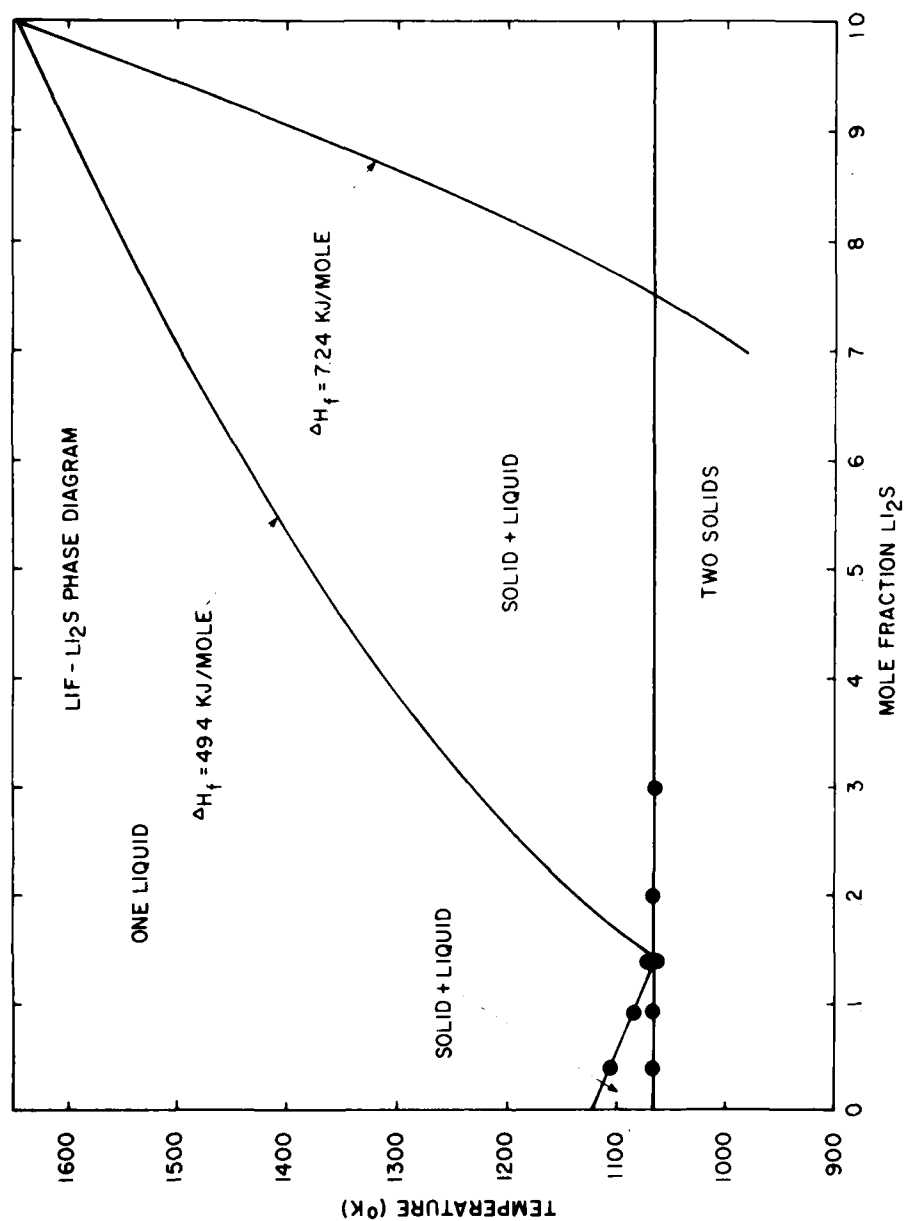


Figure 6 Lithium Fluoride-Lithium Sulfide Solubility Results

equal to zero, indicating that the solution exhibits ideal solution behavior in the temperature and composition range of the data. With B_3 and B_1 known, the value of B_2 was determined by the dissymmetry relationship, Equation (2.14).

The solubility data also yielded information concerning the heat of fusion of lithium sulfide. Equation (C.10) was used to compute the freezing point depression line extending from the melting point of pure lithium sulfide to the eutectic point. The results are shown in Figure 6. The difference between the partial molal heat capacity of lithium sulfide in solution and solid lithium sulfide was estimated to equal an average value of 1.09 J/mole in the temperature range of interest. The freezing point depression line computed using the heat of fusion estimated in Appendix B, 7.24 kJ/mole, does not yield the correct eutectic point; the value of the heat of fusion needed to correctly compute the eutectic point was found to equal 49.4 kJ/mole. Both heat of fusion values were considered in determining the thermodynamic model empirical parameters as described in Section 3.3 and below.

The value of the interaction energy parameter is given by

$$A_{23} = 0 \text{ (kJ/mole)} \quad (3.9)$$

It was estimated that the value of A_{23} is accurate to ± 1 kJ/mole. The quasilattice parameter is given for the low heat of fusion case by

$$B_2 = 1.0 / (1.90 - 5.98 \times 10^{-4} T) \quad (3.10)$$

and for the high heat of fusion case by

$$B_2 = 1.0 / (2.08 - 6.56 \times 10^{-4} T) \quad (3.11)$$

The accuracy of B_2 is fixed by the accuracy with which B_1 and B_3 were determined since it is fixed by the dissymmetry relationship.

3.5 Summary

The five empirical parameters required in the thermodynamic model developed in Chapter II were determined. The two parameters representing the lithium-lithium fluoride binary pair were determined most accurately since a greater amount of data is available on this system. The two parameters associated with the lithium-lithium fluoride binary are particularly important since the ternary system being considered in the present study consists largely of lithium and lithium fluoride in the composition and temperature range of interest. Solubility data for the lithium-lithium sulfide and lithium fluoride-lithium sulfide binaries were less abundant because of the experimental difficulties associated with the handling of lithium sulfide at high temperatures. Data generated for these systems in the present study and by Faeth [21] were used to evaluate the remaining three empirical parameters. Two sets of parameters were formed, one for each of the two values for the heat of fusion of lithium sulfide. Data on the lithium fluoride-lithium sulfide binary system indicated that the heat of fusion of lithium sulfide is higher than the estimated value. The predictions of the thermodynamic model as applied to a steadily operating liquid metal combustor will be compared to experimental data in Chapter V.

CHAPTER IV

EXPERIMENTAL APPARATUS AND PROCEDURE

4.1 Introduction

The experimental apparatus used in the study were designed to facilitate the extraction of bath liquid samples; the measurement of bath liquid densities; and the measurement of thermal performance under conditions where the combustion process is conducted in a steady manner. Two different combustors were employed in the course of the investigation. A radiative combustor was employed to generate the bath liquid density data and to obtain information required for the design of the larger air-cooled combustor. The air-cooled combustor was used to generate bath liquid solubility and thermal performance data.

Each combustor was designed in a breadboard style for experimental convenience in that the reaction chamber/heat exchanger, product collection tank, exhaust filter and fuel tank were separate components, and was not configured for direct application in a submersible. With the exception of the exhaust gas filter which was not used with the radiative combustor, both combustors consisted of the following major components: a) a reaction chamber; b) a product collection tank; c) a fuel tank; d) a fuel pump; e) an exhaust gas filter; and f) a control system. General descriptions of the components are given in the following sections.

4.2 Air-Cooled Combustor Apparatus

The air-cooled combustor apparatus is shown schematically in Figure 7, and as a photograph in Figure 8.

4.2.1 Reaction Chamber and Heat Exchanger. The reaction chamber and heat exchanger were fabricated from type 316 stainless steel. The reaction chamber had nominal dimensions of 0.28 cm, 48.3 cm and 26.0 cm for the wall thickness, length and diameter, respectively. The annular heat exchanger was positioned around the reaction chamber by six longitudinal spacers to provide an annular gap width of approximately 0.28 cm.

A sump was built into the bottom of the reaction chamber to contain the product-rich liquid. The system was designed to contain the product-rich liquid in a sump to minimize thermal management problems associated with maintaining the products in a molten state, and to take advantage of the superior heat transfer qualities of the liquid metal by having molten metal in contact with the entire heat-transfer surface.

The product-rich liquid was removed from the reaction chamber through a trap system which consisted of two coaxial tubes extending from the top and bottom of the chamber as shown in Figure 7. The shorter inner tube provided the path for liquid outflow to the product collection tank. The outer tube equalized the gas pressures in the trap and the chamber ullage space by allowing argon cover gas to flow from the ullage, through the cross-over port, and out the trap. The trap maintained product and fuel levels in the reaction chamber by a simple hydrostatic balance. If the top of the product

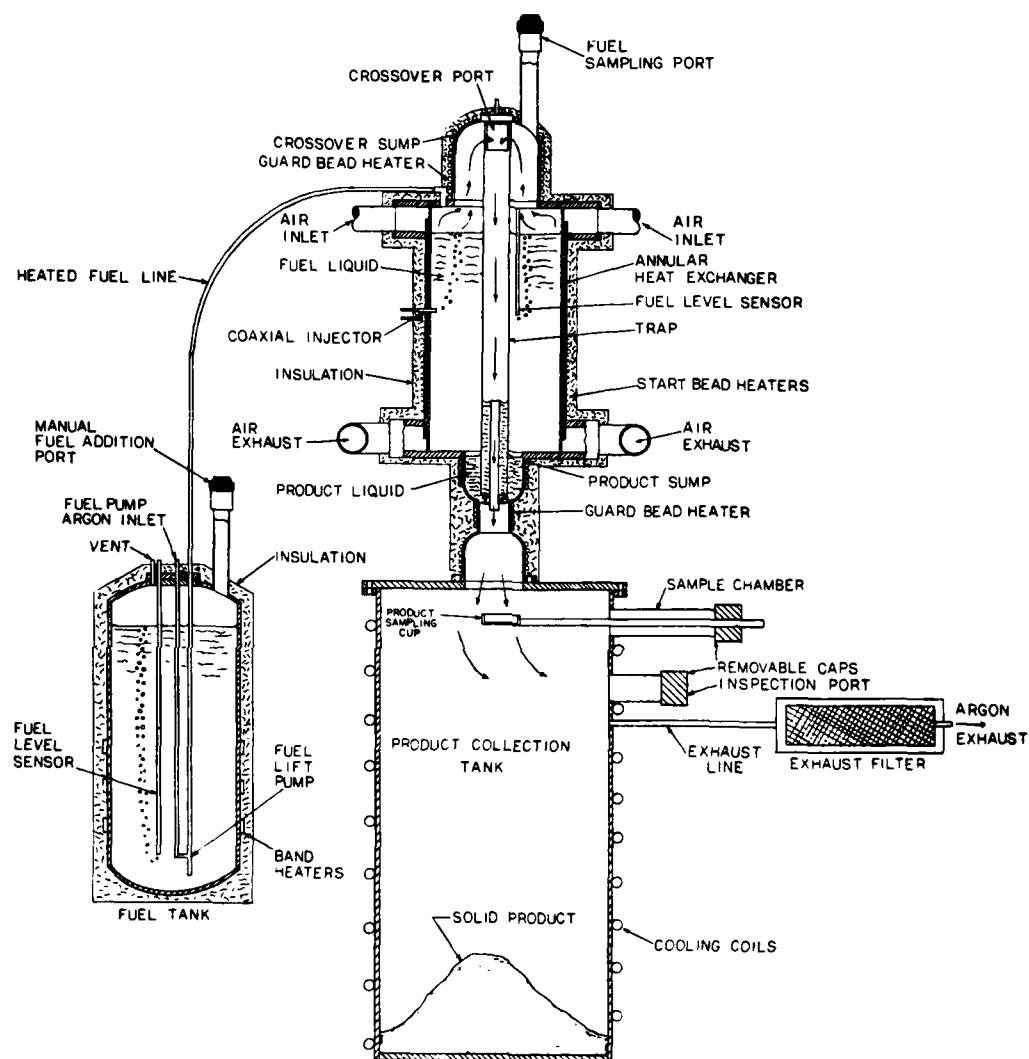


Figure 7 Schematic of Air-Cooled Steady Combustor Apparatus

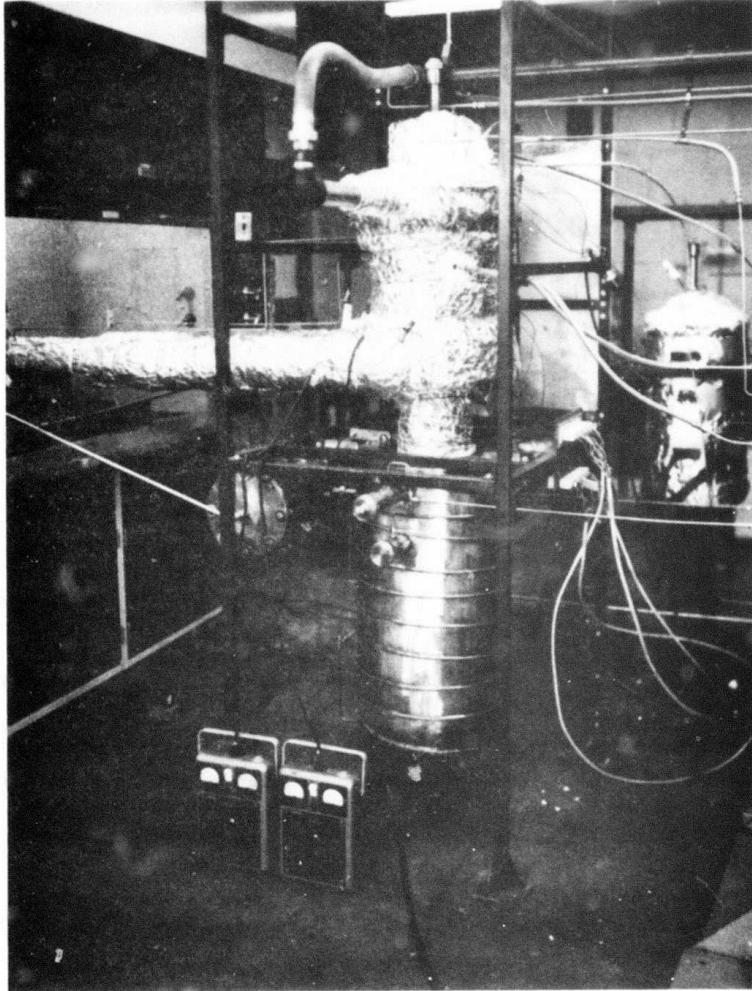


Figure 8 Photograph of Air-Cooled Steady Combustor Apparatus

layer is chosen as a datum point, then the hydrostatic pressures due to the product height in the trap above this point and the fuel height in the reaction chamber above this point are equal. The large density difference between the two liquids allows a small product height to balance a much larger fuel height. The outer tube had an inside diameter of 4.75 cm and a wall thickness of 0.165 cm, and the inner tube had an inside diameter of 1.57 cm and a wall thickness of 0.165 cm.

The crossover port was positioned in a sump built into the top of the reaction chamber. The purpose of the sump was to reduce the heat losses from the crossover port region, and to provide sufficient surface area to mount an electrical guard heater used to balance the parasitic heat loss from the region. If the temperature of the crossover-port region was permitted to drop below that of the bath, lithium and product vapor condensation would occur which could over a period of time result in the buildup of sufficient liquid to interrupt the argon flow through the trap. The sump temperature was controlled by a 1.5 kW bead heater mounted on the walls. The heater was manufactured by the Cole-Parmer Instrument Company (model 3116-40) and was controlled by a Honeywell temperature controller (model R7350A). The control signal to the controller was the output of a chromel-alumel thermocouple which was spot-welded to the wall of the sump.

A sampling port which provided access to the reaction chamber was mounted on the sump. The port was primarily used to take fuel-rich liquid samples by lowering a sample capsule on a specially designed

probe through the port, but it also functioned as a general inspection port and a manual fuel addition port (for solid fuel sticks).

Fuel entered the reaction chamber through a fitting welded into the top of the chamber. A low purge flow of argon was provided to the fitting to prevent diffusion of product vapors into the fuel line during periods when the fuel pump was inoperative.

Oxidizer was injected into the molten fuel through a coaxial injector shown schematically in Figure 9. In this type of injector the oxidizer flows in an inner core tube fabricated from nickel 200 alloy and is prevented from contacting the outer injector parts fabricated from type 316 stainless steel by a flow of inert argon gas in the outer shroud tube. The injector was installed in the reaction chamber by a threaded connection in a boss mounted in the wall a distance of 20.3 cm from the top.

The cooling air entered the heat exchanger inlet header through two inlet lines and was exhausted from the exit header through two exhaust lines, with both pairs of lines positioned 180° apart. The double inlet and exit configuration was used to ensure uniform air flow in the heat exchanger. The heat exchanger effectiveness was approximately 88% at a bath temperature of 1200°K.

The exterior surface of the heat exchanger was equipped with two electrical bead heaters used to melt the fuel prior to the start of the combustion process. The heaters provided an output of 1.5 kW each, and were manufactured by the Cole-Parmer Instrument Company (model 3116-40).

The reaction chamber/heat exchanger was connected to the collection tank by a product exhaust duct. The necked-down section

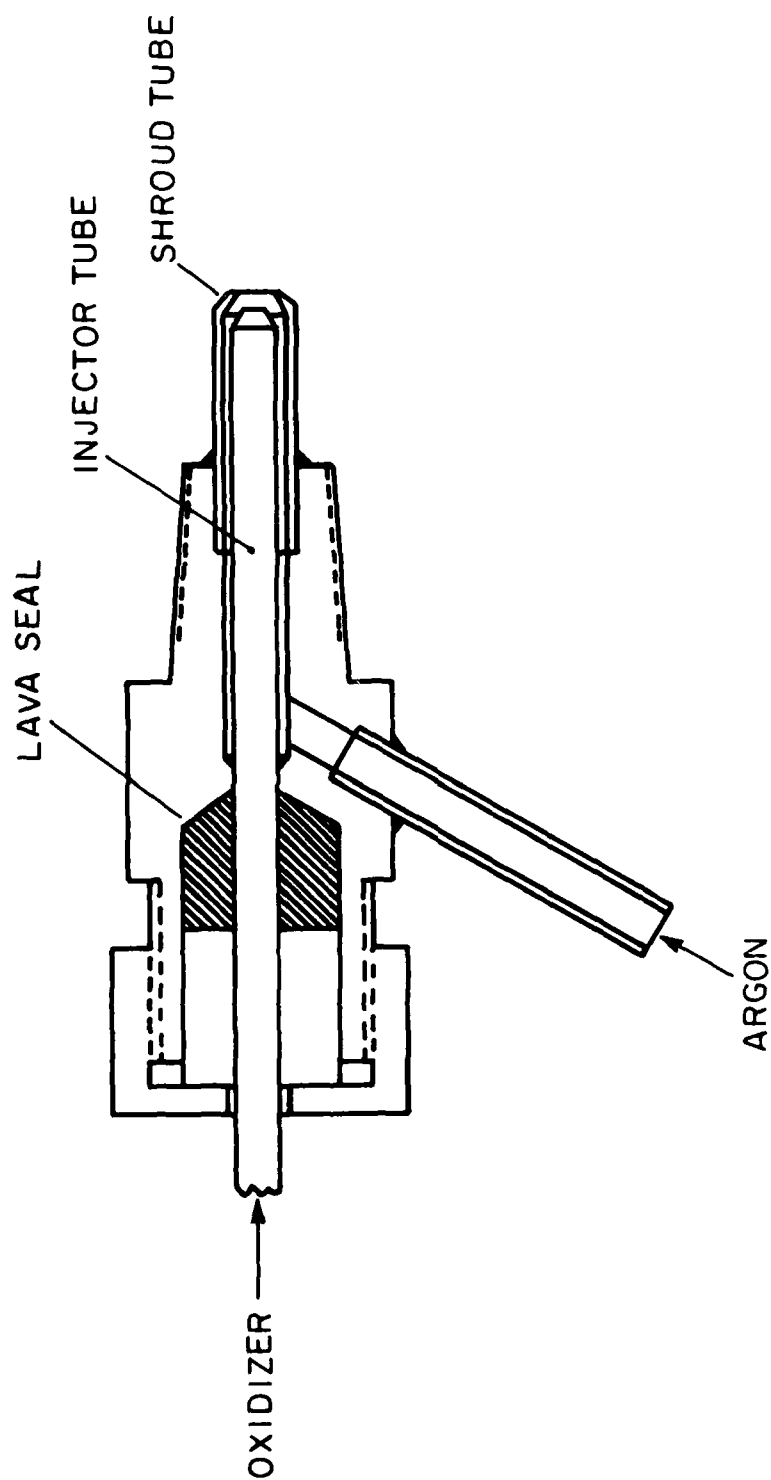


Figure 9 Sketch of the Coaxial Injector

of the duct was designed to reduce the view factor for thermal radiation from the tip of the trap tube to the cold collection tank. The larger diameter section was designed to reduce the possibility of product liquid contacting and freezing to the duct walls at the entrance to the product tank where the walls are unavoidably cooler. The product sump and product exhaust duct wall temperatures were controlled by electrical bead heaters operated through a temperature controller. The heaters were required to balance the significant heat loss through the sump/exhaust region both by conduction and radiation to the collection tank. The heaters were manufactured by the Cole-Parmer Instrument Company, with a 1.5 kW heater (model 3116-40) used on the sump and necked-down portion of the exhaust, and a 0.4 kW heater (model 3116-10) used on the larger diameter section of the exhaust. The sump heater was operated by a Honeywell model R7350A temperature controller. The control signal to the controller was the output of a chromel-alumel thermocouple which was spot-welded to the wall of the sump.

The exterior surfaces of the heat exchanger, sump, and product exhaust duct were insulated with approximately a 5 cm layer of Fiberfrax Lo-Con ceramic fiber blanket manufactured by the Carborundum Company.

4.2.2 Fuel Pump and Fuel Tank. All parts of the fuel pump and fuel tank were fabricated from type 316 stainless steel. The fuel pump was fabricated from standard tubing with an outside diameter of 0.635 cm and an inside diameter of 0.457 cm. The nominal dimensions of the fuel tank were 61 cm in length and 27 cm in diameter.

The fuel pump is shown schematically in Figure 7. Argon gas flowed into the pump through the vertical inlet line to the footpiece. The gas then flowed as a two-phase mixture with liquid lithium through the heated fuel line to the reaction chamber. The fuel flow rate was a function of the argon flow rate, lift height, and the fuel head on the footpiece inlet. Experimentally determined pump performance curves are shown in Figure 10. The fuel line temperature was maintained at approximately 540°K by a flexible, fibrous-glass insulated heater in order to prevent fuel solidification in the line. The heater was manufactured by the Cole-Parmer Instrument Company, (model 3105-80), and the power output was controlled by a variac up to a maximum of 0.38 kW.

A manual fuel addition port was provided at the top of the fuel tank to permit the addition of solid fuel which was melted in the tank and maintained at approximately 540°K. Power to the tank was provided by three band heaters which were controlled by variacs. The heaters were manufactured by the Chromalox Corporation, (model HB-1120), and provided a maximum output of 2.02 kW for each heater. The exterior surfaces of the fuel tank were insulated with approximately a 5 cm layer of Fiberfrax Lo-Con blanket.

4.2.3 Product Collection Tank. The product collection tank was fabricated from type 304 stainless steel. The nominal dimensions of the tank were 91 cm in length and 45 cm in diameter.

The product exhaust duct was connected to the collection tank lid with a bolted flange sealed by a metal O-ring (Advanced Products P/N 4750-5-7-SP). The lid was the only part of the apparatus bolted

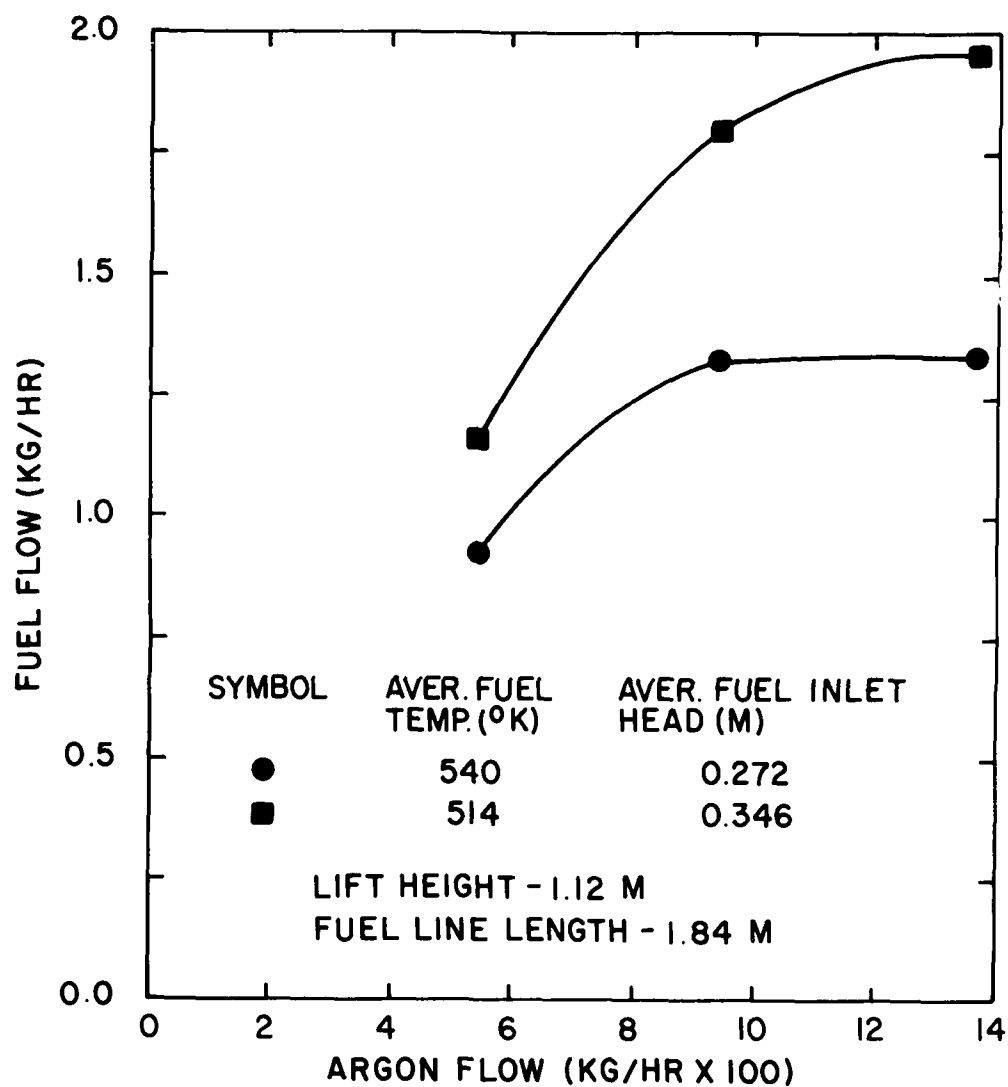


Figure 10 Performance Curves of the Argon Lift Pump

to the frame, and functioned as a single-point mount for the reaction chamber/heat exchanger and the collection tank. The collection tank was connected to the lid with a bolted flange sealed with a Viton O-ring.

The product collected tank was cooled by coils soldered to the tank wall, using water as the coolant.

Two ports were provided for access to the collection tank as shown in Figure 7. The top port was used to take product-rich liquid samples. The sample was retracted and allowed to cool in the sample chamber prior to final removal. The lower inspection port was used to observe the product level in the tank, and to provide access to the tank for physical manipulation of the product as the situation required.

4.2.4 Exhaust Filter. All argon flows entered the collection tank and then passed through an exhaust filter prior to being exhausted into a hood. The filter nominal dimensions were 16.5 cm in diameter and 45.5 cm in length. The filter element consisted of two sizes of type 316 stainless steel wire mesh cloth. The inner wraps were 40 x 40 mesh cloth followed by outer wraps of 200 x 200 mesh cloth. No attempt was made to optimize the filter design.

4.2.5 Control System. Figure 11 shows a schematic diagram of the flow control system for the apparatus. Details of some of the instrumentation shown in the figure are discussed in the next section. The various purge flows shown in Figure 11 were employed to prevent clogging of the gauge lines in the system by condensed lithium vapor. The purge flows also functioned to alleviate air contamination of the system when sample-port caps were removed. All flows in the

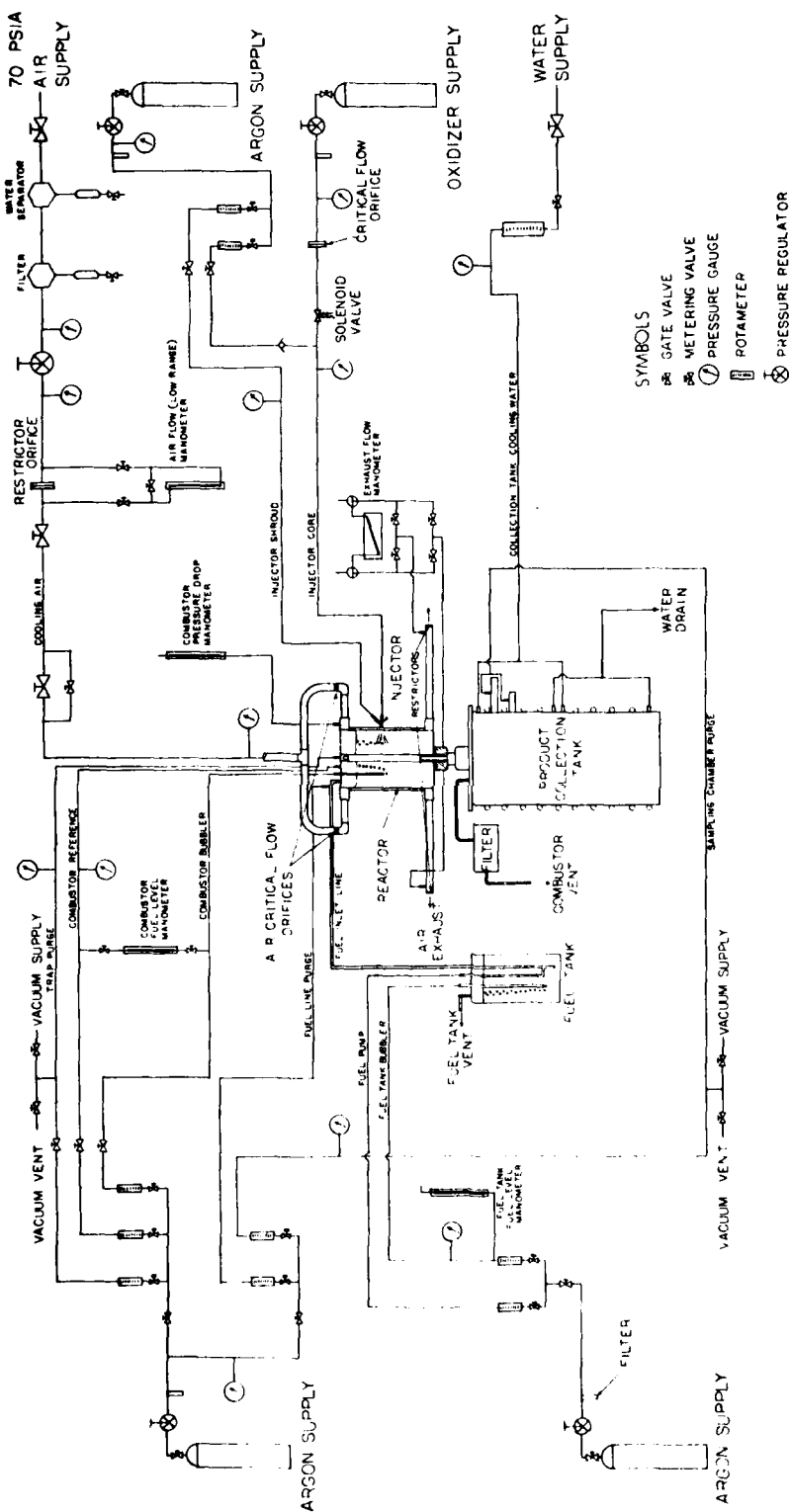


Figure 11 Flow Control System

system were metered with rotameters with the exception of the oxidizer and coolant air flows which were metered with critical flow orifices.

4.3 Radiative Combustor Apparatus

The fuel tank, fuel pump and control system were common to both the radiative and air-cooled combustors and are described in Section 4.2.

4.3.1 Reaction Chamber. The reaction chamber was fabricated from six inch standard I.P.S., schedule 10, type 316 stainless steel pipe, nominally 16.5 cm in diameter and 46 cm in length. The energy released by the reaction was removed by convection and radiation from the side walls of the reaction chamber. The coaxial injector used to inject oxidizer into the reaction chamber and the trap system used to remove reaction products are similar to the air-cooled combustor and a discussion of these components is found in Section 4.2.1. The product-rich liquid was contained within the main reaction chamber at a depth of 15 cm in early tests and 7.5 cm in later tests. The large product-rich liquid volume permitted accurate measurements of the density of this phase to be obtained.

Three 1.5 kW electrical bead heaters, manufactured by the Cole-Parmer Instrument Company (model 3116-40), were installed on the reaction chamber walls in order to heat the fuel to the molten state prior to ignition. Two of the heaters were turned off following ignition, but the heater installed in the trap area was controlled manually during a test to balance the parasitic heat loss from this region.

The exterior surfaces of the reaction chamber were insulated with approximately a 5 cm layer of Fiberfrax Lo-Con ceramic fiber blanket. The energy release rate from the reaction chamber was controlled by manual adjustment of the amount of insulation on the reaction chamber walls.

4.3.2 Product Collection Tank. The product collection tank was fabricated from 10 inch standard I.P.S., schedule 10, type 316 stainless steel pipe, nominally 27.3 cm in diameter and 61 cm in length. The tank was fitted with removable end plates on both ends to facilitate post-run removal of the reaction products. The reaction chamber was mounted to the collection tank by a bolted flange sealed with a ceramic fiber gasket.

4.4 Instrumentation

4.4.1 Flow Measurement. All argon flows to the system were metered with rotameters manufactured by Matheson Gas Products. Rotameter tube sizes varied depending on the magnitude of the particular flow being measured. The largest argon flow to the system was through the coaxial injector where a No. 604 tube was utilized. All rotameters were calibrated with a Precision Scientific Company wet-test meter (0.10 cu. ft./rev.).

The oxidizer flow was metered and controlled with a critical-flow orifice-pressure regulator combination. The pressure regulator was a Matheson model 9 two-stage regulator with a 0-300 psig output capability. The pressure upstream of the critical flow orifice was measured with a Heise absolute pressure gauge with a 0-300 psia

capacity. The orifice was calibrated with a Precision Scientific Company wet-test meter (0.25 cu. ft./rev.)

The coolant air flow measurement system was divided into low and high range sections. The low-range section consisted of a calibrated 1.78 cm (0.70 inch) diameter flow orifice manufactured by the American Meter Company (model 22092). The pressure drop across the orifice was measured with a Heise absolute pressure gauge with a 0-300 psia capacity. The high-range section consisted of two critical flow orifices installed in the heat exchanger inlet lines. The low-range and high-range systems were designed so that choked flow occurred in the orifices when the air flow exceeded the capacity of the low-range section. Flow through the critical flow orifices was then metered by measuring the upstream pressure on the line pressure gauge described earlier. Flow through the system was controlled with a pressure regulator manufactured by the Airline Hydraulics Corporation (Componetrol model 420324-5). Both the low-range and high-range sections were calibrated with a positive-displacement rotary meter manufactured by the Roots-Connersville Blower Corporation (0.2633 cu. ft./rev.).

A 4.44 cm diameter flow orifice was installed in the exit plane of each air exhaust line. The pressure drop across the orifices in each line was measured to allow corrections to be made should the flows in each leg become unmatched during the thermal performance tests. Pressures were measured with an Ellison 4-inch inclined manometer. The total pressure drop through the heat exchanger and exhaust lines were measured with a Merriam 30-inch manometer (model RC 1418).

4.4.2 Temperature Measurement. Temperatures were measured with chromel-alumel thermocouples. The reaction chamber bath temperature was measured at two different depths with four grounded, type 316 stainless steel-sheathed thermocouples manufactured by the Conax Corporation (P/N's K-3165512-G-T1-12 and K-3165512-G-T1-18). The exhaust air temperatures were also measured with Conax grounded, type 316 stainless steel-sheathed thermocouples (P/N K-316556-G-PJ-MX-062-A-3). Two thermocouples were positioned in the center of each exhaust leg. The surface temperature of various components in the apparatus were measured by spot-welded thermocouples fabricated from wire manufactured by the Thermo-electric Company, type G/G-26-K. All thermocouples were manufactured to the American National Standards Institute limits of error. In the temperature range of use, the error limit is ± 0.75 percent.

Temperatures were recorded every eighteen seconds on three Leeds and Northrup Speedomax-H twelve-point, null-balance recorders. The extension leads and recorders were calibrated with a Leeds and Northrup model 8686 millivolt potentiometer. The temperature-millivolt conversion values were taken from National Bureau of Standards tables.

4.4.3 Fuel Level Measurement. The fuel levels in both the reaction chamber and fuel tank were measured with argon bubblers located at known positions in the respective vessels. A low flow of argon (approximately 0.03 kg/hr) was supplied to the bubbler, and the inlet pressure was measured on a manometer. The frictional losses in the bubbler were negligible and therefore the manometer

measured the fuel head at the bubbler exit. An Ellison 8-inch manometer and a Merriam 35-inch manometer (model RB 1418-1) were used to measure bubbler inlet pressures in the reaction chamber and fuel tank, respectively. Knowledge of the bath liquid densities allowed the pressure measurements to be converted to depth readings.

4.4.4 Sampling System. Fuel-rich bath liquid samples were obtained for analysis by lowering a sample cup held by a long-handled sampling probe through the fuel sampling port at the top of the apparatus. The probe was fabricated from type 316 stainless steel and consisted of a support for the sample cup and a movable ball which acted as a filling valve. The sample cup was fabricated from nickel 200 alloy, and had an outside diameter of 1.3 cm and a length of 2.5 cm. During the course of the investigation it was found that sample cups fabricated from either stainless steel or low-carbon steel resulted in sample contamination believed to be caused by surface corrosion of the material by the lithium sulfide. The probe and sample cup apparatus were similar to that used by Avery [22].

The sample cup was placed in the sampling probe and sealed with the ball to prevent contamination prior to being filled with the melt. After the sample was taken, the cup was again sealed with the ball to prevent sample contamination during retrieval.

Product-rich bath liquid samples were obtained by sampling the product flowing out the trap. The sample was taken by extending a sampling cup through the sample chamber into the product flow path. Figure 3 shows the product sampling cup in sampling position. The cup

was fabricated from type 316 stainless steel and had a semicircular cross section with an outside diameter of 3.18 cm and a length of 7.62 cm.

4.5 Experimental Procedure

4.5.1 Reactants. The lithium fuel used in the experimental program was produced by the Lithium Corporation of America. The fuel was packed in two-pound cans and sealed under argon. The purity is listed in 99.9% with the major impurity being sodium.

The sulfur hexafluoride oxidizer was produced by Matheson Gas Products. The gas was contained in a cylinder as a liquid under its own vapor pressure (2200 kPa at 294°K). The gas was certified purity grade with a listed purity of 99.8%.

4.5.2 Pre-Test Preparation Procedure. Prior to the start of the combustion process, the reaction chamber including the sumps and outflow duct were heated electrically to approximately 1030°K. Ignition could be initiated at any temperature above the melting point of lithium, 453°K, but the higher temperature was chosen to shorten the low-temperature transient period of the run. The fuel tank and fuel line were heated electrically and stabilized at a temperature of 540°K. During the heat-up period all argon flows to the system were operational including a purge flow of argon through the core tube of the coaxial injector.

4.5.3 Normal Operating Procedure. The combustion process was started by actuation of a solenoid valve which supplied oxidizer to the injector. The argon purge flow to the injector core tube was

terminated immediately after start. The bath temperature was allowed to increase to the desired operating value, and the oxidizer and air flow were then matched to stabilize the temperature.

The oxidizer flow was adjusted to the desired power level, and the argon flow to the lift pump was adjusted to yield the stoichiometric fuel flow rate. The fuel flow rate was not measured directly, but was monitored by observing the fuel level in the reaction chamber through the use of the fuel level manometer. Correct matching of the fuel and oxidizer flow rates was indicated by a constant fuel level in the reaction chamber. The fuel level in the remote fuel tank was maintained by the manual addition of solid fuel to the tank. The coolant air flow to the system was adjusted at each power level to maintain the bath temperature at the desired value.

The combustor was operated at a particular power level-bath temperature condition for sufficient time to ensure the establishment of thermal and chemical equilibrium in the reaction chamber. The design of the combustor facilitated the establishment of chemical equilibrium since the product-rich liquid contained in the combustor sump could be exchanged relatively rapidly (approximately 0.54 hours at a power level of 10 kW). Additionally, the fuel-rich phase was easily saturated with products since the bath was stirred by the oxidizer jet, and the combustion process was occurring within the fuel-rich phase. Both fuel-rich and product-rich liquid samples were obtained over a range of temperatures by gradually increasing the bath temperature over the course of the run.

The oxidizer flow, shroud argon flow, fuel pump argon flow, coolant air flow, fuel tank and reaction chamber fuel levels, combustor pressures, and system temperatures were continually monitored and recorded throughout a test. The data were later reduced to determine system performance.

The combustion process was terminated by actuating the oxidizer solenoid valve to the closed position. An argon purge flow through the injector core tube was initiated just prior to termination of the oxidizer flow.

4.5.4 Post-Test Shutdown Procedure. After the oxidizer flow was terminated, the coolant air flow was reduced to a low value to allow gradual cool-down of the apparatus. The product collection tank was removed from the apparatus after the system had completely cooled, and the reaction products were removed from the collection tank. The product exhaust duct region of the apparatus was inspected, and the collection tank was reinstalled on the apparatus. The injector and fuel level bubbler were removed and inspected; the parts were replaced if necessary.

4.5.5 Bath Sampling Procedure. Product-rich and fuel-rich bath samples were extracted with the apparatus described in Section 4.4.4.

A product-rich sample was allowed to cool in the sample chamber under an argon purge prior to final removal from the apparatus. The sample was then cracked loose from the sample cup into a stainless steel tray, and transferred to a sealed glass container.

A fuel-rich sample was removed from the reaction chamber through the sample port at the top of the combustor. The combustion between the lithium on the outside of the sample cup and the ambient air was extinguished and the residue removed from the outside of the cup by quenching in water. The sample cup was held in the sample probe during this period and sealed by the probe ball valve to prevent sample contamination. The sample cup was then removed from the probe and transferred to a sealed glass container.

The sealed glass containers containing the samples were evacuated in the antechamber of a vacuum/glove box. The containers were then transferred to the main chamber of the glove box and stored under a low humidity, argon atmosphere for future chemical analysis.

4.5.6 Bath Sample Analysis Procedure. The fuel-rich samples were prepared for analysis by cleaning the remaining scale from the outside of the cups with fine emery cloth. The polished cups were weighed with an analytical balance manufactured by Ainsworth, Incorporated, type L C 28948. The cups were reweighed following the analysis of the samples to obtain the sample weight by difference.

The product-rich samples were prepared for analysis by grinding the entire sample to an extremely fine powder with a model 7875 Micro-Mill manufactured by The Chemical Rubber Company. A portion of the powdered sample was weighed on the analytical balance described earlier and then subjected to the analysis procedure. All the cleaning, grinding and weighing operations were conducted within the

low humidity, argon atmosphere glove box to prevent sample contamination.

The details of the wet-test chemical analysis procedures used to analyze the samples are described in Appendix D.

4.5.7 Bath Density Measurement Procedure. The densities of both the fuel-rich and product-rich liquids were obtained over a range of temperatures. The radiative combustor described in Section 4.3 was utilized to generate the density data. The product-rich liquid was contained in the bottom of the cylindrical reaction chamber in the radiative combustor. The design permitted direct access to both the fuel-rich and product-rich liquids from the sampling port provided in the top of the combustor.

The measurements were made by lowering a bubbler (similar to the fuel level bullers previously described in Section 4.4.3) through the sampling port into the bath with the pressure being measured every 1.27 cm. The pressure was measured with a Merriam manometer (model RC 1418) filled with Merriam unity oil (specific gravity = 1.00). The reaction chamber pressure was referenced to the low pressure side of the manometer; therefore, the manometer measured liquid head above the bubbler tip. A series of readings were obtained as the bubbler was lowered, with approximately 15-22 readings taken in the fuel-rich liquid and 5-10 readings in the product-rich liquid. A linear least squares curve fit was made to the pressure readings; the slope of this curve yields the density. A change in slope was noted when the product-rich liquid was entered, and the point where the slope changed provided a measure of the product-rich liquid level.

4.5.8 Thermal Performance Measurement Procedure. The thermal performance measurements were made by measuring the enthalpy rise and flow rate of the coolant air as a function of oxidizer flow rate for a bath temperature of $1197 \pm 3^\circ\text{K}$. The temperature was chosen because it is in the middle of the normal operating range of the combustor. The single temperature was examined because the thermal performance is not significantly affected by bath temperature in the temperature range of interest.

For a given oxidizer flow rate, the coolant air flow rate was adjusted to maintain the constant bath temperature. The air and wall temperature of each exhaust leg were measured and recorded. The exhaust air temperatures were corrected for errors caused by conduction and radiation to the walls by employing the procedures presented by Moffat [44]. The dominant effect was radiation, with corrections in the range of 1-5% resulting for the different flow conditions. Minor flow mismatches in the exhaust legs were accounted for by applying corrections generated from data on the pressure drops across the exhaust orifices. Flow mismatches on the order of 5% were encountered at the highest flows. The combustor was operated for a period of one hour at each power level. Minor variations in the air flow rate and air exit temperature over the hour period were accounted for by taking mean values. The enthalpy change of the air was obtained by integrating the cubic expression for the specific heat at constant pressure of air given in Reference [45] from the inlet temperature to the exit temperature. The enthalpy change of each exhaust leg was multiplied by the flow rate of that leg and

then added to yield the total power input to the coolant air load.

The electrical power inputs to the system were independent of load and were therefore included with the parasitic heat loss from the system which includes all heat flows not transferred to the working fluid of the heat exchanger. Both the energy release rate of the combustor and the net average parasitic heat loss from the combustor were obtained from a plot of heat exchanger load in kW versus oxidizer flow rate in kg/hr. The slope of the curve yielded the energy release rate in kW-hr/kg of oxidizer. The negative intercept on the load axis yielded the net average parasitic heat loss from the system in kW. The gross parasitic heat loss equals the net parasitic heat loss plus the electrical input to the system of approximately 1.9 kW.

CHAPTER V

EXPERIMENTAL AND THEORETICAL RESULTS

5.1 General Experimental Observations

5.1.1 Radiative Combustor Tests. The objectives of the radiative combustor test program were to generate bath liquid density data and to examine several design details which had to be resolved before the design of the more complex air-cooled combustor could be completed. A total of eight tests were conducted, as summarized in Table 1.

Test LSR-1 indicated that a guard heater was required in the trap area of the combustor to balance the parasitic heat loss from this zone, and larger crossover ports were needed in the trap shroud tube. Product outflow was not achieved during the test because the trap area could not be maintained at a temperature above the solidification temperature of the product. These design changes proved to be satisfactory during test LSR-2, but an additional difficulty was encountered with the type 321 stainless steel hydroformed bellows used as the product exhaust duct. The bellows was found to be plugged with product material and severely corroded. To eliminate the problem, the trap area was redesigned to provide a cylindrical product exhaust duct fabricated from type 316 stainless steel, along with a modified inner trap tube which included a lip to direct the product flow away from the exhaust duct walls. No problems were encountered with the modified combustor during test LSR-3 which was run for a total of 7.1 hours. The final design

Table 1

Summary of Radiative Combustor Tests

Run Number	Run Length (hours)	Oxidizer Flow (kg/hr)	Maximum Bath Temperature (°K)	Comments
LSR-1	2.0	0.26-1.21	1264	No product outflow because trap area clogged with solidified product.
LSR-2	1.5	0.31-1.22	1261	Test terminated after leak developed in bellows connection in product exhaust duct.
LSR-3	7.1	0.14-0.88	1233	Redesigned product exhaust duct functioned well with no clogging problems encountered.
LSR-4	1.3	0.32-0.88	1177	Test terminated after problems were encountered with the bath density measurement apparatus.
LSR-5	7.1	0.0-0.95	1272	Bath densities measured in the temperature range of 1172-1255°K.
LSR-6	5.6	0.0-2.25	1219	Argon lift pump used to supply fuel to the reaction chamber. Bath densities measured in the temperature range of 1144-1200°K.
LSR-7	3.2	0.0-0.83	1297	Argon lift pump used to supply fuel to the reaction chamber. Bath densities measured in the temperature range of 1236-1280°K.
LSR-8	4.5	0.0-2.77	1252	Demonstrated extended high power operation. Bath densities measured at 1177°K.

modifications to the combustor were made following test LSR-6. Minor difficulties were encountered with product liquid freezing to the exhaust duct walls in the region where the duct was connected to the product collection tank. The duct diameter was increased in this region to minimize the possibility of product flow contacting the walls. The inner trap tube was also shortened to provide a lower product level in the combustor.

The first attempt to obtain bath density data was made during test LSR-4, but a malfunction of the density measurement apparatus caused the test to be terminated early. The density measurement apparatus was modified and functioned properly during test LSR-5 which was run for a total of 7.1 hours. The long-term operation experienced during LSR-5 provided further substantiation of the design modifications described earlier. Additional density data were obtained during all subsequent radiative combustor tests.

The operation of the argon lift pump used to supply fuel to the reaction chamber was evaluated during the final three radiative combustor tests, LSR-6, LSR-7 and LSR-8. Prior to test LSR-6, the fuel had been added to the combustor manually as solid sticks. It was found that the performance of the pump was adversely affected by small positive pressure differentials between the reaction chamber and the fuel tank, and the argon exhaust line from the product collection tank was enlarged to decrease the combustor pressure.

Test LSR-8 was conducted to demonstrate long-term operation at power levels greater than 11 kW. Figure 12 illustrates a portion of the data obtained from the test. A power level greater than 11 kW

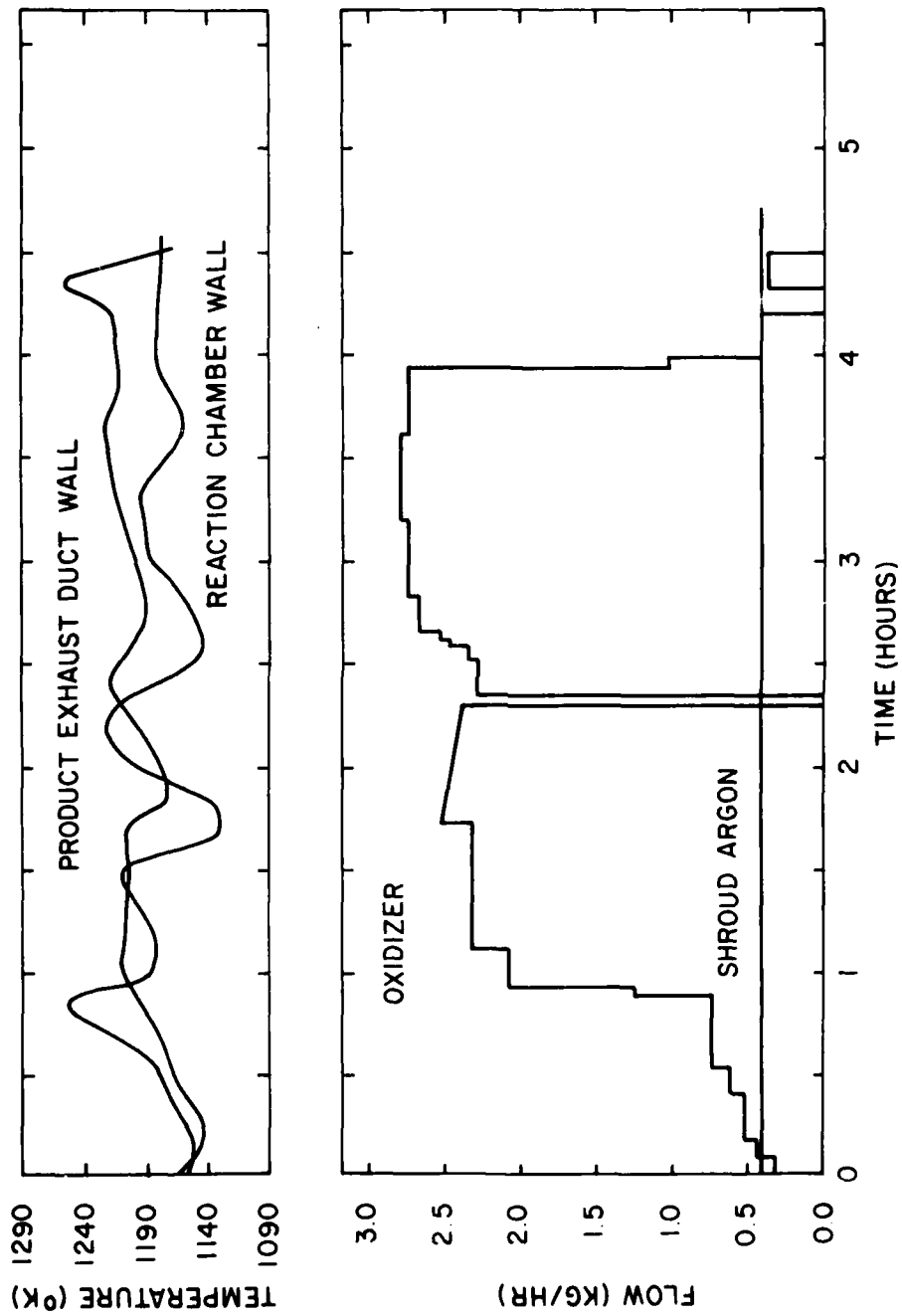


Figure 12 Radiative Combustor Run Data (Test LSR-8)

was maintained for over three hours, with the power exceeding 13 kW for one hour. An idel period was necessitated midway through the high power period while repairs were made to a failed oxidizer control regulator. The rather large fluctuations in the combustor wall temperature and the product exhaust duct wall temperature shown in Figure 12 were caused by the fact that the combustor was radiatively cooled which resulted in the power output of the combustor being strongly affected by small fuel level changes. Also shown in the figure are the oxidizer flow rate as a function of time and the corresponding injector shroud argon flow.

5.1.2 Air-Cooled Combustor Tests. Table 2 summarizes the ten air-cooled combustor tests which were conducted. The main objectives of the tests were to generate bath liquid solubility and thermal performance data, and to demonstrate long-term system operation under steady-state conditions.

Tests PPC-1 and PPC-2 indicated the need for a change to the combustor trap design. It was found that the top of the combustor, including the region of the shroud tube crossover port, could not be maintained at bath temperature; which resulted in condensed lithium and product vapors forming a liquid slug inside the trap shroud tube. The slug formation was enhanced by the exhaust argon flow causing condensed vapors to be directed into the tube, the high surface tension of liquid lithium permitting the size of the slug to be large, and the fact that the shroud tube itself was below bath temperature. The net effect of the slug formation was to cause the combustor ullage region pressure to exceed that of the shroud tube

Table 2

Summary of Air-Cooled Combustor Tests

Run Number	Run Length (hours)	Oxidizer Flow (kg/hr)	Coolant Flow (kg/hr)	Maximum Bath Temperature (°K)	Maximum Power Level (kW)
PPC-1	2.4	2.26	22.0-84.9	1208	10.8
PPC-2	2.6	0.90-2.27	31.8-43.0	1213	10.8
PPC-3	1.4	2.27	20.1-48.8	1225	10.8
PPC-4	3.8	0.75-2.25	0.0	1210	10.7
PPC-5	2.5	0.75-1.88	16.4-37.7	1172	8.9
PPC-6	0.9	0.76	0.0	1161	3.6
PPC-7	2.8	0.56-1.13	0.0	1238	5.4
PPC-8	5.2	0.47-1.13	0.0	1255	5.4
PPC-9	6.3	1.31-4.96	18.0-109.	1205	23.6
PPC-10	10.0	1.11-5.29	11.0-127.	1205	25.2

during the period of time the slug was moving through the shroud tube. The pressure mismatch upset the hydrostatic balance of the combustor trap which resulted in the loss of the product liquid in the trap and ultimate trap failure. Normal trap operation had occurred in both tests prior to the slug formation.

Several factors existed which made the air-cooled combustor more sensitive to slug formation than the radiative combustor, which never showed signs of this problem. The factors include: a) a greater argon flow into the combustor ullage region; b) a longer shroud tube length; and c) a smaller product liquid volume. The greater argon flow rate resulted in a larger rate of product outflow during the pressurization period, and the longer shroud tube increased the period as the slug had to move a greater distance. The two effects were magnified for the air-cooled combustor, due to the smaller product volume which could be outflowed before the trap failed.

Tests PPC-3 and PPC-4 were run with a spot heater installed in the crossover port area to maintain the temperature of the region close to bath temperature. Both tests were terminated when failures of the heater occurred. It was found that the spot heater could not maintain the top of the combustor at bath temperature when coolant air was applied to the system, and the condition led to failure of the trap as described above during test PPC-5. The initial design of the combustor did not permit the proper installation of a spot heater. Alternate methods of installation were tried on tests PPC-6, PPC-7 and PPC-8, all of which forced the tests to be terminated when the heaters failed. The three tests were run at low power levels

which permitted the argon flow to the system through the coaxial injector to be reduced, and eliminated the need for coolant air flow. No problems were encountered with the trap during the tests, but it was evident that a design change would be needed before the system could be operated at higher power levels.

Bath liquid samples were obtained during tests PPC-2 through PPC-8. The samples were analyzed following each test, and excellent agreement was obtained between samples obtained from the different tests.

The combustor was modified prior to the final two tests to the configuration described in Section 4.2. Tests PPC-9 and PPC-10 were conducted to complete the remaining test objective of measuring the thermal performance of the system.

Power levels of 6.2, 12.8, 19.4, 21.3, and 23.4 kW were examined during test PPC-9 by operating at each condition for one hour. The oxidizer flow, coolant air flow, bath temperature, exhaust air temperature, and mean cycle load for the test are plotted in Figure 13 as a function of time. The coolant air flow was adjusted at each test condition to maintain the bath temperature at $1197 \pm 3^\circ\text{K}$. A total of 19.14 kg of oxidizer and 7.25 kg of fuel were consumed during the test. The test was terminated when all test objectives were met.

Additional performance data were obtained during test PPC-10 by operating for one hour periods at power levels of 7.2, 8.2, 10.1, 12.5, 13.9, 15.3, 20.5, and 23.9 kW. The test was unique in that both the longest run time, 10 hours, and highest power output, 25.2

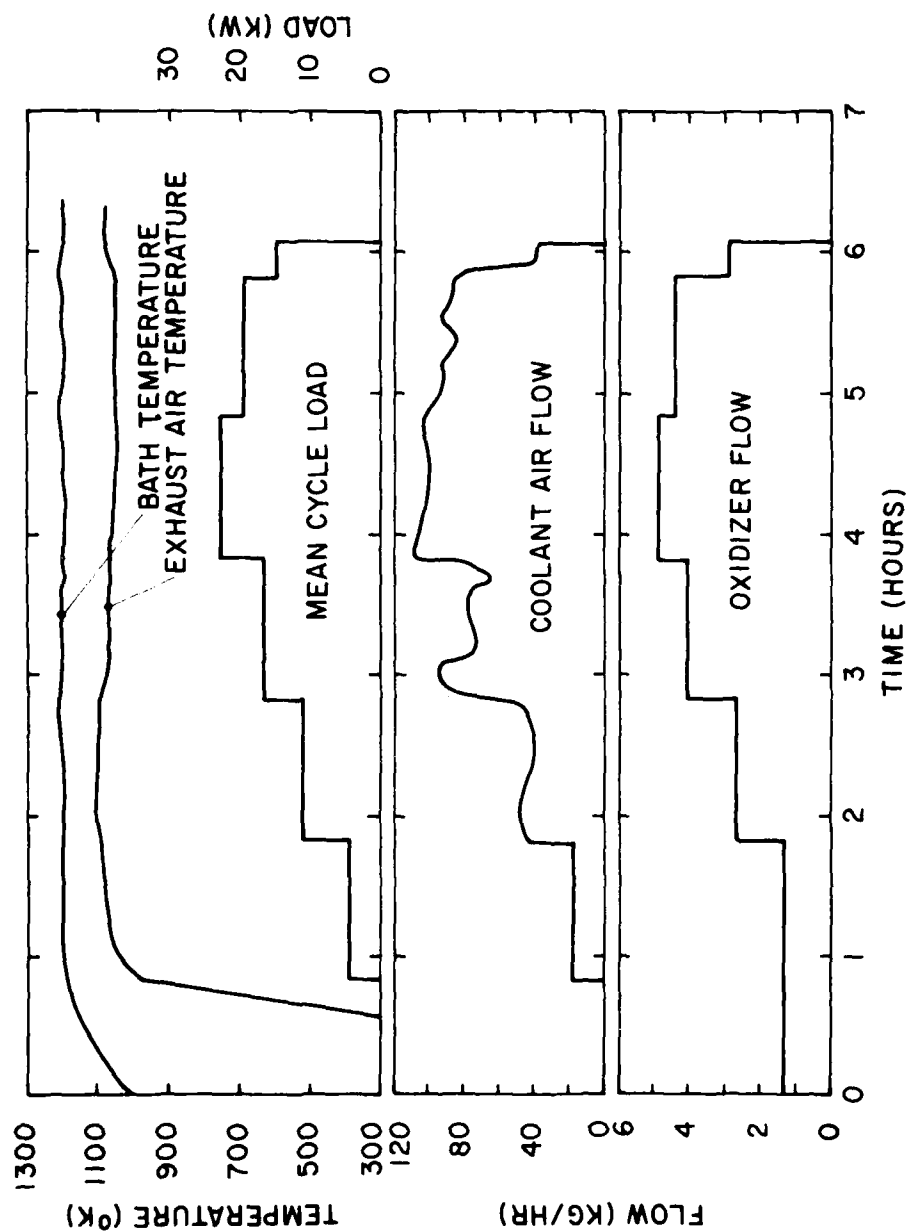


Figure 13 Air-Cooled Combustor Run Data (Test PPC-9)

kW, were achieved during this test. Figure 14 presents the oxidizer flow, coolant air flow, bath temperature, exhaust air temperature, and mean cycle load for the test plotted versus time. The coolant air flow was adjusted at each condition to maintain the same bath temperature examined in test PPC-9, $1197 \pm 3^\circ\text{K}$. A total of 26.4 kg of oxidizer and 10.0 kg of fuel were consumed during the test, and the test was terminated when all the objectives were met. The performance data obtained during test PPC-10 agreed well with the data obtained during test PPC-9.

5.1.3 Nature of the Reaction Products The reaction products produced during the radiative and air-cooled combustor tests were collected by a dry-tank collection method where the products are exhausted into a tank originally empty at the start of the test. Figure 15 is a photograph of the product material collected during test PPC-9. The products formed a stalagmite formation extending from the bottom of the tank to a height of approximately one meter. The mass of the product shown in Figure 15 was approximately 25 kg. The product formation produced during test PPC-9 was typical of the formations produced during other tests.

An alternate method of product collection is the wet-tank collection method where the products are exhausted into the fuel tank containing the molten fuel. Such a method is possible because the volume of the reaction products is less than the volume of the fuel. The method would result in a reduction in overall system volume. The wet-tank collection method was not investigated in an actual combustor, but was investigated using the apparatus described

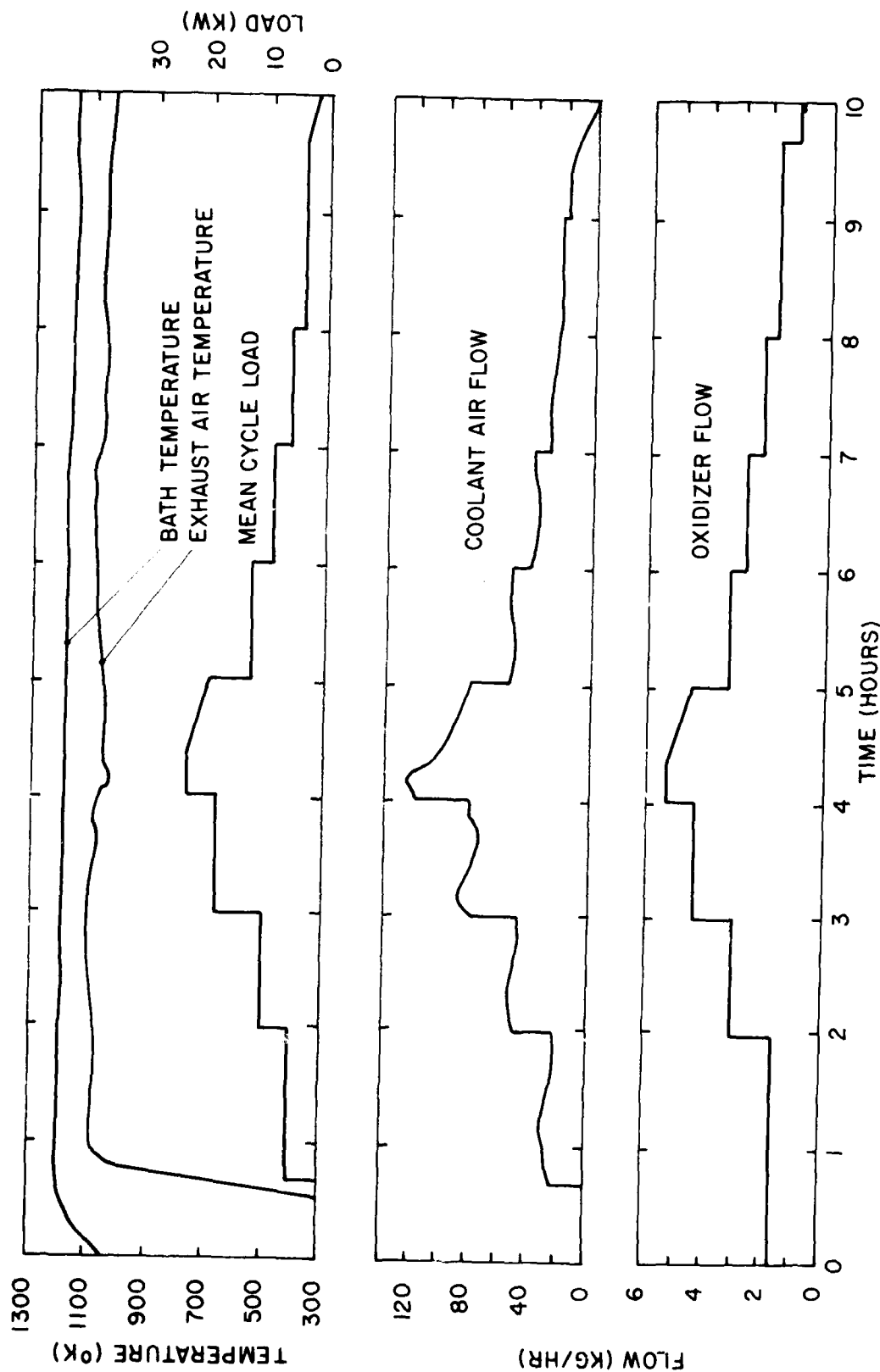


Figure 14 Air-Cooled Combustor Run Data (Test PPC-10)

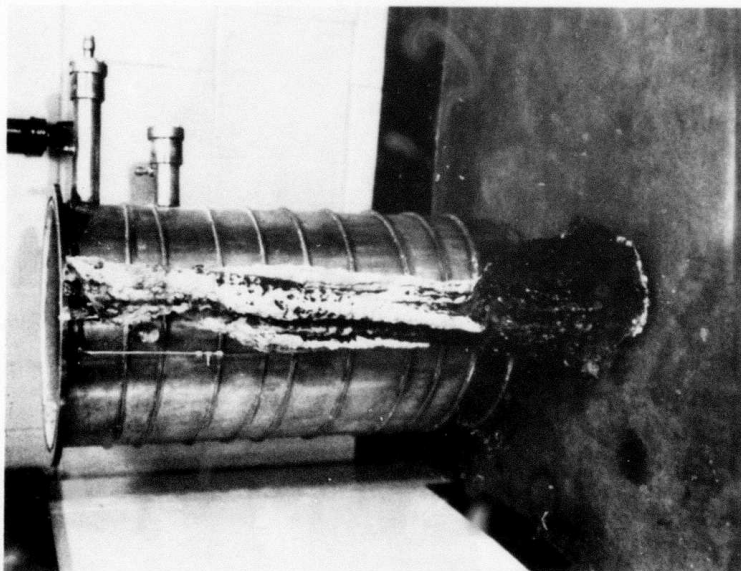


Figure 15 Photograph of Reaction Products

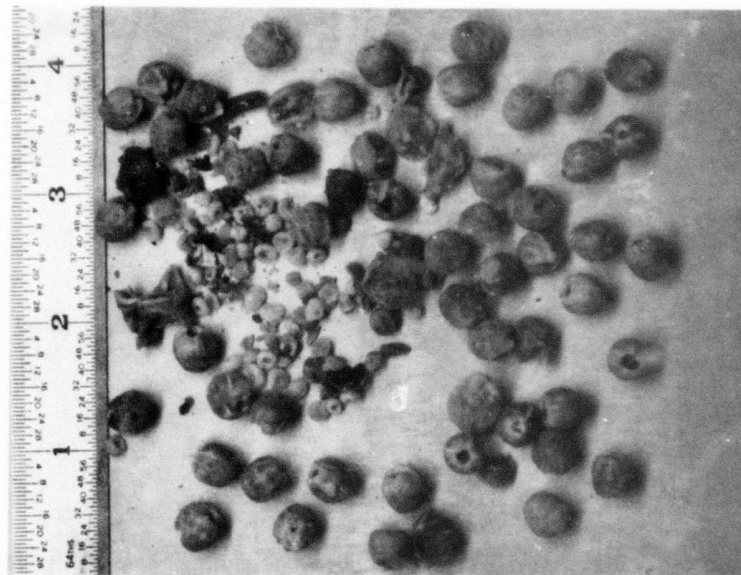


Figure 16 Photograph of Wet-Tank Reaction Products

in Appendix F. The form of the product collected with a wet-tank collection method is shown as a photograph in Figure 16. The products formed spherical balls approximately 0.9 cm in diameter. The packing efficiency of the balls was approximately 50% on a volume basis.

5.2 Liquid Phase Solubility Results

The theoretical and experimental solubility results for the fuel-rich phase are shown in Figure 17 as mole fraction lithium fluoride and lithium sulfide plotted versus temperature with the remainder of the phase consisting of pure lithium. The experimental data is presented in Table 3. The data taken from different combustor runs are distinguished by different symbols in the figure, and it is seen that the agreement between the different data is good. The theoretical results obtained from the thermodynamic model described in Chapters II and III are shown as solid lines in Figure 17 for the case employing the high value for the heat of fusion of lithium sulfide, 49.4 kJ/mole, and as a dashed line for the case employing the low value for the heat of fusion, 7.24 kJ/mole. The results for the two cases agreed within 0.6% for the lithium fluoride component. The agreement between the theoretical predictions and the experimental data is good. The maximum error in the lithium fluoride solubility prediction is approximately 25% and occurs at the low temperature end of the temperature range examined. The maximum error in the lithium sulfide solubility prediction is approximately 39% for the high heat of fusion case, and occurs at the high temperature end of the temperature range. The error for the low heat of fusion case remains relatively constant at a value of approximately 50%. Both

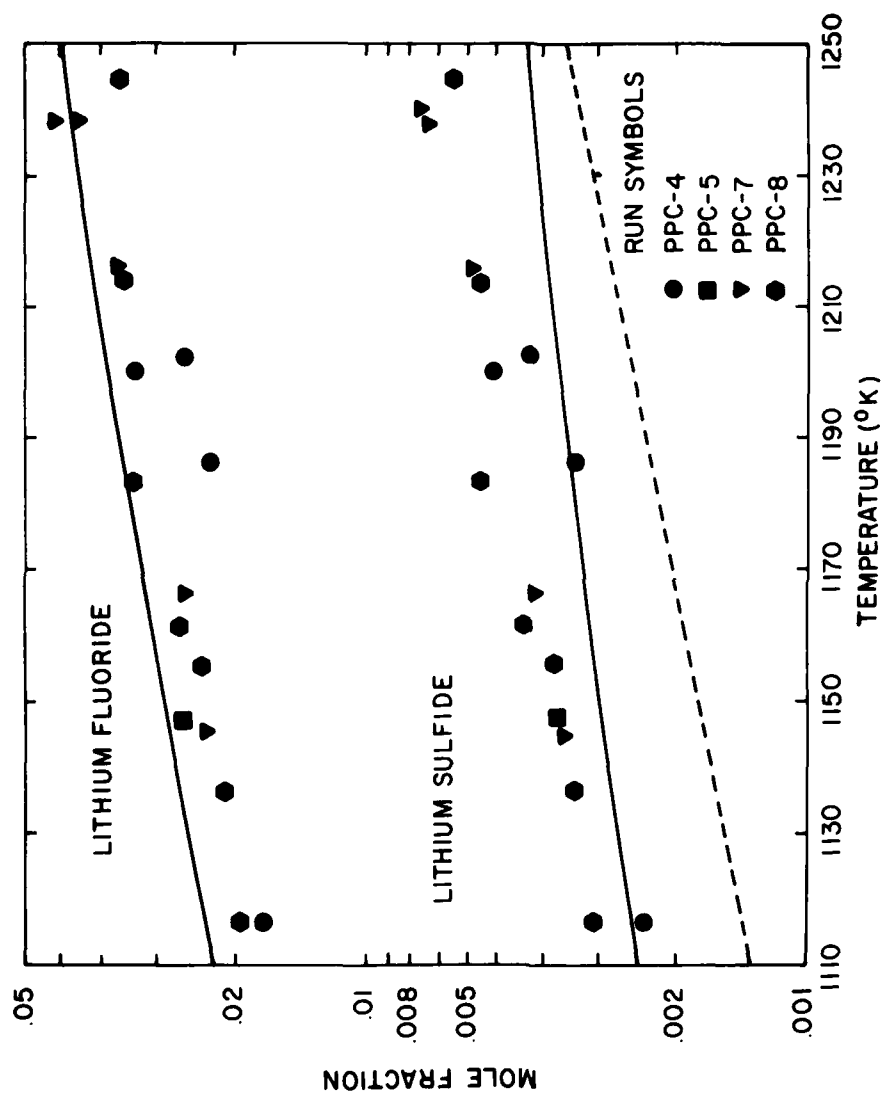


Figure 17 Fuel-Rich Liquid Solubilities

Table 3

Fuel-Rich Liquid Solubility Data

Test Number	Temperature (°K)	Lithium Mole Fraction	Lithium Fluoride Mole Fraction	Lithium Sulfide Mole Fraction
PPC-4	1116	0.980	0.0172	0.00233
PPC-8	1116	0.977	0.0196	0.00309
PPC-8	1136	0.976	0.0209	0.00334
PPC-7	1145	0.974	0.0228	0.00357
PPC-5	1147	0.971	0.0255	0.00364
PPC-8	1155	0.973	0.0236	0.00372
PPC-8	1161	0.970	0.0260	0.00432
PPC-7	1166	0.970	0.0255	0.00401
PPC-8	1183	0.961	0.0338	0.00553
PPC-4	1186	0.974	0.0222	0.00336
PPC-4	1200	0.962	0.0333	0.00502
PPC-4	1202	0.970	0.0259	0.00423
PPC-7	1214	0.959	0.0352	0.00558
PPC-8	1214	0.958	0.0359	0.00554
PPC-7	1238	0.948	0.0448	0.00717
PPC-7	1238	0.944	0.0490	0.00714
PPC-8	1244	0.958	0.0362	0.00630

the experimental data and the theoretical predictions show a gradual increase in lithium fluoride and lithium sulfide solubilities in the fuel-rich phase as the temperature is increased.

Figure 18 compares the theoretical and experimental solubility results for the product-rich phase, and Table 4 presents a summary of the experimental data. The lithium solubility is plotted as mole fraction versus temperature. The ratio of mole fraction lithium sulfide to mole fraction lithium fluoride is plotted versus temperature since the solubility ratio of these two components is controlled by the reaction stoichiometry. The agreement between the experimental data taken from different combustor runs, distinguished by different symbols in the figure, is seen to be good. The theoretical results computed from the two different heat of fusion cases are identical within the accuracy of the plot, and are shown as solid lines. The lithium solubility computed from the low heat of fusion case was approximately 4% lower than the high heat of fusion case at 1110°K and 2% higher at 1250°K. The theoretical predictions are extremely good for the product-rich phase. The lithium solubility is predicted to an accuracy of 5-8% over the temperature range examined. The lithium fluoride-lithium sulfide mole fraction ratio is theoretically exact and any disagreement is caused by scatter of the experimental data. The lithium solubility in the product-rich phase was found to be very low, less than 0.9% on a mole fraction basis, in the temperature range examined, and was found to increase with temperature as expected.

The scatter in the data presented in Figures 17 and 18 could be caused by the following: a) nonequilibrium of the phases when

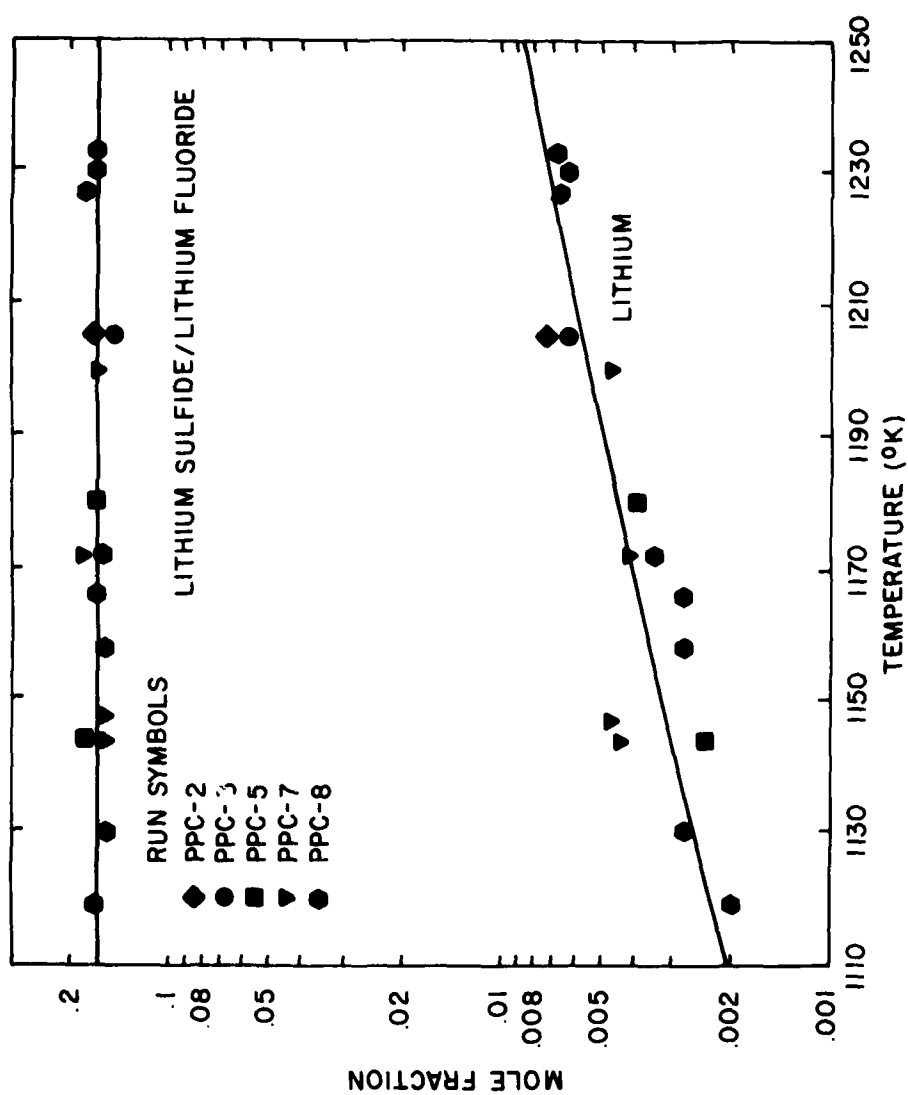


Figure 18 Product-Rich Liquid Solubilities

Table 4

Product-Rich Liquid Solubility Data

Test Number	Temperature (°K)	Lithium Mole Fraction	Lithium Fluoride Mole Fraction	Lithium Sulfide Mole Fraction
PPC-8	1119	0.00200	0.856	0.141
PPC-8	1130	0.00274	0.864	0.133
PPC-7	1144	0.00425	0.865	0.131
PPC-5	1144	0.00235	0.851	0.147
PPC-7	1147	0.00444	0.859	0.136
PPC-8	1158	0.00274	0.864	0.133
PPC-8	1166	0.00278	0.857	0.140
PPC-8	1172	0.00346	0.858	0.138
PPC-7	1172	0.00381	0.857	0.139
PPC-5	1180	0.00380	0.854	0.142
PPC-7	1200	0.00448	0.853	0.142
PPC-3	1205	0.00637	0.868	0.125
PPC-2	1205	0.00675	0.849	0.144
PPC-8	1227	0.00662	0.848	0.145
PPC-8	1230	0.00638	0.850	0.145
PPC-8	1233	0.00665	0.852	0.141

the bath samples were taken; b) the sample composition not representative of the bulk liquid-composition; c) errors in temperature measurement; and d) errors in determining the bath sample composition. As described in Section 4.5.3, precautions were taken during the operation of the combustor to ensure that equilibrium conditions were established in the combustor. A quantitative estimate of nonequilibrium effects is not available, but it is noted that the rate of phase saturation is enhanced by the very low solubilities of the minor components involved in each phase. The accuracy of the thermocouples is listed by the manufacturer to be within approximately $\pm 9^\circ\text{K}$ in the temperature range of interest. The measurement error introduced should be consistent from test to test because the thermocouples used in the different tests were taken from the same production lot. The accuracy with which the recorded temperatures could be read from the chart was estimated to be $\pm 2^\circ\text{K}$. It was concluded that the measurement accuracy of the thermocouples was well within the manufacturer's tolerance since the product eutectic temperature, 1065°K , and the fuel solidification temperature, 453°K , were consistently measured to within the accuracy of the recording chart by observing thermal arrests during post-test cool-down cycles. Errors introduced by the wet-test chemical analysis procedures were found to be small by testing the procedures against prepared samples of known composition. The lithium fluoride and lithium sulfide concentrations in the fuel-rich and product-rich phases were found to be within an accuracy of $\pm 3\%$. The lithium concentration in the product-rich phase was determined to within

an accuracy of $\pm 8\%$. The greatest source of error could not be evaluated quantitatively, but was believed to be caused by the bath samples not representing the bulk phase composition. The composition change could occur after sample removal by small quantities of lithium being lost through the ball valve/sample cup seal in the case of the fuel-rich samples, or by contamination of the samples with extraneous lithium in the case of the product-rich samples.

5.3 Liquid Phase Density Results

The theoretical and experimental densities for both the product-rich and fuel-rich liquid phases are compared in Figure 19. The experimental data are presented in Table 5. The theoretical results for the two cases examined in the analysis (involving different heats of fusion for the lithium sulfide component) are the same within the accuracy of the plot. The largest difference between the two cases is approximately 0.7% for the fuel-rich phase density at 1110°K. The density of the fuel-rich phase was found experimentally to be relatively constant in the temperature range examined. The theoretical result, shown as the solid line in Figure 19, predicts a slight increase in density with temperature and gives values approximately 6% lower than the experimental data in the low temperature region. The agreement in the higher temperature region is within approximately 2%. The lack of temperature dependence of fuel-rich liquid phase density is caused by a balance between the decrease in the density of pure lithium and the increased solubility of the more dense product species with increasing temperature. The product-rich liquid density was found to decrease with increasing temperature. The data agree

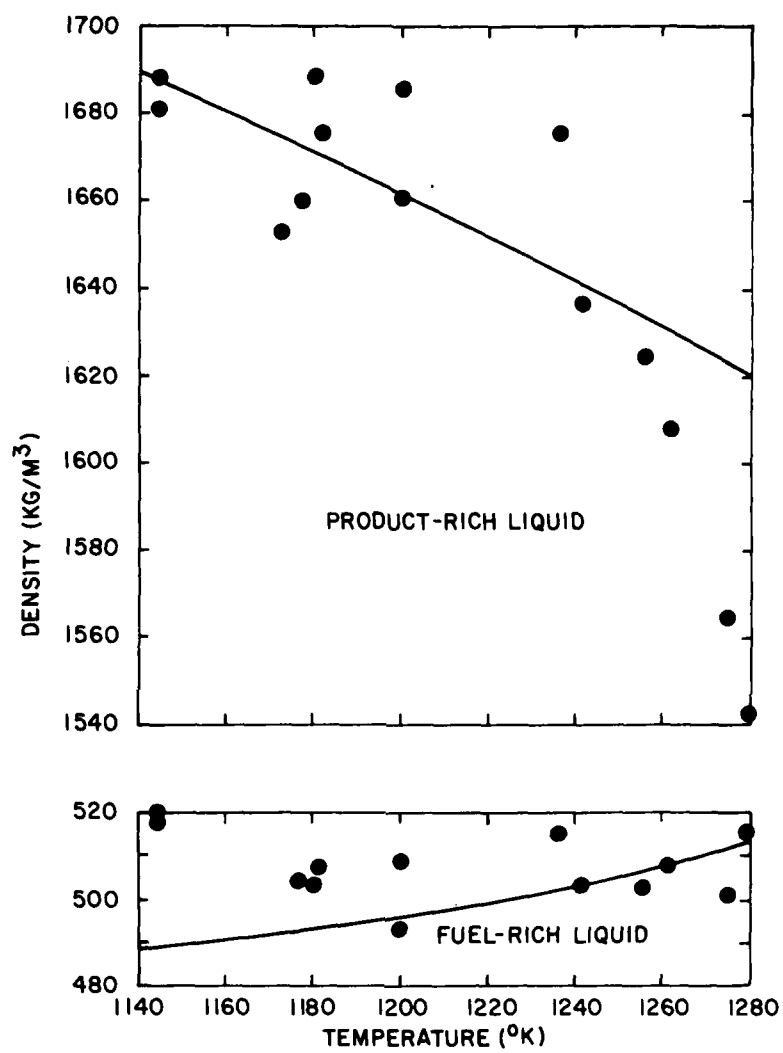


Figure 19 Bath Densities

Table 5

Bath Liquid Density Data

Temperature (°K)	Fuel-Rich Liquid Density (kg/m ³)	Product-Rich Liquid Density (kg/m ³)
1144	518	1690
1144	520	1680
1172	---	1650
1177	504	1660
1180	503	1690
1181	507	1680
1200	493	1660
1200	509	1680
1236	515	1680
1241	503	1640
1255	503	1620
1261	508	1610
1275	501	1560
1280	516	1540

with the theoretical prediction, shown as the solid line in Figure 19, to within $\pm 2\%$ except at the highest temperature where the error reaches a maximum of approximately 5%.

5.4 Gas Phase Partial Pressure Results

The theoretical gas phase partial pressures are presented in Figure 20 as the sum of the partial pressures of various dimer and polymeric species plotted versus temperature. The predictions are effectively unchanged by the value of the heat of fusion of lithium sulfide used in the model; the predictions for the lithium and lithium fluoride species agreeing within 0.1% and the predictions for the lithium sulfide species agreeing within 0.25%. The partial pressures of the individual species were not measured experimentally, but the total pressure was measured during the course of a related study [46]. The method used was to measure the oxidizer inlet pressure to an unvented wick-type pot combustor. The measured pressure was equal to the mixture vapor pressure because the injector was unchoked, and the combustion was occurring off the surface of the wick as a diffusion flame. The experimental total pressure results are compared to the theoretical predictions in Figure 21. The largest differences of 10-15% occur in the low temperature region where the experimental uncertainties were the greatest. The results indicate that the reaction chamber pressure in unvented combustors can vary approximately an order of magnitude in the typical operating temperature range, but in all cases is very low (0.035 bar at 1250°K).

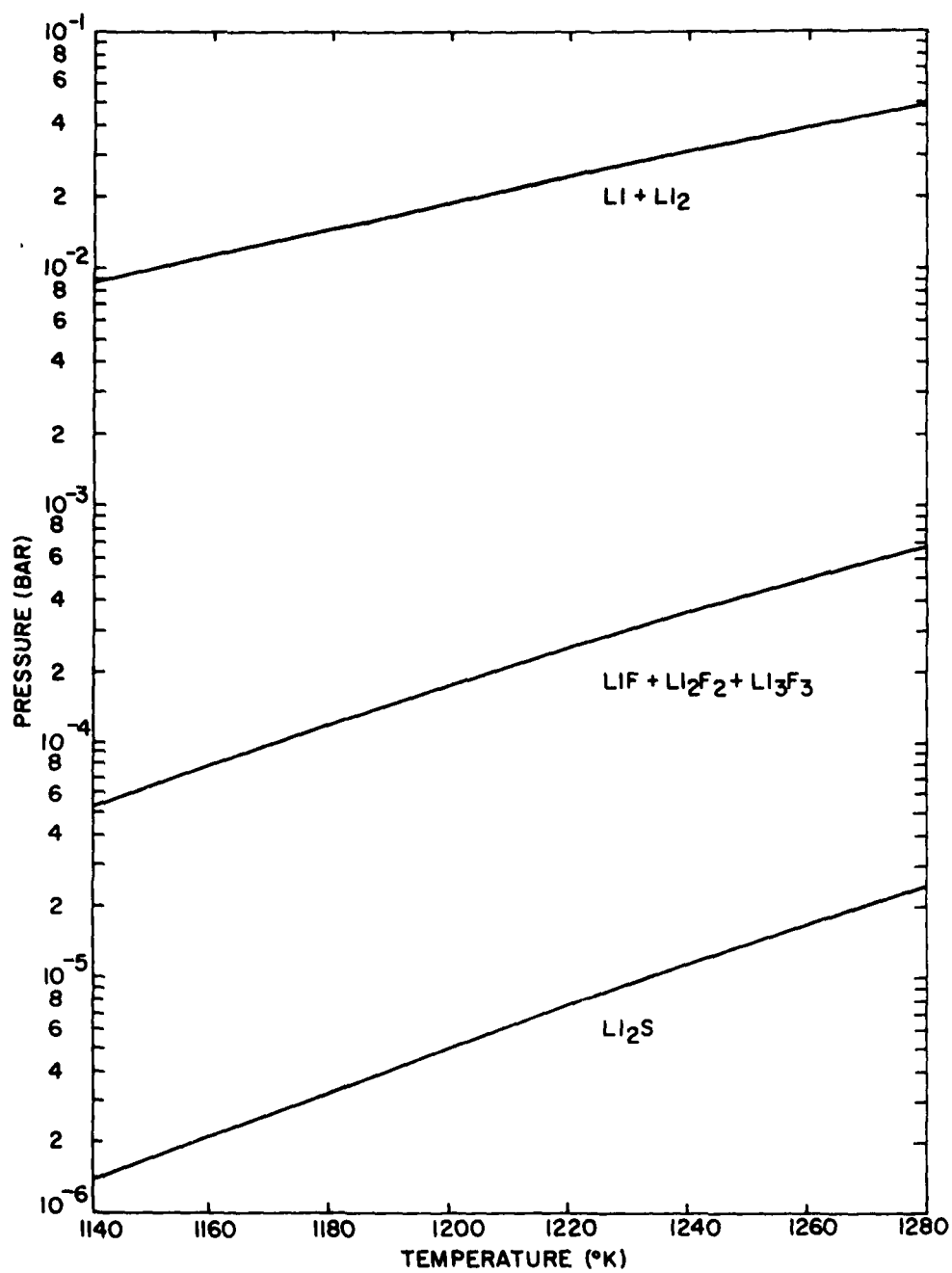


Figure 20 Theoretical Gas Phase Partial Pressures

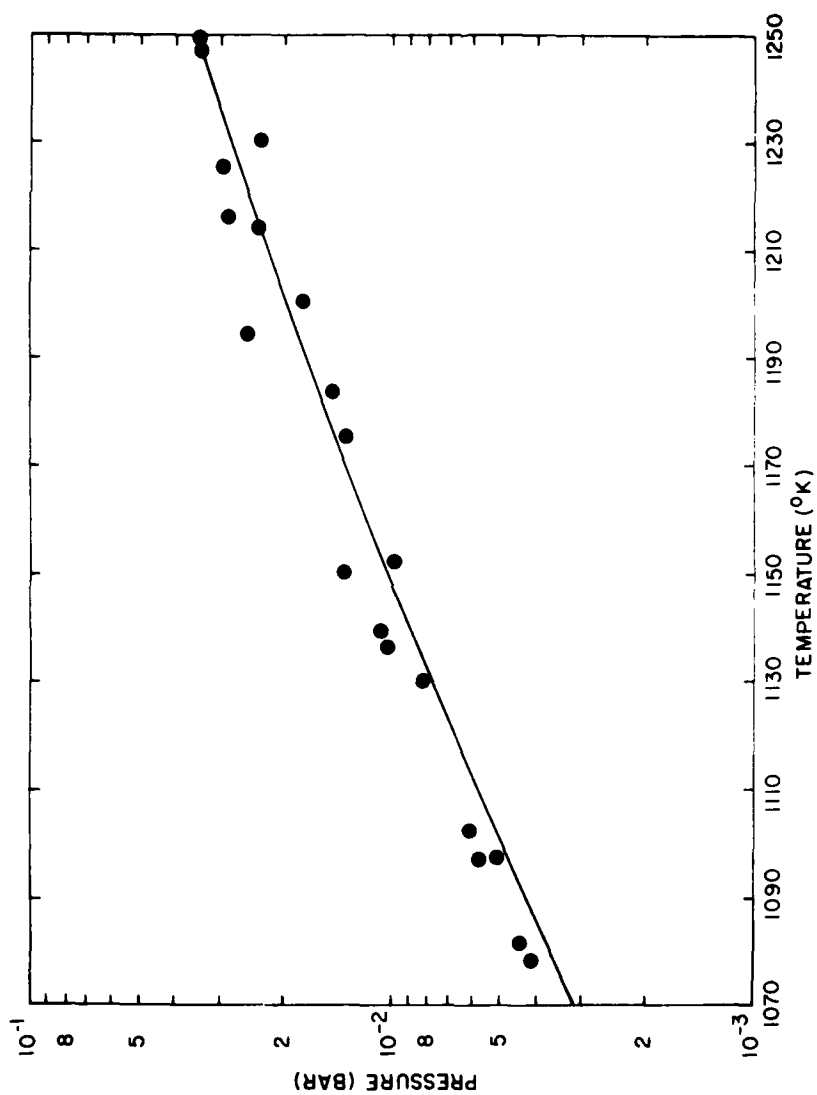


Figure 21 Wick-Type Combustor Total Pressure Results

5.5 Oxidizer Utilization Efficiency Results

Oxidizer utilization efficiency tests were conducted following the procedure described in Appendix E. The injector was submerged at depths of 5.0 to 7.6 cm. and had oxidizer and shroud argon flows of approximately 2.5 and 0.63 kg/hr, respectively. The tests were conducted in a vented pot-type combustor. The results indicated the presence of small amounts of unreacted oxidizer in the argon flow leaving the combustor during the initial start-up transient when the bath temperature was in the range of 810 to 870°K. No unreacted oxidizer was detected during subsequent operation. The oxidizer utilization efficiency during the start-up transient was greater than 99.5%. The results confirmed that the oxidizer utilization efficiency is 100% during normal operating conditions of the experimental apparatus.

5.6 Thermal Performance Results

5.6.1 Energy Release. The thermal performance data obtained during tests PPC-9 and PPC-10 are plotted in Figure 22 as heat exchanger load versus oxidizer flow. The average net parasitic heat loss from the apparatus is given by the negative intercept on the heat exchanger load axis, and includes the sum of all losses from the system and the electrical input to the system through the sump guard heaters. The value of 2.98 kW was determined by a least squares linear fit to the data and therefore is an average value for the entire group of data. The slope of the least squares fit yields an energy release rate of 4.99 kW-hr/kg of oxidizer at a bath temperature of $1197 \pm 3^\circ\text{K}$, a fuel inlet temperature of 533°K , and an

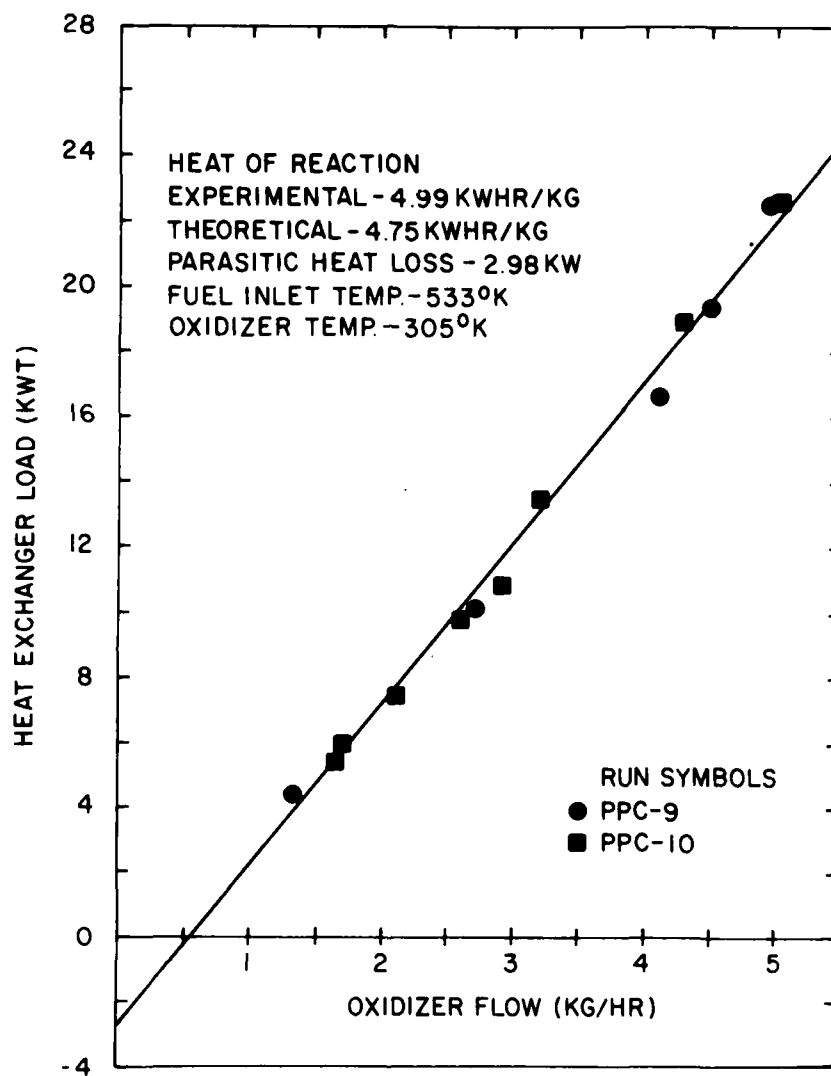


Figure 22 Performance Results

oxidizer temperature of 305°K. The theoretical values for these conditions are 4.71 kW-hr/kg and 4.79 kW-hr/kg for the high and low lithium sulfide heats of fusion cases, respectively. The experimental value is 5.9% higher than the high heat of fusion value and 4.2% higher than the low heat of fusion value. The small error largely results from the assumption that the parasitic heat loss remained constant with load. In fact, the parasitic heat loss decreased with increased load. The value of the parasitic heat loss at each load condition could not be determined, and the use of an average value caused the slope of the curve to be incorrectly too high.

The difference between the theoretical energy release rates is caused by the enthalpy of liquid lithium sulfide being approximately 10% higher for the high heat of fusion case than for the low heat of fusion case. It is impossible to determine from the thermal performance data which is the correct value for the heat of fusion of lithium sulfide, as errors introduced by the estimated heat capacity data are expected to be approximately of the same order of magnitude as the changes caused by the differences in the heats of fusion. Additionally, the uncertainty in the experimental value dominates the small difference between the two theoretical values. The contribution to the product-rich liquid enthalpy from the excess enthalpy of mixing is on the order of 0.1% and therefore effects from nonideal mixing are small from the energy release standpoint. The recommended value for the energy release rate at the given operating conditions is the average of the two results or 4.75 kW-hr/kg of oxidizer.

5.6.2 Energy Utilization. The energy utilization efficiency of the air-cooled combustor is considered in Figure 23. The figure presents an energy flow diagram for the combustor under conditions where the power to the load is 25 kW and the bath temperature, fuel inlet temperature and oxidizer temperature are 1197, 533, and 305°K, respectively. The losses from the system associated with parasitic heat loss and product enthalpy were found to equal 3.7 and 5.57 kW, respectively. The parasitic heat loss was determined by extrapolating the data at the 22.5 kW load condition and using the average theoretical energy release rate of 4.75 kW-hr/kg to obtain the net parasitic heat loss. The power input from the electrical guard heaters of 1.9 kW was estimated from knowledge of the heater power outputs and the controller cycle periods. The electrical power was added to the net parasitic heat loss to obtain the total parasitic heat loss from the system. It is noted that the net parasitic heat loss from the system at the extrapolated 25 kW power level was approximately 40% lower than the average value for all actual load conditions. The product enthalpy, electrical energy input to the fuel, and the standard heat of reaction were computed from the theoretical model using the average energy release rate.

In an actual submersible application the product enthalpy would not be lost from the system, but could be used as a source for vehicle heating and as energy needed to melt the fuel. Additionally, the electrical guard heaters could be eliminated by designing the sump regions with additional emphasis on the thermal management problems associated with these regions.

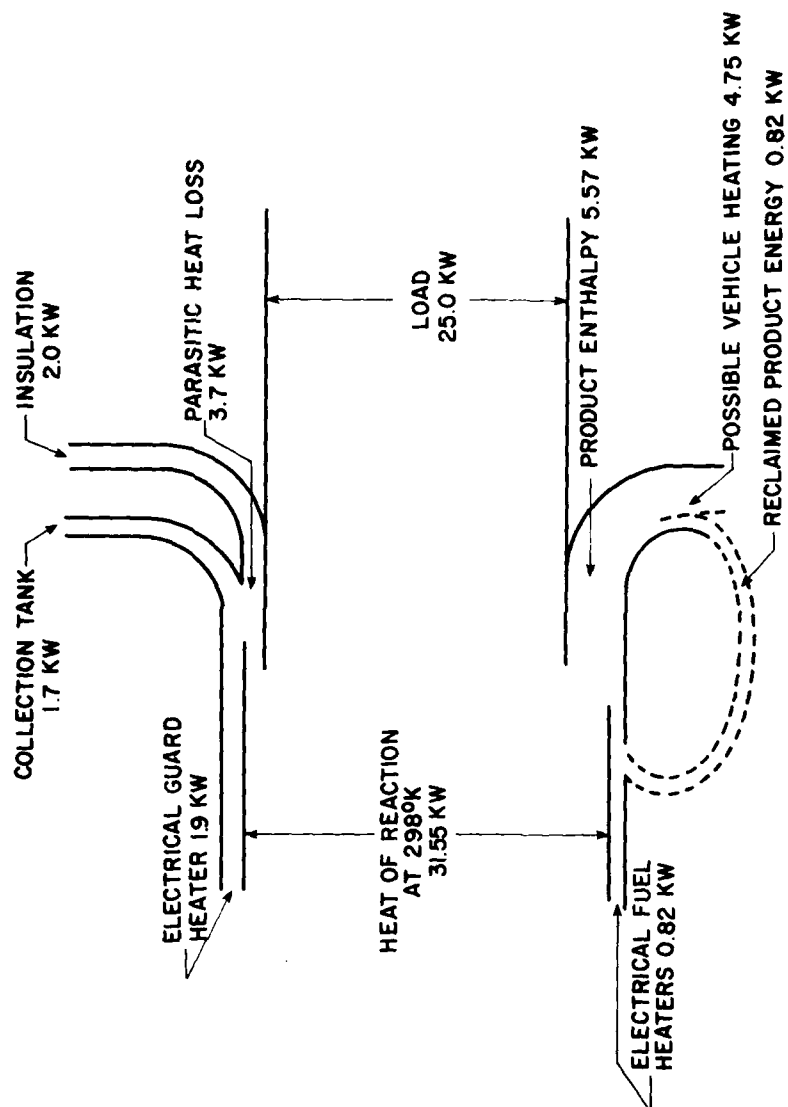


Figure 23 Energy Flow Diagram for Apparatus

As illustrated in Figure 23, approximately 79.2% of the standard heat of reaction at 298°K was transferred to the load at a bath temperature of 1197°K. The effects of bath temperature on system performance are discussed in the following section.

5.6.3 Bath Temperature Effects on System Performance. Figure 24 presents fuel utilization efficiency, thermal efficiency, bath liquid density ratio, and total mixture pressure as a function of temperature. The results are the average of the values computed from the two cases employing different values for the heat of fusion of lithium sulfide examined in the theoretical model. The thermal efficiency curve was computed assuming no parasitic heat loss from the system and with fuel and oxidizer inlet temperatures of 533 and 305°K, respectively. Additionally, the effects of fuel carryover in the argon exhaust from the reaction chamber and the energy loss resulting from the flow were not included.

The bath liquid density ratio given by the ratio of the density of the product-rich liquid to the density of the fuel-rich liquid decreases with increasing bath temperature from a value of 3.52 at 1110°K to a value of 1.00 at the computed consolute temperature of 1638°K. At temperatures above the consolute temperature the product-rich and fuel-rich phases are miscible and removal of the reaction products from the reaction chamber is not possible. The decrease in the liquid density ratio with increasing temperature indicates that the combustor trap geometry needed to maintain the fuel-rich and product-rich liquid levels at specified values is temperature dependent. For the trap design employed in the combustor

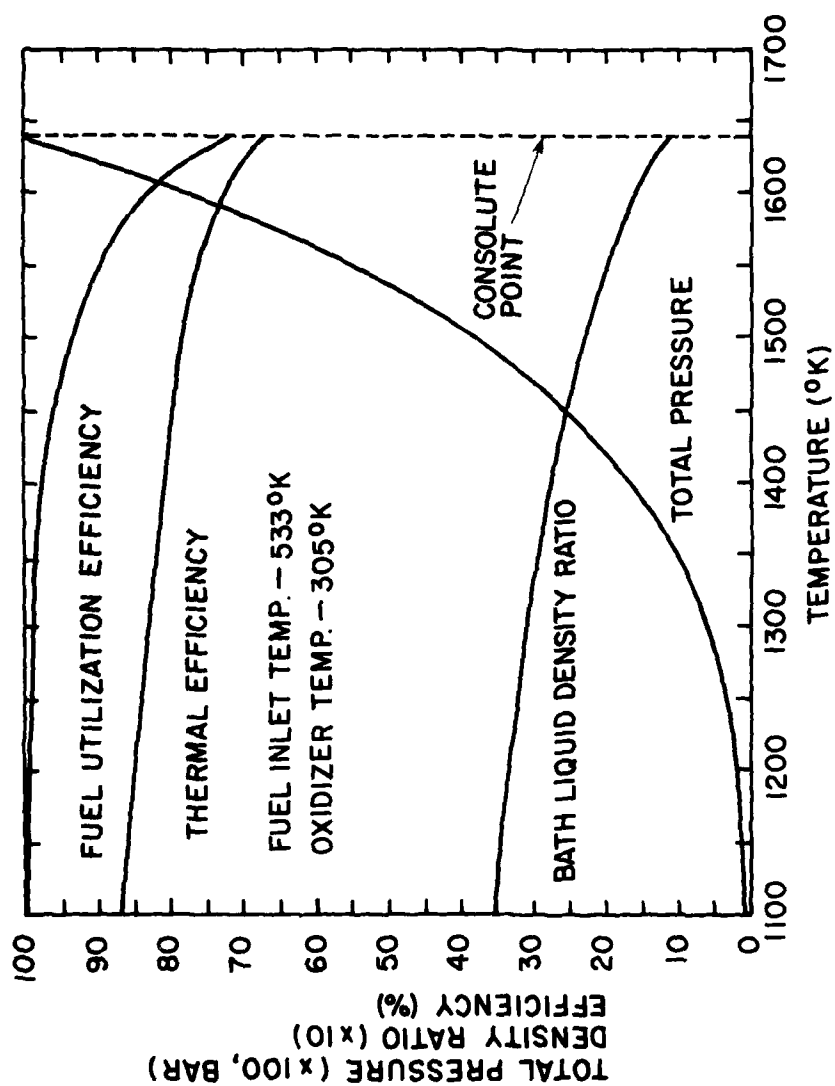


Figure 24 Effects of Bath Temperature on System Performance

used in the present study, the inner trap tube would have to be lengthened for operation at a higher bath temperature.

The total vapor pressure of the mixture was found to increase significantly with increasing bath temperature. The total pressure increases from 0.00565 bar at 1110°K to 0.98 bar at 1638°K. The vapor pressure of the mixture becomes the internal pressure of the reaction chamber when an unvented configuration is used. In this case, the combustor trap system must be designed with the pressure forces taken into consideration. For a vented combustor such as the one used in the present study, the increased vapor pressure represents an increased mass flow of fuel and product species from the combustor for a given argon flow.

The thermal efficiency is defined as the ratio of the energy released to the load to the standard heat of reaction at 298°K. The thermal efficiency decreases from a value of 86.4% at a bath temperature of 1110°K to a value of 67.0% at a bath temperature of 1638°K. The decrease is caused by the products being exhausted at a higher temperature and therefore with a higher enthalpy.

The fuel utilization efficiency is defined as the ratio of the rate of fuel consumption by the chemical reaction to the total fuel flow rate to the reaction chamber. Fuel utilization efficiencies of 99.8% and 73.0% are achieved at bath temperatures of 1110 and 1638°K, respectively. The decrease is caused by the increased solubility of the fuel in the products exhausted from the reaction chamber.

CHAPTER VI

SUMMARY AND CONCLUSIONS

6.1 Summary

The overall objective of the present study was to investigate analytically and experimentally the characteristics of a steadily operating liquid metal thermal energy source employing the lithium-sulfur hexafluoride reactant combination. The specific objectives of the study were as follows:

1. Experimentally measure bath liquid densities, bath liquid compositions, and thermal performance for temperatures typical of metal combustor operation.
2. Develop a thermodynamic model for the bath liquids and compare the model predictions to the measurements.
3. Examine continuous operation of a complete steady combustor system with varying thermal load requirements for extended periods of time.

A steady metal combustor apparatus which permitted the necessary measurements to be made was designed and fabricated. Steady-state conditions were established by continuously supplying fuel and oxidizer to the reaction chamber while continuously removing the reaction products through a trap arrangement in the bottom of the chamber. The oxidizer was injected into the molten bath through a coaxial injector, and fuel was supplied with an argon lift pump. The apparatus was operated in the temperature range of 1110 to 1255°K with power outputs ranging from 0.0 to 25.2 kW.

Procedures were developed to obtain bath liquid samples from the reaction chamber, and to analyze the samples using wet-test chemical analysis methods. Procedures were also developed for obtaining bath liquid density data. Bath liquid solubility data were obtained in the temperature range of 1116 to 1244°K, and bath liquid density data were obtained in the temperature range of 1144 to 1280°K.

Thermal performance data were generated at a bath temperature of $1197 \pm 3^\circ\text{K}$ over a range of load conditions. The data yielded an energy release rate of 4.99 kW-hr/kg of oxidizer which is in good agreement with the theoretical value obtained from the thermodynamic model of 4.75 kW-hr/kg.

System operation was demonstrated for extended periods with the longest test being ten hours in duration. The capability of the system to operate under variable load range, idling and restart conditions was also demonstrated. No corrosion problems with the type 316 stainless steel components were observed.

A thermodynamic model for the reaction chamber contents was developed using the van Laar expression for the excess Gibbs free energy of mixing in the liquid phase and an ideal solution assumption for the gas phase. The model permitted the calculation of liquid phase solubilities, liquid phase densities, gas phase partial pressures, and thermal performance.

Experimentally determined bath liquid solubility data, bath liquid density data, and thermal performance were compared to the theoretical predictions. It was found that the model adequately predicted the thermodynamic characteristics of the system.

6.2 Conclusions

The major conclusions of the study are as follows:

1. The thermodynamic model for the ternary immiscible liquid mixture composed of lithium, lithium fluoride, and lithium sulfide examined in this study predicted the solubilities of the various components within an accuracy of 5-50% indicating the van Laar expression for the excess Gibbs free energy of mixing used in the model adequately represents the mixing characteristics of the system. Additionally, the experimentally measured liquid densities, mixture vapor pressures and thermal performance agreed within 5% of the thermodynamic model predictions.
2. A steadily operating metal combustor was operated for periods on the order of ten hours under conditions of continuous fuel addition and product outflow, variable load range, idling and restart. These operating periods were not limited by the combustor, and longer periods of operation appear to be feasible.
3. The thermal efficiency of the system decreases with temperature from a value of 86.4% at a bath temperature of 1110°K to a value of 84.0% at a bath temperature of 1250°K.
4. Fuel utilization efficiency decreases with increasing bath temperature from a value of 99.8% at a bath temperature of 1110°K to a value of 99.2% at a bath temperature of 1250°K.

5. Visual inspection of the type 316 stainless steel components used in the experimental apparatus revealed no corrosion problems, indicating that this material is suitable for combustor fabrication. Sample contamination was found during the chemical analysis of fuel-rich liquid samples extracted with type 316 stainless steel sample cups which was not found in samples extracted with nickel 200 alloy cups. The contamination was believed to be caused by the products of surface corrosion of the stainless steel by lithium sulfide since similar contamination was found during lithium-lithium sulfide solubility tests at temperatures above 1100°K. These findings suggest low levels of corrosion that are not apparent during visual inspection of components following test periods in the range of the current investigation, but which could be a factor during longer periods of operation.

6.3 Recommendations for Further Study

It is desirable to have additional solubility data for the lithium-lithium sulfide and lithium fluoride-lithium sulfide binary systems. Additional data over a broader temperature-concentration range would permit more confident evaluation of the empirical parameters associated with these binary pairs. Of particular importance is data in the lithium sulfide-rich region of either phase diagram since such data could be used to infer the heat of fusion of lithium sulfide.

The thermodynamic model developed in this study can be applied to the analysis of other combustor concepts. Several new combustor designs have been proposed which need to be examined both analytically and experimentally [46].

BIBLIOGRAPHY

1. Pauliukonis, R. S., "Fuel System Comprising Sulfur Hexafluoride and Lithium Containing Fuel," United States Patent 3,325,318, June 13, 1967.
2. van der Sluijs, W. L. N., "A Lithium/Sodium/Sulphurhexafluoride Heat Source in Combination with a Stirling Engine as a Propulsion System for Small Submersibles," Proceedings of Tenth Intersociety Energy Conversion Engineering Conference, p. 1031-1037, 1975.
3. Percival, W. H., "Underwater Propulsion System," United States Patent 3,353,349, November 21, 1967.
4. Uhlemann, H., Spigt, C. L., and Hermans, M. L., "The Combination of a Stirling Engine with a Remotely Placed Heat Source," Proceedings of Ninth Intersociety Energy Conversion Engineering Conference, p. 620-629, 1974.
5. Biermann, U. K. P., "The Lithium/Sulfurhexafluoride Heat Source in Combination with a Stirling Engine as an Environmental Independent Underwater Propulsion System," Proceedings of Tenth Intersociety Energy Conversion Engineering Conference, p. 1023-1030, 1975.
6. Mattavi, J. N., Heffner, F. E., and Miklos, A. A., "The Stirling Engine for Underwater Vehicle Applications," Society of Automotive Engineers, National Powerplant Meeting, Paper 690731, October 27-29, 1969.
7. Faeth, G. M., Kuo, K. K., and Olson, D. R., "A Study of a Liquid Metal Thermal Energy Source," Final Report under Contract No. N00600-73-C-0113, Advanced Research Projects Agency, ARPA Order No. 2150, Program Code No. 2N10, Mechanical Engineering Department, The Pennsylvania State University, 155 p., August, 1973.
8. Blakeslee, T., Groff, E., Faeth, G. M., and Olson, D. R., "A Study of a Liquid Metal Thermal Energy Source," Annual Report under Contract No. N00600-74-C-0033, Advanced Research Projects Agency, ARPA Order No. 2150, Program Code No. 2N10, Mechanical Engineering Department, The Pennsylvania State University, 112 p., September, 1974.
9. Faeth, G. M., "Steady Heat Generating Reactor," United States Patent, 3,838,658, October 1, 1974.
10. Stull, D. R. and Prophet, H., Project Directors, JANAF Thermochemical Tables, NSRDS-NBS 37, U. S. Government Printing Office, Washington, D. C., June, 1971.

11. Janz, G. J., et al., Molten Salts: Volume I, Electrical Conductance, Density, and Viscosity Data, NSRDS-NBS 15, U. S. Government Printing Office, Washington, D. C., October, 1968.
12. Davison, H. W., "Compilation of Thermophysical Properties of Liquid Lithium," NASA TN D-4650, 1968.
13. Morris, D. F. C., "The Lattice Energy and Heat of Formation of Lithium Monosulfide," Journal Physical Chemistry of Solids, Vol. 5, p. 264-267, 1958.
14. Juza, R., and Uphoff, W., "Zur Kenntnis des Lithiumsulfids," Zeitschrift für anorganische und allgemeine Chemie, Band 287, Heft 3, p. 113-168, October 1956.
15. Cunningham, P. T., Johnson, S. A., and Cairns, E. J., "Phase Equilibria in Lithium-Chalcogen Systems," Journal of the Electrochemical Society, Vol. 119, No. 11, p. 1448-1450, 1972.
16. Mott, W. R., "Relative Volatilities of Refractory Materials," Transactions of the Electrochemical Society, Vol. 34, p. 255-295, 1918.
17. Mourlot, M. A., "Recherches Sur Les Sulfures Metalliques," Annales De Chemie Et De Physique, Serie 7, Vol. 17, p. 510-576, 1899.
18. Zintl, E., Harder, A., and Dauth, B., "Gitterstruktur Der Oxyde, Sulfide, Selenide Und Telluride Des Lithiums Natriums Und Kalium," Zeitschrift für Elektrochemie und Angewandte Physikalische Chemie, Band 40, Nr. 8, p. 588-593, 1934.
19. Beck, G., "Energie-und Raumänderung bei chemischen Reaktionen," Zeitschrift für anorganische und allgemeine Chemie, Band 233, p. 151-160, 1937.
20. Dworkin, A. S., Bronstein, H. R., and Bredig, M. A., "Miscibility of Metals with Salts. VI. Lithium-Lithium Halide Systems," Journal of Physical Chemistry, Vol. 66, p. 572-573, 1962.
21. Faeth, G. M., Personal Correspondence, 1973.
22. Avery, J. F., "Combustion of a Submerged Turbulent Oxidizer Jet in a Liquid Metal," Ph.D. Thesis, The Pennsylvania State University, University Park, Pennsylvania, 1974.
23. Nakanishi, K., "Thermodynamic Studies of Phase Equilibria in Molten Salt Systems," Industrial Engineering Chemistry, Fundamentals, Vol. 9, No. 3, p. 449-453, 1970.
24. Mattavi, J. N., "Bubble Reaction Characteristics," Ph.D. Thesis, The Pennsylvania State University, University Park, Pennsylvania, 1969.

25. Little, T. E., "Reactivity of Nitrogen, Oxygen, and Halogenated Gases with Molten Lithium Metal," Ph.D. Thesis, The Pennsylvania State University, University Park, Pennsylvania, 1973.
26. Avery, J. F. and Faeth, G. M., "Combustion of a Submerged Gaseous Oxidizer Jet in a Liquid Metal," Fifteenth Symposium (International) on Combustion, p. 501-512, The Combustion Institute, Pittsburgh, Pennsylvania, 1974.
27. Wohl, K., "Thermodynamic Evaluation of Binary and Ternary Liquid Systems," Transactions of the American Institute of Chemical Engineers, Vol. 42, p. 215-249, 1946.
28. Wilson, G. M., "Vapor-Liquid Equilibrium. XI. A New Expression for the Excess Free Energy of Mixing," Journal of the American Chemical Society, Vol. 86, p. 127-130, 1964.
29. Orye, R. V. and Prausnitz, J. M., "Multicomponent Equilibria with the Wilson Equation," Industrial and Engineering Chemistry, Vol. 57, p. 18-26, 1965.
30. Hiranuma, M., "A New Expression Similar to the Three-Parameter Wilson Equation," Industrial Engineering Chemistry, Fundamentals, Vol. 13, No. 3, 1974.
31. Nagata, I. and Yamada, T., "Correlation and Prediction of Excess Thermodynamic Functions of Strongly Nonideal Liquid Mixtures," Industrial Engineering Chemistry, Process Design and Development, Vol. 13, No. 1, 1974.
32. Renon, H. and Prausnitz, J. M., "Local Compositions in Thermodynamic Excess Functions for Liquid Mixtures," American Institute of Chemical Engineering Journal, Vol. 14, p. 135-144, 1968.
33. Marina, J. M. and Tassios, D. O., "Effective Local Compositions in Phase Equilibrium Correlations," Industrial Engineering Chemistry, Process Design and Development, Vol. 12, No. 1, p. 67-71, 1973.
34. Marina, J. M. and Tassios, D. P., "Prediction of Ternary Liquid-Liquid Equilibrium from Binary Data," Industrial Engineering Chemistry, Process Design and Development, Vol. 12, No. 3, p. 271-274, 1973.
35. Bruin, S., "Activity Coefficient Relations in Miscible and Partially Miscible Multicomponent Systems," Industrial Engineering Chemistry, Fundamentals, Vol. 9, No. 3, p. 305-314, 1970.

36. Pitzer, K. S., "Solubility and the Nature of Bonding in Fused Alkali Halide-Metal Systems," Journal of the American Chemical Society, Vol. 84, No. 11, p. 2025-2027, 1962.
37. Lumsden, J., Thermodynamics of Molten Salt Mixtures, Academic Press, New York, New York, p. 293-298, 1966.
38. Lewis, G. H. and Randall, M., Thermodynamics, Second Edition, Revised by K. S. Pitzer and L. Brewer, McGraw-Hill Book Company, New York, New York, 1961.
39. Hildebrand, J. H., Prausnitz, J. M., and Scott, R. L., Regular and Related Solutions, Van Nostrand Reinhold Company, New York, New York, 1970.
40. Berkowitz, J. and Chupka, W. A., "Composition of Vapors in Equilibrium with Salts at High Temperatures," Annals of the New York Academy of Sciences, Vol. 79, p. 1073-1078, 1960.
41. Thormeier, K., "Solubility of the Noble Gases in Liquid Sodium," Nuclear Engineering and Design, Vol. 14, p. 69-82, 1970.
42. Slotnick, H., Kapelner, S. M., and Cleary, R. E., "The Solubility of Helium in Lithium and Potassium," Pratt and Whitney Aircraft Company Report PWAC-380, February 24, 1965.
43. Blander, M., Editor, Molten Salt Chemistry, p. 231, John Wiley and Sons, New York, New York, 1964.
44. Moffat, R. J., "Gas Temperature Measurement," Temperature-Its Measurement and Control in Science and Industry, Vol. 3, Part 2, p. 553-571, Reinhold Publishing Corporation, New York, New York, 1962.
45. Obert, E. F. and Gaggiloi, R. A., Thermodynamics, Second Edition, McGraw-Hill Book Company, New York, New York, 1963.
46. Blakeslee, T. III, Groff, E. G., Faeth, G. M. and Olson, D. R., "A Study of a Liquid Metal Thermal Energy Source," Quarterly Technical Report, December 1, 1976 to February 29, 1976, under Contract No. N00600-74-C-0033, Advanced Research Projects Agency, ARPA Order No. 2150, Program Code No. 2N10, Mechanical Engineering Department, The Pennsylvania State University, 38 p., March 1976.
47. Steunenber, R. K., Letter from Argonne National Laboratory to this author dated May 22, 1975.
48. Lange, N. A., Editor, Handbook of Chemistry, 11th Edition, Handbood Publishers, Sandusky, Ohio, 1973.

49. Bichowsky, F. R. and Rossini, F. D., The Thermochemistry of the Chemical Substances, Reinhold Publishing Company, New York, New York, 1936.
50. Handbook of Chemistry and Physics, 52nd Edition, The Chemical Rubber Company, Cleveland, Ohio, 1971.
51. Gray, D. E., Editor, American Institute of Physics Handbook, 3rd Edition, McGraw-Hill Book Company, New York, New York, 1972.
52. Davidson, N., Statistical Thermodynamics, McGraw-Hill Book Company, New York, New York, 1962.
53. Luke, C. L., "Determination of Sulfur in Nickel by the Evolution Method," Analytical Chemistry, Vol. 29, No. 8, p. 1227-1228, August, 1957.
54. Willard, H. H. and Winter, D. B., "Volumetric Method for Determination of Fluorine," Industrial and Engineering Chemistry, Analytical Edition, Vol. 5, No. 1, p. 7-10, January, 1933.
55. Rogers, L. B. and Calley, E. R., "A New Selective Reagent for Lithium," Industrial and Engineering Chemistry, Analytical Edition, Vol. 15, No. 3, p. 209-211, March, 1943.

APPENDIX A

COMPUTER PROGRAM AND NEWTON-RAPHSON METHOD USED TO SOLVE THE THERMODYNAMIC MODEL EQUATIONS

The set of thermodynamic model equations are not easily solved because of the nonlinear form of Equations (2.43) after substitution of Equations (2.19) for the component activities. The resulting equations were simplified somewhat by taking the natural logarithm of both sides.

The Newton-Raphson method was used to obtain the solution to the set of nonlinear equations. A change of variables was necessitated because the existence of the natural logarithm of the mole fractions resulted in procedure failure if the computer iterated to a negative mole fraction during the course of the search. To eliminate the problem logarithmic variables were employed as follows:

$$z_i = \ln x_i \quad (A.1)$$

$$w_i = \ln y_i \quad (A.2)$$

where x_i and y_i are the mole fractions of the various components in the two immiscible phases.

In terms of the variables defined by Equations (A.1) and (A.2), Equations (2.43), (2.44), (2.45), and (2.49) become

$$\begin{aligned}
 RTz_1 + \frac{B_2 A_{12} e^{z_2} (B_2 e^{z_2+e^{z_3}}) - B_3 A_{23} e^{z_2 z_3} + A_{13} e^{z_3} (B_2 e^{z_2+e^{z_3}})}{(B_3 e^{z_1+B_2 e^{z_2+e^{z_3}}})^2} \\
 - RTw_1 - \frac{B_2 A_{12} e^{w_2} (B_2 e^{w_2+e^{w_3}}) - B_3 A_{23} e^{w_2 w_3} + A_{13} e^{w_3} (B_2 e^{w_2+e^{w_3}})}{(B_3 e^{w_1+B_2 e^{w_2+e^{w_3}}})^2} = 0
 \end{aligned}
 \tag{A.3}$$

$$\begin{aligned}
 RTz_2 + \frac{B_2 A_{12} e^{z_1} (B_3 e^{z_1+e^{z_3}}) - B_2 A_{13} e^{z_1 z_3} + A_{23} e^{z_3} (B_3 e^{z_1+e^{z_3}})}{(B_3 e^{z_1+B_2 e^{z_2+e^{z_3}}})^2} \\
 - RTw_2 - \frac{B_2 A_{12} e^{w_1} (B_3 e^{w_1+e^{w_3}}) - B_2 A_{13} e^{w_1 w_3} + A_{23} e^{w_3} (B_3 e^{w_1+e^{w_3}})}{(B_3 e^{w_1+B_2 e^{w_2+e^{w_3}}})^2} = 0
 \end{aligned}
 \tag{A.4}$$

$$\begin{aligned}
 RTz_3 + \frac{A_{23} e^{w_1} (B_3 e^{z_1+B_2 e^{z_2}}) - B_2 A_{12} e^{z_1 z_2} + A_{13} e^{z_1} (B_3 e^{z_1+B_2 e^{z_2}})}{(B_3 e^{z_1+B_2 e^{z_2+e^{z_3}}})^2} \\
 - RTw_3 - \frac{A_{23} e^{w_1} (B_3 e^{w_1+B_2 e^{w_2}}) - B_2 A_{12} e^{w_1 w_2} + A_{13} e^{w_1} (B_3 e^{w_1+B_2 e^{w_2}})}{(B_3 e^{w_1+B_2 e^{w_2+e^{w_3}}})^2} = 0
 \end{aligned}
 \tag{A.5}$$

$$e^{z_1} + e^{z_2} + e^{z_3} = 1 \tag{A.6}$$

$$e^{w_1} + e^{w_2} + e^{w_3} = 1 \tag{A.7}$$

$$e^{w_2} - 6e^{w_3} = 1 \tag{A.8}$$

Equations (A.3) to (A.8) were linearized by choosing estimates of the variables, z_{i0} and w_{i0} , and writing

$$z_i = z_{i0} + z_i' \quad (\text{A.9})$$

$$w_i = w_{i0} + w_i' \quad (\text{A.10})$$

where z_i' and w_i' are small correction terms to the original estimate.

The linearized equations can be obtained either by direct substitution of Equations (A.9) and (A.10) into Equations (A.3) to (A.8) and simplification, or by expanding each equation in a Taylor series about the initial estimates. Using the Taylor series method, the equations can be expressed as functions of the six variables as follows

$$f(z_i, w_i) = C \quad (\text{A.11})$$

where C represents a constant characteristic of a given equation. If higher order terms are neglected, the equations can be expressed as

$$\begin{aligned} f(z_i, w_i) = f(z_{i0}, w_{i0}) + \sum_{i=1}^3 z_i' \frac{\partial f}{\partial z_i} (z_{i0}, w_{i0}) \\ + \sum_{i=1}^3 w_i' \frac{\partial f}{\partial w_i} (z_{i0}, w_{i0}) = 0 \end{aligned} \quad (\text{A.12})$$

The resulting expressions are arranged in matrix form as follows

$$[D_{ij}] \begin{bmatrix} z_i' \\ w_i' \end{bmatrix} = G_i \quad (\text{A.13})$$

The computer program used to solve Equations (A.13) is presented below with the matrix coefficients D_{ij} and G_i being denoted by $A(i,j)$

and $R(1)$ in the program. The equations were solved for z_1' and w_1' for a given iteration using the Gaussian elimination method. The original estimates were updated following each iteration by adding z_1' and w_1' to z_{10} and w_{10} , respectively, and the method was repeated until all z_1' and w_1' were reduced to within desired tolerances. The mole fractions of the two phases are then given by

$$x_i = \exp(z_{i0}) \quad (A.14)$$

$$y_i = \exp(w_{i0}) \quad (A.15)$$

The computer program is listed as shown on the following pages.


```

C      IMPLICIT REAL*8(A-H,O-Z)
C      PREDICTION OF TERNARY MIXTURE IMMISCIBILITY
C      VAN LAAR MODEL UTILIZED
C      STOICHIOMETRIC REQUIREMENT INCLUDED
      DIMENSION Z(12),B(12),C(12),D(12),E(12),F(12),G(12),DHF(12),H(12),
      1A(6,6),R(6),CP(12),S(12),HREF(12),FREF(12),FENER(12)
      DIMENSION WKAREA(8)
      RG=1.98726
C      READ IN PROPERTY DATA COEFFICIENTS FROM JANAF
      READ(5,1)Z
      READ(5,1)B
      READ(5,1)C
      READ(5,1)D
      READ(5,1)E
      READ(5,1)F
      READ(5,1)G
      READ(5,1)DHF
      1 FORMAT(4E15.8)
      RG=1.98726
C      COMPONENTS 1**LIF(S), 2**LIF(L), 3**LIF(G), 4**LI2F2(G), 5**LI3F3(G),
C      6**LI(S), 7**LI(L), 8**LI(G), 9**LI2(G), 10** LI2S(S), 11**LI2S(L),
C      12**LI2S(G)
C      PROPERTIES OF COMPONENTS 1 THRU 9 FROM JANAF TABLES
C      PROPERTIES OF COMPONENTS 11 AND 12 ESTIMATED FROM NA2S IN JANAF
C      PROPERTIES OF COMPONENT 12 CALCULATED FROM STATISTICAL THERMODYNAMIC
C      DO LOOP PRODUCING HEAT OF FUSION CHANGE
      DO 911 JDHF=1,2
C      ADJUST LI2S LIQUID AND GAS ENTHALPY FOR HEAT OF FUSION CHANGE
      IF(JDHF.EQ.1)DHF(11)=-107.8
      IF(JDHF.EQ.1)DHF(12)=-42.532
      IF(JDHF.EQ.1)F(11)=-115.4155
      IF(JDHF.EQ.2)DHF(11)=-117.9
      IF(JDHF.EQ.2)DHF(12)=-52.632
      IF(JDHF.EQ.2)F(11)=-125.5155
      T=1110.0

```

```

C      INITIAL GUESSES OF THE LOGS OF THE MOLE FRACTIONS
X10=-0.02655
X20=-3.7636
X30=-5.9522
Y10=-6.1423
Y20=-0.15676
Y30=-1.9486
C      DO LOOP PRODUCING THE TEMPERATURE VARIATION
DO 999 JKL=1,18
C      DO LOOP PRODUCING PROPERTIES OF FIRST ELEVEN COMPONENTS
DO 942 I=1,11
  TR=T/1000.0
  CP(I)=Z(I)+B(I)*TR+C(I)*TR**2+D(I)*TR**3.+E(I)/TR**2
  S(I)=Z(I)*DLOG(TR)+B(I)*TR+(C(I)*TR**2)/2.0+(D(I)*TR**3.)/3.0-E(I)
  1/(2.0*TR**2)+G(I)
  H(I)=Z(I)*TR+B(I)*TR**2/2.0+C(I)*TR**3./3.0+D(I)*TR**4./4.0-E(I)/T
  1R+FI)
  HREF(I)=H(I)-DHF(I)
  FREF(I)=S(I)-HREF(I)/TR
  H(I)=1000.0*H(I)
  HREF(I)=1000.0*HREF(I)
942 CONTINUE
  FENER(1)=-145996.9287-T*FREF(1)
  FENER(2)=-143083.2800-T*FREF(2)
  FENER(3)=-80690.9349-T*FREF(3)
  FENER(4)=-219506.3114-T*FREF(4)
  FENER(5)=-361019.9969-T*FREF(5)
  FENER(6)=-2.6532-T*FREF(6)
  FENER(7)=565.6305-T*FREF(7)
  FENER(8)=38398.3928-T*FREF(8)
  FENER(9)=50345.2354-T*FREF(9)
  FENER(10)=-117702.9008-T*FREF(10)
  FENER(11)=-116189.1038-T*FREF(11)
C      THERMODYNAMIC PROPERTIES OF LINEAR LI2S GAS
  V1=556.0

```

```

V2=102.0
V3=722.0
RAD=1.926
WM=45.944
ERT=2.30442D-39*RAD**2
BP=2.7989D-39/ERT
D2=2.0
SIG=2.0
STR=1.5*DLOG(WM)+2.5*DLOG(T)-1.165
HTR=2.5*T
FTR=1.5*DLOG(WM)+2.5*DLOG(T)-3.665
CPT=2.5
U1=1.4387*V1/T
U2=1.4387*V2/T
U3=1.4387*V3/T
P=DEXP(U1)-1.0
Q=DEXP(U2)-1.0
RQ=DEXP(U3)-1.0
PP=1.0-DEXP(-U1)
QQ=1.0-DEXP(-U2)
RR=1.0-DEXP(-U3)
SVIB=U1/P+D2*U2/Q+U3/RQ-DLOG(PP*RR*QQ**D2)
HVIB=T*(U1/P+D2*U2/Q+U3/RQ)
FVIB=-DLOG(PP*RR*QQ**D2)
CPVIB=U1**2*DEXP(U1)/P**2+D2*U2**2*DEXP(U2)/Q**2+U3**2*DEXP(U3)/RQ
I**2
RC=1.4388*BP/T
SROT=1.0-DLOG(RC)-DLOG(SIG)-RC**2/90.0
HROT=T*(1.0-RC/3.0-RC**2/45.0)
FROT=-DLOG(RC)-DLOG(SIG)+RC/3.0+RC**2/90.0
CPROT=1.0+RC**2/45.0
STOT=STR+SVIB+SROT
HTOT=HTR+HVIB+HROT
FTOT=FTR+FVIB+FROT
CPTOT=CPT+CPVIB+CPROT

```

```

S(12)=RG*STOT
+REF(12)=RG*HTOT-3170.726
=REF(12)=RG*FTOT+3170.726/T
CP(12)=RG*CPTOT
H(12)=HREF(12)+1000.0*DHF(12)
FENER(12)=-60529.9986-T*FREF(12)
BINARY VAN LAAR CONSTANTS
A12=29050.0-13.70*T
B1=2.58-8.13D-04*T
A23=0.0
IF(JDHF.EQ.1)B3=1.36
IF(JDHF.EQ.1)A13=12700.0-0.0957*T
IF(JDHF.EQ.2)B3=1.24
IF(JDHF.EQ.2)A13=21100.0-7.11*T
B2=B3/B1
WRITE(6,111)T,B1,A12,B2,A23,B3,A13
111 FORMAT(7F15.5)
ITER=0
99 ITER=ITER+1
C  SET UP OF MATRIX COEFFICIENTS
  ALPHA=B3*DEXP(X10)+B2*DEXP(X20)+DEXP(X30)
  BETA=B3*DEXP(Y10)+B2*DEXP(Y20)+DEXP(Y30)
  SRATIO=6.0
C  MATRIX COEFFICIENTS
  A(1,1)=RG*T+(-2.*B2*B3*A12*DEXP(X20+X10)*(B2*DEXP(X20)+DEXP(X30))+
12.0*B3**2*A23*DEXP(X20+X30+X10)-2.0*B3*A13*DEXP(X10+X30)*(B2*DEXP(
2X20)+DEXP(X30)))/ALPHA**3.
  A(1,2)=(2.0*B2**2*A12*DEXP(2.*X20)+B2*A12*DEXP(X20+X30)-B3*A23*DEX
1P(X20+X30)+A13*B2*DEXP(X20+X30))/ALPHA**2+(-2.0*B2**2*A12*DEXP(2.*
2X20)*(B2*DEXP(X20)+DEXP(X30))+2.0*B2*B3*A23*DEXP(2.*X20+X30)-2.0*B
32*A13*DEXP(X20+X30)*(B2*DEXP(X20)+DEXP(X30)))/ALPHA**3.
  A(1,3)=(B2*A12*DEXP(X20+X30)-B3*A23*DEXP(X20+X30)+2.0*A13*DEXP(2.*
1X30)+B2*A13*DEXP(X30+X20))/ALPHA**2+(-2.0*B2*A12*DEXP(X20+X30)*(B2
2*DEXP(X20)+DEXP(X30))+2.*B3*A23*DEXP(X20+2.*X30)-2.0*A13*DEXP(2.*X
330)*(B2*DEXP(X20)+DEXP(X30)))/ALPHA**3.

```

```

A(1,4)=-RG*T-(-2.0*B2*B3*A12*DEXP(Y20+Y10)*(B2*DEXP(Y20)+DEXP(Y30)
1)+2.0*B3**2*A23*DEXP(Y20+Y30+Y10)-2.0*B3*A13*DEXP(Y10+Y30))*(B2*DEX
2P(Y20)+DEXP(Y30)))/BETA**3.
A(1,5)=-(-2.0*B2**2*A12*DEXP(2.*Y20)+B2*A12*DEXP(Y20+Y30)-B3*A23*DE
1XP(Y20+Y30)+A13*B2*DEXP(Y20+Y30))/BETA**2-(-2.0*B2**2*A12*DEXP(2.0
2*Y20)*(B2*DEXP(Y20)+DEXP(Y30))+2.0*B2*B3*A23*DEXP(2.*Y20+Y30)-2.0*
3B2*A13*DEXP(Y20+Y30))*(B2*DEXP(Y20)+DEXP(Y30)))/BETA**3.
A(1,6)=-(-B2*A12*DEXP(Y20+Y30)-B3*A23*DEXP(Y20+Y30)+2.*A13*DEXP(2.*
1Y30)+B2*A13*DEXP(Y30+Y20))/BETA**2-(-2.0*B2*A12*DEXP(Y30+Y20)*(B2*
2DEXP(Y20)+DEXP(Y30))+2.0*B3*A23*DEXP(Y20+Y30)-2.0*A13*DEXP(2.*Y30)
3*(B2*DEXP(Y20)+DEXP(Y30)))/BETA**3.
A(2,1)=(2.0*B2*B3*A12*DEXP(2.*X10)+B2*A12*DEXP(X10+X30)-B2*A13*DEX
1P(X10+X30)+A23*B3*DEXP(X10+X30))/ALPHA**2+(-2.0*B2*B3*A12*DEXP(2.*
2X10)*(B3*DEXP(X10)+DEXP(X30))+2.0*B2*B3*A13*DEXP(2.*X10+X30)-2.0*A
323*B3*DEXP(X10+X30)*(B3*DEXP(X10)+DEXP(X30)))/ALPHA**3.
A(2,2)=RG*T+(-2.0*B2**2*A12*DEXP(X10+X20)*(B3*DEXP(X10)+DEXP(X30))
1+2.0*B2**2*A12*DEXP(X10+X20+X30)-2.0*B2*A23*DEXP(X20+X30)*(B3*DEXP
2(X10)+DEXP(X30)))/ALPHA**3.
A(2,3)=(B2*A12*DEXP(X10+X30)-B2*A13*DEXP(X10+X30)+2.0*A23*DEXP(2.*
1X30)+A23*B3*DEXP(X10+X30))/ALPHA**2+(-2.0*B2*A12*DEXP(X10+X30)*(B3
2*DEXP(X10)+DEXP(X30))+2.0*B2*A13*DEXP(X10+2.*X30)-2.0*A23*DEXP(2.*
3X30)*(B3*DEXP(X10)+DEXP(X30)))/ALPHA**3.
A(2,4)=-(-2.0*B2*B3*A12*DEXP(2.*Y10)+B2*A12*DEXP(Y10+Y30)-B2*A13*DE
1XP(Y10+Y30)+A23*B3*DEXP(Y10+Y30))/BETA**2-(-2.0*B2*B3*A12*DEXP(2.*
2Y10)*(B3*DEXP(Y10)+DEXP(Y30))+2.0*B2*B3*A13*DEXP(2.*Y10+Y30)-2.0*A
323*B3*DEXP(Y10+Y30)*(B3*DEXP(Y10)+DEXP(Y30)))/BETA**3.
A(2,5)=-RG*T-(-2.0*B2**2*A12*DEXP(Y10+Y20)*(B3*DEXP(Y10)+DEXP(Y30)
1)+2.0*B2**2*A12*DEXP(Y10+Y20+Y30)-2.0*B2*A23*DEXP(Y20+Y30)*(B3*DEX
2P(Y10)+DEXP(Y30)))/BETA**3.
A(2,6)=-(-B2*A12*DEXP(Y10+Y30)-B2*A13*DEXP(Y10+Y30)+2.0*A23*DEXP(2.*
1*Y30)+A23*B3*DEXP(Y10+Y30))/BETA**2-(-2.0*B2*A12*DEXP(Y10+Y30)*(B3
2*DEXP(Y10)+DEXP(Y30))+2.0*B2*A13*DEXP(Y10+2.*Y30)-2.0*A23*DEXP(2.*
3Y30)*(B3*DEXP(Y10)+DEXP(Y30)))/BETA**3.
A(3,1)=(A23*B3*DEXP(X20+X10)-B2*A12*DEXP(X20+X10)+2.0*A13*B3*DEXP(
12.*X10)+A13*B2*DEXP(X20+X10))/ALPHA**2+(-2.0*A23*B3*DEXP(X20+X10)*

```

```

2(B3*DEXP(X10)+B2*DEXP(X20))+2.00*B2*A12*B3*DEXP(2.*X10+X20)-2.0*B3
3*A13*DEXP(2.*X10)*(B3*DEXP(X10)+B2*DEXP(X20))/ALPHA**3.
A(3,2)=(2.0*B2*A23*DEXP(2.*X20)+A23*B3*DEXP(X10+X20)-B2*A12*DEXP(X
110+X20)+A13*B2*DEXP(X10+X20))/ALPHA**2+(-2.0*B2*A23*DEXP(2.*X20)*(
2B3*DEXP(X10)+B2*DEXP(X20))+2.00*B2*A12*B2*DEXP(X10+2.*X20)-2.0*A13
3*B2*DEXP(X10+X20)*(B3*DEXP(X10)+B2*DEXP(X20))/ALPHA**3.
A(3,3)=RG*T+(-2.0*A23*DEXP(X20+X30)*(B3*DEXP(X10)+B2*DEXP(X20))+2.
100*B2*A12*DEXP(X10+X20+X30)-2.0*A13*DEXP(X10+X30)*(B3*DEXP(X10)+B2
2*DEXP(X20))/ALPHA**3.
A(3,4)=-(A23*B3*DEXP(Y10+Y20)-B2*A12*DEXP(Y10+Y20)+2.0*A13*B3*DEXP
1(2.*Y10)+A13*B2*DEXP(Y20+Y10))/BETA**2-(-2.0*A23*B3*DEXP(Y10+Y20)*
2(B3*DEXP(Y10)+B2*DEXP(Y20))+2.*B2*A12*B3*DEXP(2.*Y10+Y20)-2.0*B3*A
313*DEXP(2.*Y10)*(B3*DEXP(Y10)+B2*DEXP(Y20))/BETA**3.
A(3,5)=-(2.0*B2*A23*DEXP(2.*Y20)+A23*B3*DEXP(Y10+Y20)-B2*A12*DEXP(
1Y10+Y20)+A13*B2*DEXP(Y10+Y20))/BETA**2-(-2.0*B2*A23*DEXP(2.*Y20)*(
2B3*DEXP(Y10)+B2*DEXP(Y20))+2.00*B2*A12*B2*DEXP(Y10+2.*Y20)-2.0*A13*
3B2*DEXP(Y10+Y20)*(B3*DEXP(Y10)+B2*DEXP(Y20))/BETA**3.
A(3,6)=-RG*T-(-2.0*A23*DEXP(Y10+Y20+Y30)*(B3*DEXP(Y10)+B2*DEXP(Y20))+2
1.0*B2*A12*DEXP(Y10+Y20+Y30)-2.0*A13*DEXP(Y10+Y30)*(B3*DEXP(Y10)+B2
2*DEXP(Y20))/BETA**3.
A(4,1)=DEXP(X10)
A(4,2)=DEXP(X20)
A(4,3)=DEXP(X30)
A(4,4)=0.0
A(4,5)=0.0
A(4,6)=0.0
A(5,1)=0.0
A(5,2)=0.0
A(5,3)=0.0
A(5,4)=DEXP(Y10)
A(5,5)=DEXP(Y20)
A(5,6)=DEXP(Y30)
A(6,1)=0.0
A(6,2)=0.0
A(6,3)=0.0

```

```

A(6,4)=0.0
A(6,5)=DEXP(Y20)
A(6,6)=-SRATIO*DEXP(Y30)
R(1)=RG*T*Y10+(B2**2*A12*DEXP(2.*Y20)+B2*A12*DEXP(Y20+Y30)-B3*A23*
1DEXP(Y20+Y30)+A13*B2*DEXP(Y20+Y30)+A13*DEXP(2.*Y30))/BETA**2-RG*T*
2X10-(B2**2*A12*DEXP(2.*X20)+B2*A12*DEXP(X20+X30)-B3*A23*DEXP(X20+X
330)+A13*B2*DEXP(X20+X30)+A13*DEXP(2.*X30))/ALPHA**2
R(2)=RG*T*Y20+(B2*B3*A12*DEXP(2.*Y10)+B2*A12*DEXP(Y10+Y30)-B2*A13*
1DEXP(Y10+Y30)+A23*B3*DEXP(Y10+Y30)+A23*DEXP(2.*Y30))/BETA**2-RG*T*
2X20-(B2*B3*A12*DEXP(2.*X10)+B2*A12*DEXP(X10+X30)-B2*A13*DEXP(X10+X
330)+A23*B3*DEXP(X10+X30)+A23*DEXP(2.*X30))/ALPHA**2
R(3)=RG*T*Y30+(B3*A23*DEXP(Y10+Y20)+B2*A23*DEXP(2.*Y20)-B2*A12*DEX
1P(Y10+Y20)+A13*B3*DEXP(2.*Y10)+A13*B2*DEXP(Y10+Y20))/BETA**2-RG*T*
2X30-(B3*A23*DEXP(X10+X20)+B2*A23*DEXP(2.*X20)-B2*A12*DEXP(X10+X20)
3+A13*B3*DEXP(2.*X10)+A13*B2*DEXP(X10+X20))/ALPHA**2
R(4)=1.0-DEXP(X10)-DEXP(X20)-DEXP(X30)
R(5)=1.0-DEXP(Y10)-DEXP(Y20)-DEXP(Y30)
R(6)=SRATIO*DEXP(Y30)-DEXP(Y20)

```

C SOLUTION OF EQUATIONS USING GAUSSIAN ELIMINATION

N=6

M=1

IA=6

IDGT=5

CALL LEQTLF(A,M,N,IA,R,IDGT,WKAREA,IER)

X1P=R(1)

X2P=R(2)

X3P=R(3)

Y1P=R(4)

Y2P=R(5)

Y3P=R(6)

C CORRECTION OF INITIAL GUESS FOR NEXT ITERATION

X10=X10+X1P

X20=X20+X2P

X30=X30+X3P

Y10=Y10+Y1P

```

C      Y20=Y20+Y2P
C      Y30=Y30+Y3P
C      IER IS AN INDICATOR PERTAINING TO THE ACCURACY
C      OF THE SOLUTION TO THE SET OF EQUATIONS
C      ITERATION TEST PROCEDURE
      IF(ITER.EQ.30)GO TO 103
      TEST1=DABS(X1P)
      TEST2=DABS(X2P)
      TEST3=DABS(X3P)
      TEST4=DABS(Y1P)
      TEST5=DABS(Y2P)
      TEST6=DABS(Y3P)
      IF(TEST1.GT.0.0001)GO TO 99
      IF(TEST2.GT.0.0001)GO TO 99
      IF(TEST3.GT.0.0001)GO TO 99
      IF(TEST4.GT.0.0001)GO TO 99
      IF(TEST5.GT.0.0001)GO TO 99
      IF(TEST6.GT.0.0001)GO TO 99
      103 CONTINUE
      WRITE(6,101)IER,ITER
      101 FORMAT(2I20)
C      SWITCH BACK TO MOLE FRACTIONS FOR PRINTOUT
      X10=DEXP(X10)
      X20=DEXP(X20)
      X30=DEXP(X30)
      Y10=DEXP(Y10)
      Y20=DEXP(Y20)
      Y30=DEXP(Y30)
      WRITE(6,100)X10,X20,X30,Y10,Y20,Y30
      100 FORMAT(6F20.5)
C      COMPUTATION OF ACTIVITY COEFFICIENTS IN EACH PHASE
      PAR1=B3*X10+B2*X20+X30
      PAR2=B3*Y10+B2*Y20+Y30
      FAC1=(B2*A12*X20*(B2*X20+X30)-B3*A23*X20*X30+A13*X30*(B2*X20+X30))
      1/PAR1**2

```



```

FAC4=(B2*A12*Y20*(B2*Y20+Y30)-B3*A23*Y20*Y30+A13*Y30*(B2*Y20+Y30))/PAR2**2
FAC2=(B2*A12*X10*(93*X10+X30)-B2*A13*X10*X30+A23*X30*(B3*X10+X30))/PAR1**2
FAC5=(B2*A12*Y10*(B3*Y10+Y30)-B2*A13*Y10*Y30+A23*Y30*(B3*Y10+Y30))/PAR2**2
FAC3=(A23*X20*(B3*X10+B2*X20)-B2*A12*X10*X20+A13*X10*(B3*X10+B2*X20+Y30))/PAR1**2
FAC6=(A23*Y20*(B3*Y10+B2*Y20)-B2*A12*Y10*Y20+A13*Y10*(B3*Y10+B2*Y20+Y30))/PAR2**2
ACT1=X10*DEXP(FAC1/(RG*T))
ACT2=X20*DEXP(FAC2/(RG*T))
ACT3=X30*DEXP(FAC3/(RG*T))
ACT4=Y10*DEXP(FAC4/(RG*T))
ACT5=Y20*DEXP(FAC5/(RG*T))
ACT6=Y30*DEXP(FAC6/(RG*T))
WRITE(6,600)ACT1,ACT2,ACT3,ACT4,ACT5,ACT6
600 FORMAT(6F20.5)
C
ENTHALPIES OF PRODUCT AND FUEL MIXTURES
HIF=X10*H(7)+X20*H(2)+X30*H(11)
HIP=Y10*H(7)+Y20*H(2)+Y30*H(11)
A12P=-13.965
B3P=0.00
IF(JDHF.EQ.1)A13P=-0.09569
IF(JDHF.EQ.2)A13P=-7.11
IF(JDHF.EQ.1)B2P=1.36*8.1317D-04/(2.5846-8.1317D-04*T)**2
IF(JDHF.EQ.2)B2P=1.24*8.1317D-04/(2.5846-8.1317D-04*T)**2
C
THE FOLLOWING ENTHALPY EQUATIONS HAVE BUILT INTO THEM
C
A23 EQUALLING ZERO FOR ALL TEMPERATURES
HMIXF=-T*((X10*X20*(B2*A12P+A12*B2P)+X10*X30*A13P)/PAR1-(X10*X20*B
12*A12+X10*X30*A13)*(X10*B3P+X20*B2P)/PAR1**2)+(X10*X20*B2*A12+X20
2*X30*A23+X10*X30*A13)/PAR1
HMIXP=-T*((Y10*Y20*(B2*A12P+A12*B2P)+Y10*Y30*A13P)/PAR1-(Y10*Y20*B
12*A12+Y10*Y30*A13)*(Y10*B3P+Y20*B2P)/PAR1**2)+(Y10*Y20*B2*A12+Y20
2*Y30*A23+Y10*Y30*A13)/PAR1

```

```

HTOTF=HIF+HMXF
HTOTP=HIP+HMXP
WRITE(6,201)HIF
WRITE(6,203)HMXF
WRITE(6,205)HTOTF
WRITE(6,202)HIP
WRITE(6,204)HMXP
WRITE(6,206)HTOTP
201 FORMAT(20H FUEL IDEAL ENTHALPY,E20.5,9H CAL/MOLE)
202 FORMAT(20H PROD IDEAL ENTHALPY,E20.5,9H CAL/MOLE)
203 FORMAT(20H FUEL MIX ENTHALPY ,E20.5,9H CAL/MOLE)
204 FORMAT(20H PROD MIX ENTHALPY ,E20.5,9H CAL/MOLE)
205 FORMAT(20H FUEL TOT ENTHALPY ,E20.5,9H CAL/MOLE)
206 FORMAT(20H PROD TOT ENTHALPY ,E20.5,9H CAL/MOLE)
C ENERGY RELEASE COMPUTATIONS
POWER=25.0
C LITHIUM IN AT 500 F, SF6 IN AT 90 F
ENER=2286.707*(8.0+6.0*Y10/Y20)-291618.2-(6.0/Y20)*HTOTP
ENERGY=7.957D-06*ENER
WRITE(6,207)ENERGY
207 FORMAT(15H ENERGY RELEASE,E20.5,20H KILOWATTS/KG/HR SF6)
DOTOX=POWER/ENERGY
DOTFI=0.3801*DOTOX
WLI=0.006939
WLIF=0.02594
WLI2S=0.04594
WSF6=0.146066
DOTP=((WLI*Y10+WLIF*Y20+WLI2S*Y30)/WSF6)*(6.0/Y20)*DOTOX
DOTFL=(WLI*Y10/WSF6)*(6.0/Y20)*DOTOX
DOTFT=DOTFI+DOTFL
PERBUR=100.0*DOTFI/DOTFT
ALL DENSITIES IN GM/CC
RHOLI=0.562-0.1D-03*T
RHOLIF=2.3581-0.4902D-03*T
RHOLIS=1.7476-0.2940D-03*T

```

```

C      DENSITY OF FUEL AND PROD ASSUMES NO VOLUME CHANGE ON MIXING
WF=6.939*X10+25.94*X20+45.94*X30
WP=6.939*Y10+25.94*Y20+45.94*Y30
VF=6.939*X10/RHOLI+25.94*X20/RHOLIF+45.94*X30/RHOLIS
VP=6.939*Y10/RHOLI+25.94*Y20/RHOLIF+45.94*Y30/RHOLIS
DENF=WF/VF
DENP=WP/VP
WRITE(6,208)POWER,DOTX      DX FLOW,E20.5
208 FORMAT(12H POWER LEVEL,E20.5,10H KILOWATTS,14H
1,6H KG/HR)
WRITE(6,209)DOTP
209 FORMAT(18H PRODUCT FLOW RATE,E20.5,6H KG/HR)
WRITE(6,210)DOTFT,PERBUR
210 FORMAT(10H FUEL FLOW,E20.5,6H KG/HR,15H PERCENT BURNED,E20.5,2H %)
WRITE(6,212)DENF,DENP
212 FORMAT(13H FUEL DENSITY,E20.5,6H GM/CC,13H PROD DENSITY,E20.5,6H G
1M/CC)
C      COMPUTATION OF EQUILIBRIUM CONSTANTS
CLI=DEXP((FENER(7)-FENER(8))/(RG*T))
CLIF=DEXP((FENER(2)-FENER(3))/(RG*T))
CLI2S=DEXP((FENER(11)-FENER(12))/(RG*T))
CLIF2=DEXP((2.*FENER(3)-FENER(4))/(RG*T))
CLIF3=DEXP((3.*FENER(3)-FENER(5))/(RG*T))
CLI2=DEXP((12.*FENER(8)-FENER(9))/(RG*T))
WRITE(6,890)
890 FORMAT(59H EQUILIBRIUM CONSTANTS FOLLOW,LI,LIF,LI2S,(LIF)2,(LIF)3,
1LI2)
WRITE(6,891)CLI,CLIF,CLI2S,CLIF2,CLIF3,CLI2
891 FORMAT(6E16.5)
PRLI=ACT1*CLI
PRLIF=ACT2*CLIF
PRLI2S=ACT3*CLI2S
PRLIF2=CLIF2*PRLIF**2
PRLIF3=CLIF3*PRLIF**3.
PRLI2=CLI2*PRLI**2

```

```

PRA=1.00-PRLI-PRLIF-PRLI2S-PRLIF2-PRLIF3-PRLI2
WRITE(6,713)PRLI,PRLIF,PRLI2S
713 FORMAT(9H LI PRESS,E15.5,4H ATM,10H LIF PRESS,E15.5,4H ATM,11H LI2
IS PRESS,E15.5,4H ATM)
WRITE(6,714)PRLIF2,PRLIF3
714 FORMAT(13H (LIF)2 PRESS,E15.5,4H ATM,13H (LIF)3 PRESS,E15.5,4H ATM
1)
WRITE(6,715)PRLI2,PRA
715 FORMAT(10H LI2 PRESS,E15.5,4H ATM,12H ARGON PRESS,E15.5,4H ATM)
WRITE(6,211)
211 FORMAT(20H *****)
C CHANGE TO LOGS FOR USE AS STARTING VALUE ON NEXT ITERATION
X10=DLOG(X10)
X20=DLOG(X20)
X30=DLOG(X30)
Y10=DLOG(Y10)
Y20=DLOG(Y20)
Y30=DLOG(Y30)
T=T+10.0
999 CONTINUE
911 CONTINUE
STOP
END
DATA INPUT DD *
0.56055500D+01 0.15340000D+02 0.84474600D+01 0.19049520D+02
0.28513590D+02 0.15199880D+01 0.85996800D+01 0.49256600D+01
0.88603100D+01 0.26330000D+02 0.20913349D+02 0.00000000D+00
0.19803330D+02 0.00000000D+00 0.49473900D+00 0.60634000D+00
0.23861400D+01 0.20017000D+02-0.44781500D+01 0.80856000D-01
0.38434600D+00-0.29953000D+02 0.16972300D+00 0.00000000D+00
-0.18625410D+02 0.00000000D+00-0.87318000D-01-0.14845900D+00
-0.58192200D+00-0.19339930D+02 0.38475000D+01-0.82874000D-01
-0.14783000D-01 0.34122000D+02-0.70770000D-01 0.00000000D+00
0.74345500D+01 0.00000000D+00 0.69181000D-02 0.11843300D-01
0.46232000D-01 0.34183100D+01-0.10997230D+01 0.29229200D-01

```

0.11936000D-02-0.11035000D+02 0.99600000D-02 0.00000000D+00
0.92950000D-03 0.00000000D+00-0.23253000D-01-0.40610000D-01
-0.15627000D+00-0.12510000D-03-0.97140000D-03 0.98640000D-02
-0.37710000D-02-0.42067000D+00-0.41018710D+00 0.00000000D+00
-0.14839393D+03-0.14765460D+03-0.84257519D+02-0.23134498D+03
-0.37144235D+03-0.11809622D+01-0.18332665D+01 0.36960730D+02
0.47675271D+02-0.12590725D+03-0.12381550D+03 0.00000000D+00
0.10187004D+02 0.28833157D+02 0.57309917D+02 0.82746138D+02
0.10851148D+03 0.36466384D+01 0.19677763D+02 0.39111723D+02
0.57517269D+02 0.57413000D+02 0.44094000D+02 0.00000000D+00
-0.14600000D+03-0.14308100D+03-0.81450000D+02-0.22533000D+03
-0.36262000D+03 0.00000000D+00 0.56900000D+00 0.38410000D+02
0.50400000D+02-0.11770000D+03-0.11620000D+03-0.59447760D+02

APPENDIX B

THERMOCHEMICAL PROPERTY DATA

B.1 Thermodynamic Properties of Li(s,l,g), Li₂(g), LiF(s,l,g), Li₂F₂(g), Li₃F₃(g), and SF₆(g)

The thermodynamic properties of Li(s,l,g), Li₂(g), LiF(s,l,g), Li₂F₂(g), Li₃F₃(g) and SF₆(g) were taken from the JANAF Thermochemical Tables [10]. The symbols s, l, and g signify solid, liquid, and gas phases, respectively. The data were inserted into the computer program by utilizing polynomial curve fits available from JANAF.

B.2 Thermodynamic Properties of Li₂S(s,l,g)

The information available in the literature on the properties of Li₂S is very limited. The heat of formation of Li₂S(s) at 298°K was calculated by Morris [13] to be -492.4₋₂₁ kJ/mole, and determined experimentally by Juza and Uphoff [14] to be -445.6 kJ/mole. The melting point of Li₂S was experimentally determined to be 1645₋₅⁺¹⁰°K by Cunningham, Johnson, and Cairns [15]. The boiling point of Li₂S was determined to be 2073°K by Mott [16] in an experimental study of the volatilities of various refractory materials. Since the above information was incomplete, it was necessary to estimate the remaining thermodynamic property data.

B.2.1 Thermodynamic Properties of Li₂S(s). The specific heats of Li₂S(s) were estimated by using Knopp's rule [38] with data taken from Reference [10] for Na₂S(s), Li₂O(s) and Na₂O(s). The

estimated heat capacity data were then fitted to a polynomial equation using least squares methods. The estimated heat capacities were found to be approximately 7 to 20% lower than the corresponding values for $\text{Na}_2\text{S(s)}$ depending on the temperature. Estimates of the entropy of formation of $\text{Li}_2\text{S(s)}$ were given by Steunenbergh [47] at temperatures of 623, 673, and 723°K. The estimated entropies of formation were used to determine the entropies of $\text{Li}_2\text{S(s)}$ at the given temperatures, which were in turn used in conjunction with the estimated heat capacity data to determine the entropy at 298°K. The enthalpies of $\text{Li}_2\text{S(s)}$ were determined by integration of the heat capacity equation and using the value of Morris [13] for the heat of formation at 298°K.

B.2.2 Thermodynamic Properties of $\text{Li}_2\text{S(l)}$. The heat capacities of $\text{Li}_2\text{S(l)}$ were estimated by using Knoop's rule with data taken from Reference [10] for $\text{Na}_2\text{S(l)}$, $\text{Li}_2\text{O(l)}$ and $\text{Na}_2\text{O(l)}$. The estimated data were found to be 4.2 J/mole-°K lower than the corresponding values for $\text{Na}_2\text{S(l)}$ and the data were represented by the JANAF polynomial equation for the $\text{Na}_2\text{S(l)}$ data after the proper adjustment. The heat of fusion of lithium sulfide was estimated by compiling data from References [10] and [48] through [51] on the melting points and heats of fusion of alkali metal-halogen salts, lithium and sodium oxides, alkali metal sulfates, and sodium sulfide. The entropies of fusion, ΔS_f , were obtained by noting:

$$\Delta S_f = \frac{\Delta H_f}{T_f} \quad (\text{B.1})$$

The entropies of fusion of the various compounds were plotted against the molecular weight of the participating alkali metal. Definite trends were noticed in the curves, especially between the lithium and sodium compounds. By continuing the trends, the entropy of fusion of Li_2S was estimated to be 3.8 ± 1.2 J/mole-°K. By employing Equation (B.1) and the melting point of Cunningham, et al., [15], the heat of fusion was estimated to be 6.19 ± 2.1 kJ/mole. The estimated value was taken to be 7.24 kJ/mole in subsequent calculations as this value had been used in earlier work. A value for the heat of fusion of 49.4 kJ/mole was also considered since this value resulted in the best representation of the lithium fluoride-lithium sulfide binary solubility data. The heat of formation of a solid and liquid can be related

$$\Delta H_f = H_{\text{form}_T_f}^{(l)} - \Delta H_{\text{form}_T_f}^{(s)} \quad (\text{B.2})$$

where ΔH_f is the heat of fusion at the melting point of the pure component and ΔH_{form} is the heat of formation. The variation of the heat of formation with temperature can be expressed as follows:

$$\Delta H_{\text{form}_T} = \Delta H_{\text{form}_{298}} + (h_T - h_{298})_{\text{compound}} - \sum (h_T - h_{298})_{\text{elements}} \quad (\text{B.3})$$

Combination of Equations (B.2) and (B.3) results in an expression relating the heat of formation of $\text{Li}_2\text{S}(l)$ at 298°K to the heat of formation of $\text{Li}_2\text{S}(s)$ at 298°K, the heat of fusion, and relative enthalpies of the compounds as follows:

$$\Delta H_{\text{form}298}^{(1)} = \Delta H_{\text{form}298}^{(s)} + \Delta H_f + \left[h_{T_f} - h_{298} \right]_{\text{Li}_2\text{S}(s)} - \left[h_{T_f} - h_{298} \right]_{\text{Li}_2\text{S}(l)} \quad (\text{B.4})$$

Utilizing Equation (B.4), the heat of formation of $\text{Li}_2\text{S}(l)$ was estimated to be -493.3 kJ/mole for the low heat of fusion case and -451.0 kJ/mole for the high heat of fusion case. The entropy of $\text{Li}_2\text{S}(l)$ at 298°K was equated to the entropy of $\text{Li}_2\text{S}(s)$ at 298°K plus the difference between the corresponding entropies for $\text{Na}_2\text{S}(l)$ and $\text{Na}_2\text{S}(s)$. The enthalpies of $\text{Li}_2\text{S}(l)$ were determined by integration of the heat capacity equation and using the above values for the heats of formation at 298°K .

B.2.3 Thermodynamic Properties of $\text{Li}_2\text{S}(g)$. The thermodynamic properties of $\text{Li}_2\text{S}(g)$ were estimated by application of the principles of statistical thermodynamics after the initial estimation of the required spectroscopic data.

The vibrational frequencies of the molecule were estimated by a comparison of the trends in similar diatomic and triatomic molecules. Data taken from the JANAF Thermochemical Tables [10] and used for this purpose are listed in Table 6. The vibrational frequencies were estimated simply by continuing the trends shown in molecules having hydrogen atoms substituted for lithium atoms. The first step was to estimate the simple harmonic oscillator frequency of LiS from trends shown in HN , HO , HS , LiN and LiO . It was then observed that the frequency of the triatomic ν_1 mode was approximately 3% larger than the corresponding diatomic harmonic oscillator frequency for the H_2N , H_2O , H_2S and Li_2O molecules. The ν_1 frequency of Li_2S

Table 6

Vibrational Frequency Data for Triatomic and Diatomic Molecules

Molecule	ν_1	ν_2	ν_3	Molecule	$\nu_o = \omega_e - 2\omega_e x_e$
H ₂ S 92.2°	2614	1183	2627	HS	2582
H ₂ O 104.4°	3657	1594	3756	HO	3570
H ₂ N 103°	3173	1499	3220	HN	3124
Li ₂ O 180°	760	140	987	LiO	735
				LiN	686
Li ₂ S* 180°	556	102	722	LiS*	540

*Estimated Data

was estimated accordingly. The ν_2 and ν_3 frequencies of the bent molecules were observed to be approximately in similar proportion to the corresponding ν_1 frequencies. As a result the ν_2 and ν_3 frequencies of Li_2S were taken to be in the same proportion to the ν_1 frequency as in the Li_2O case.

This method of estimation of the vibrational frequencies was expected to give only relatively crude estimates. The effects of changing these values on the thermodynamic properties was examined.

The Li-S bond distance was estimated from the Li-O bond distance in Li_2O by assuming the same fraction of the sum of the ionic bond radii of the participating atoms. The atomic radii were taken from Lange [48]. For Li_2O , the Li-O bond distance was found to equal the sum of the atomic radii multiplied by a factor of 0.779. Hence the Li-S bond distance in Li_2S was estimated to be 1.93 Å. The rotational constants were then computed using this estimated value of the bond distance. The accuracy of this method was examined by applying the same method to the H_2O , H_2N and H_2S molecules. The accuracy depends on which molecule was picked to determine the ratio, but the maximum error that resulted was only 2.8%. The effects of varying the bond distance was also examined.

The statistical thermodynamic equations utilized to compute the thermodynamic properties are summarized below. The equations are developed in any statistical thermodynamics text such as the text by Davidson [52]. All units are in J-mole^{-1} or $\text{J-mole}^{-1}\text{-}^\circ\text{K}^{-1}$.

The electronic ground state of Li_2S was assumed to be a singlet with no low-lying electronic states. This is the case for Li_2O . Hence there were no electronic contributions to the thermodynamic properties.

The translational contributions to the thermodynamic functions were computed by the following for both the linear and nonlinear molecules. The reference pressure was taken to be 101325 n-m^{-2} , and M_0 equals $1 \times 10^{-3} \text{ kg}$.

$$-\left(\frac{f-h_0}{T}\right)_{\text{trans}} = \frac{3}{2} R \ln \left(\frac{M}{M_0}\right) + \frac{5}{2} R \ln T - 30.472 \quad (\text{B.5})$$

$$\left(h-h_0\right)_{\text{trans}} = \frac{5}{2} RT \quad (\text{B.6})$$

$$s_{\text{trans}} = \frac{3}{2} R \ln \left(\frac{M}{M_0}\right) + \frac{5}{2} \ln T - 9.686 \quad (\text{B.7})$$

$$c_{p_{\text{trans}}} = \frac{5}{2} R \quad (\text{B.8})$$

The vibrational contributions are given by the following:

$$\text{where } u_i = 1.4388 \frac{\nu_i (\text{cm}^{-1})}{T(^{\circ}\text{K})}$$

$$-\left(\frac{f-h_0}{T}\right)_{\text{vib}} = R \left[\ln(1 - e^{-u_1}) + \omega_2 \ln(1 - e^{-u_2}) + \ln(1 - e^{-u_3}) \right] \quad (\text{B.9})$$

$$\left(h-h_0\right)_{\text{vib}} = RT \left[\frac{u_1}{e^{u_1}-1} + \frac{\omega_2 u_2}{e^{u_2}-1} + \frac{u_3}{e^{u_3}-1} \right] \quad (\text{B.10})$$

$$s_{\text{vib}} = R \left[\frac{u_1}{e^{u_1}-1} + \frac{\omega_2 u_2}{e^{u_2}-1} + \frac{u_3}{e^{u_3}-1} - \ln(1 - e^{-u_1}) - \omega_2 \ln(1 - e^{-u_2}) - \ln(1 - e^{-u_3}) \right] \quad (\text{B.11})$$

$$c_{p_{\text{vib}}} = R \left[\frac{u_1^2 e^{u_1}}{(e^{u_1}-1)^2} + \frac{\omega_2 u_2^2 e^{u_2}}{(e^{u_2}-1)^2} + \frac{u_3^2 e^{u_3}}{(e^{u_3}-1)^2} \right] \quad (\text{B.12})$$

The bending vibration ν_2 is nondegenerate, $\omega_2 = 1$, for the bent molecule and doubly degenerate, $\omega_2 = 2$, for the linear molecule.

The rotational contributions are given by the following. For the linear case:

$$-\left(\frac{f-h_o}{T}\right)_{\text{rot}} = \left[R - \ln\left(\frac{h'cB'}{kT}\right) - \ln \sigma + \frac{h'cB'}{3kT} + \frac{1}{90} \left(\frac{h'cB'}{kT}\right)^2 \right] \quad (\text{B.13})$$

$$(h-h_o)_{\text{rot}} = RT \left[1 - \frac{h'cB'}{3kT} - \frac{1}{45} \left(\frac{h'cB'}{kT}\right)^2 \right] \quad (\text{B.14})$$

$$s_{\text{rot}} = R \left[1 - \ln\left(\frac{h'cB'}{kT}\right) - \ln \sigma - \frac{1}{90} \left(\frac{h'cB'}{kT}\right)^2 \right] \quad (\text{B.15})$$

$$c_{p_{\text{rot}}} = R \left[1 + \frac{1}{45} \left(\frac{h'cB'}{kT}\right)^2 \right] \quad (\text{B.16})$$

where

$$B' = \frac{h'}{8\pi^2 cI} \quad (\text{B.17})$$

For the bent case:

$$-\left(\frac{f-h_o}{T}\right)_{\text{rot}} = R \left[\frac{1}{2} \ln D' + \frac{3}{2} \ln T - \ln \sigma + \frac{1}{2} \ln \left(\frac{512 \pi^7 R^3}{h^6} \right) \right] \quad (\text{B.18})$$

$$(h-h_o) = \frac{3}{2} RT \quad (\text{B.19})$$

$$s_{\text{rot}} = R \left[\frac{1}{2} \ln(D' \times 10^{117}) + \frac{3}{2} \ln T - \ln \sigma \right] - 0.138 \quad (\text{B.20})$$

$$c_{p_{\text{rot}}} = \frac{3}{2} R \quad (\text{B.21})$$

where

$$D' = I_A I_B I_C \quad (\text{B.22})$$

The symmetry number (σ) for both the linear and bent molecules is equal to two due to the symmetric structure of the molecule.

The total thermodynamic quantities are given by summation of the electronic, translational, rotational and vibrational contributions. The physical constants used in the calculation were taken from Davidson [52].

Properties were computed for both the linear molecule and bent molecule utilizing the estimated data. The Li-S-Li bond angle was taken to be 100 degrees in the bent case. To examine changes brought about by variances in the assumed data, four additional cases were examined for each configuration as follows: (a) vibrational frequencies doubled, bond distance fixed; (b) vibrational frequencies halved, bond distance fixed; (c) base vibrational frequencies, bond distance reduced by 10%; and (d) base vibrational frequencies, bond distance increased by 10%.

Table 7 lists the percent deviation of the indicated thermodynamic quantities from the values given by the base case at a temperature of 1200°K. The base case was the linear molecule in conjunction with previously estimated spectroscopic data. It is believed that the estimated spectroscopic data is much more precise than the variances examined and therefore it is believed that the estimated thermodynamic data is accurate to within $\pm 5\%$.

The heat of formation of $\text{Li}_2\text{S(g)}$ was required to determine the values of the absolute enthalpies. The heat of formation was determined by choosing a value which when used in conjunction with the data previously estimated, computed the boiling point given by Mott [16]. The values determined were -220.2 kJ/mole for the low

Table 7

Effects of Various Assumptions on the Thermodynamic Properties

Case	c_p^o		s^o		$-(f^o - h^o_o)/T$		$h^o - h^o_o$	
	Linear	Bent	Linear	Bent	Linear	Bent	Linear	Bent
Base Case	0.0	-6.7	0.0	+2.4	0.0	+4.2	0.0	-6.6
Vibrational Frequency Doubled	-3.6	-10.2	-6.7	-2.6	-6.2	-0.1	-8.9	-14.6
Vibrational Frequency Halved	-1.0	-5.8	+6.9	+7.6	+7.3	+9.4	+5.5	-1.5
Bond Distance Decreased 10%	0.0	-6.7	-0.5	+1.6	-0.6	+3.2	0.0	-6.6
Bond Distance Increased 10%	0.0	-6.7	+0.5	+3.1	+0.6	+5.1	0.0	-6.6

heat of fusion case, and -177.9 kJ/mole for the high heat of fusion case.

A check on the above estimation was made by computation of the implied heat of vaporization. At the boiling point the following holds:

$$\Delta H_b = \Delta H_{\text{form}_{T_b}}(g) - \Delta H_{\text{form}_{T_b}}(l) \quad (\text{B.23})$$

where ΔH_b is the heat of vaporization and T_b is the boiling temperature. Substitution of Equation (B.3) yields:

$$\begin{aligned} \Delta H_b = & H_{\text{form}_{298}}(g) - H_{\text{form}_{298}}(l) + \left(h_{T_b} - h_{298} \right)_{\text{Li}_2\text{S}(g)} \\ & - \left(h_{T_b} - h_{298} \right)_{\text{Li}_2\text{S}(l)} \end{aligned} \quad (\text{B.24})$$

The value for the heat of vaporization was determined to be 230 kJ/mole for both the high and low heats of fusion cases. The value agrees well with the value of 182 kJ/mole determined by application of Trouton's rule [38] which states that the entropy increase upon boiling is 87.9 J/mole-°K.

B.3 Densities of Li(l), LiF(l) and Li₂S(l)

The density of pure lithium was taken from Davison [12], and the density of pure lithium fluoride was taken from Janz [11]. The density of pure liquid lithium sulfide is not reported in the literature. The density of solid lithium sulfide at 298°K was given by Murlot [17] to be in the range 1630 to 1700 kg/m³. Zintl, et al., [18] examined the structure of the solid and determined the density

to be 1640 kg/m^3 at 298°K . Beck [19] presented a correlation between the volume contraction of the constituent elements and the energy of formation upon chemical reaction. The correlation yielded a value for the density of solid lithium sulfide of 1640 kg/m^3 . The density at 298°K was selected to be 1660 kg/m^3 , and the density variation with temperature was estimated to have a slope equal to the average slope of lithium and lithium fluoride. Density changes upon melting were neglected since such changes are small. The equations representing the variation of the density in kg/m^3 of the various components with temperature are

$$\rho_{\text{Li}} = 562. - 0.1T \quad (\text{B.25})$$

$$\rho_{\text{LiF}} = 2358.1 - 0.4902T \quad (\text{B.26})$$

$$\rho_{\text{Li}_2\text{S}} = 1748. - 0.294T \quad (\text{B.27})$$

APPENDIX C

THEORETICAL DEVELOPMENT OF EXPRESSIONS USED TO DETERMINE THERMODYNAMIC MODEL PARAMETERS

C.1 Expressions Relating to Solid-Liquid Equilibria

The development presented below is based on a similar analysis given in Reference [34]. At the freezing temperature, T_{f_1} , of component 1, the free energies of the pure solid and pure liquid are related as follows:

$$f_1(s) \Big|_{T_{f_1}} = f_1^o \Big|_{T_{f_1}} \quad (C.1)$$

If it is assumed that solid solutions are not formed, then the free energies of the solid and liquid phases in equilibrium at a temperature T and a mole fraction x_1 are related by

$$f_1(s) \Big|_T = \bar{f}_1(\text{solu}, x_1) \Big|_T \quad (C.2)$$

Equations (C.1) and (C.2) are combined and the effects of composition and temperature changes are separated by writing

$$\begin{aligned} (\bar{f}_1(\text{solu}, x_1) - f_1^o) \Big|_{T_{f_1}} &= (f_1(s) - \bar{f}_1(\text{solu}, x_1)) \Big|_T \\ &\quad - (f_1(s) - \bar{f}_1(\text{solu}, x_1)) \Big|_{T_{f_1}} \end{aligned} \quad (C.3)$$

Equation (2.5) is evaluated at temperature T_{f_1} , and is substituted into Equation (C.3). The resulting equation is rearranged and expressed as the following integral relationship:

$$R \ln a_1 \Big|_{T_{f_1}} = \int_{T_{f_1}}^T d \left[\frac{f_1(s) - \bar{f}_1(\text{solu}, x_1)}{T} \right] \quad (\text{C.4})$$

It is noted that at constant pressure

$$d \left(\frac{\Delta f}{T} \right) = \frac{-\Delta h}{T^2} dT \quad (\text{C.5})$$

and Equation (C.5) can be written as

$$R \ln a_1 \Big|_{T_{f_1}} = \int_{T_{f_1}}^T \frac{\bar{h}_1(\text{solu}, x_1) - h_1(s)}{T^2} dT \quad (\text{C.6})$$

The relative molal heat content is defined as

$$\bar{k}_1 \equiv \bar{h}_1(\text{solu}, x_1) - h_1^0 \quad (\text{C.7})$$

with the molal enthalpy $\bar{h}_1(\text{solu}, x_1)$ defined as

$$\bar{h}_1(\text{solu}, x_1) = \left. \frac{\partial H}{\partial n_1} \right|_{n_j (j \neq 1), P, T} \quad (\text{C.8})$$

The heat of fusion is approximated by

$$\Delta H_{f_1} = h_1^0 - h_1(s) = \Delta H_{f_1}^{T_f} + \Delta c_{p_1} (T - T_{f_1}) \quad (\text{C.9})$$

where $\Delta H_{f_1}^{T_f}$ is the standard heat of fusion of component 1 at its melting temperature, and Δc_{p_1} is the difference between the partial molal heat capacity of component 1 in solution and the molal heat capacity of the solid. Substitution of Equations (C.7) and (C.9) into Equation (C.6) yields

$$R \ln a_1 \Big|_{T_{f_1}}^T = \int_{T_{f_1}}^T \frac{\bar{k}_1}{T^2} dT \frac{-\Delta H_{f_1} T_f \theta_1}{T T_{f_1}} + \Delta c_{p_1} \left[\frac{\theta_1}{T} + \ln \left(\frac{T}{T_{f_1}} \right) \right] \quad (C.10)$$

where

$$\theta_1 = T_{f_1} - T \quad (C.11)$$

The right-hand-side of Equation (C.10) can be expressed as the sum of two parts: the term within the integral is the contribution from the enthalpy change of nonideal mixing, and the remaining terms are the contributions from the heat of fusion of component 1.

The van Laar thermodynamic model, Equation (2.10), is used to evaluate both the relative molal heat content and the activity of component 1. Equations (2.20) are evaluated at temperature T_{f_1} to yield the left-hand-side of Equation (C.10). The relative molal heat content expressions are developed from Equation (2.30). It is assumed that the empirical parameters representing the binary system, A_{ij} and B_i , vary linearly with temperature as follows:

$$\begin{aligned} A_{ij} &= A + BT \\ B_i &= a + bT \end{aligned} \quad (C.12)$$

Employing Equations (C.12), the expressions for the relative heat contents of components 1 and 2 in Binary 1-2 are

$$\bar{k}_1 = A \left[\frac{x_2^2}{(B_1 x_1 + x_2)^2} \right] + TAb \left[\frac{2.0x_1 x_2^2}{(B_1 x_1 + x_2)^3} \right] + bBT^2 \left[\frac{2.0x_1 x_2^2}{(B_1 x_1 + x_2)^3} \right] \quad (C.13)$$

$$\bar{k}_2 = A \left[\frac{B_1 x_1^2}{(B_1 x_1 + x_2)^2} \right] + ATb \left[\frac{B_1 x_1^3 - x_1^2 x_2}{(B_1 x_1 + x_2)^3} \right] + bBT^2 \left[\frac{B_1 x_1^3 - x_1^2 x_2}{(B_1 x_1 + x_2)^3} \right] \quad (C.14)$$

Substitution of the expression for the activity of component 1 given by Equation (2.20) and Equation (C.13) into Equation (C.10) yields an equation representing the thermodynamic equilibrium between solid component 1, and component 1 in solution. Substitution of the expression for the activity of component 2 given by Equation (2.20) and Equation (C.14) into Equation (C.10) yields a similar expression for component 2.

Equations (C.10) can be solved for the liquid composition as a function of temperature if the van Laar empirical parameters are known: conversely, the equations can be used in conjunction with known phase equilibria data to compute the empirical parameters. The most common phase equilibria data employed with the equations are determined from the liquidus line or freezing point depression line obtained from the lowering of the freezing point of the pure solvent on the addition of solute.

C.2 Expressions Relating to Two Equilibrated Liquid Phases

As discussed in Section 2.3, the requirement for two phases to exist in equilibrium reduces to the activities of each component being identical in each of the two phases. If the two phases are indicated by mole fractions x_1 and y_1 , the requirement can be stated as

$$a_1(x_1) = a_1(y_1) \quad (C.15)$$

The van Laar model for the activity coefficients, Equations (2.20), is employed to yield

$$\begin{aligned} \ln x_1 + \frac{A_{12}}{RT} \left(\frac{x_2}{B_1 x_1 + x_2} \right)^2 &= \ln y_1 + \frac{A_{12}}{RT} \left(\frac{y_2}{B_1 y_1 + y_2} \right)^2 \\ \ln x_2 + \frac{A_{12}}{B_1 RT} \left(\frac{B_1 x_1}{B_1 x_1 + x_2} \right)^2 &= \ln y_2 + \frac{A_{12}}{B_1 RT} \left(\frac{B_1 y_1}{B_1 y_1 + y_2} \right)^2 \end{aligned} \quad (C.16)$$

Equations (C.16) can be solved for the two unknown empirical parameters, B_1 and A_{12} , as a function of temperature and the equilibrium compositions as follows:

$$B_1 = \frac{\left[\frac{\ln(y_1/x_1)}{\ln(y_2/x_2)} \right] \left(x_2^2 y_1^2 - x_1^2 y_2^2 \right) + 2 \left(y_1 y_2 x_2^2 - x_1 x_2 y_2^2 \right)}{2 \left[\frac{\ln(y_1/x_1)}{\ln(y_2/x_2)} \right] \left(y_1 y_2 x_1^2 - x_1 x_2 y_1^2 \right) + \left(x_1^2 y_2^2 - x_2^2 y_1^2 \right)} \quad (C.17)$$

$$A_{12} = \frac{RT \ln (y_1/x_1)}{\left[\left(\frac{x_2}{B_1 x_1 + x_2} \right)^2 - \left(\frac{y_2}{B_1 y_1 + y_2} \right)^2 \right]} \quad (C.18)$$

Equations (C.17) and (C.18) are solved for the empirical parameters at a given temperature from knowledge of the compositions of the two equilibrated liquid phases at that temperature.

APPENDIX D

BATH SAMPLE ANALYSIS PROCEDURE

D.1 Lithium Fluoride and Lithium Sulfide Determination

The number of moles of lithium fluoride and lithium sulfide in both the fuel-rich and product-rich bath samples were determined using the following wet-test chemical analysis procedure.

D.1.1 Sulfide Separation. The lithium sulfide was separated from the samples using a distillation procedure described by Luke [53]. A schematic of the apparatus is shown in Figure 25. A 500 ml Erlenmeyer flask was used for both the sample flask and the receiving flask.

The sample which had been prepared for analysis was introduced to the sample flask under an argon atmosphere in a dry box. The sample flask was then introduced to the distillation apparatus. A sufficient quantity of distilled water was added through the separatory funnel to ensure complete solution of the lithium fluoride. The solubility of lithium fluoride in water is approximately 0.13 gm per 100 cm³ at 298°K. For fuel-rich samples of approximately 1.0 gm and product-rich sample of approximately 0.10 gm, 300 and 350 cm³ of water were added, respectively. The sample solution was acidified by adding 130 cm³ of one molar hydrochloric acid to the fuel-rich samples and 50 cm³ of half molar hydrochloric acid to the product-rich samples. An argon purge transferred the evolved hydrogen sulfide gas to the receiving flask positioned in an ice bath and

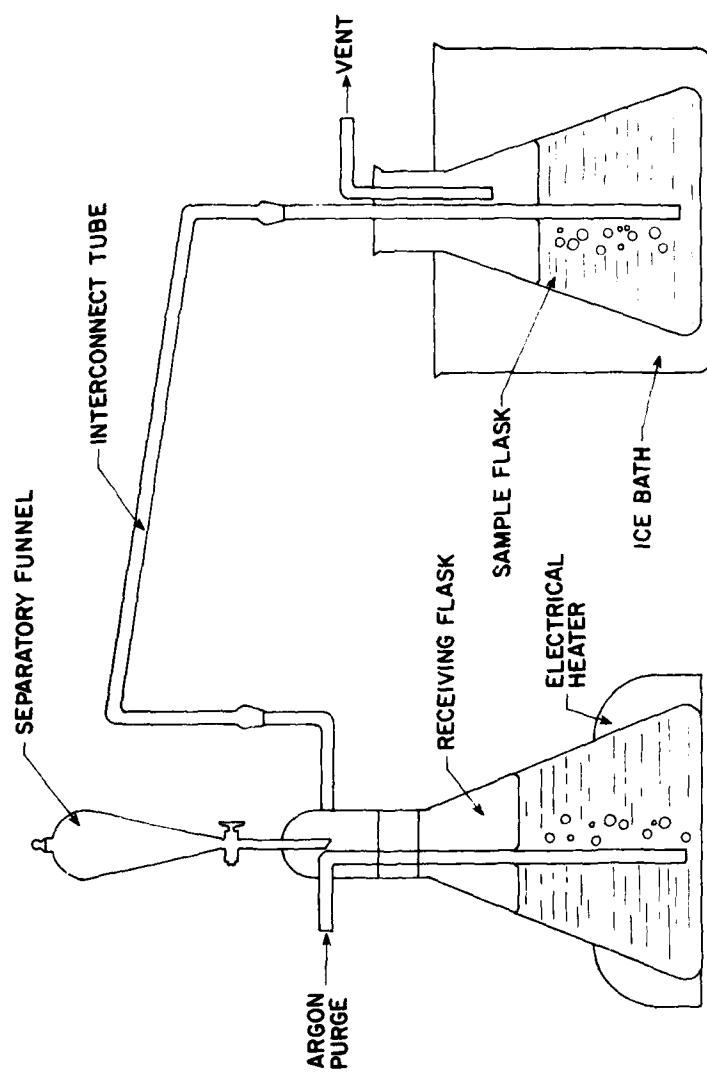


Figure 25 Distillation Apparatus

containing 350 cm³ of water and 40 cm³ of ammonical zinc sulfate solution. The sample solution was heated for a total of 36 minutes of which approximately 12 minutes were at a slow boil condition. The sample flask contained F⁻ and Li⁺ ions from the three sources of free lithium, lithium fluoride and lithium sulfide.

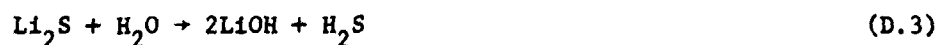
D.1.2 Lithium Sulfide Determination. Reagents:

1. Ammonical Zinc Sulfate Solution - dissolve 50.0 gm ZnSO₄·7H₂O in 250 ml NH₄OH (28% NH₃).
2. Potassium Iodide - KI - 0.50 M.
3. Potassium Iodate - KIO₃ - 0.05 M.
4. Soluble Starch - 1% in H₂O.

The procedure described by Luke [53] was utilized. The solution in the receiving flask was transferred to a larger flask with the aid of distilled water. Sufficient KI and HCl was added to provide an excess of H⁺ and I⁻ in the solution. Starch indicator was added, and the solution was titrated with KIO₃ until the appearance of a permanent blue color indicating the presence of I₂. The following equations described the process:



The number of moles of H₂S present is three times the number of moles of IO₃⁻ added during the titration. The H₂S was produced by the following reaction:



Therefore the number of moles of Li_2S present also equals three times the number of moles of IO_3^- added.

D.1.3 Lithium Fluoride Determination. Reagents:

1. Thorium Nitrate - $\text{Th}(\text{NO}_3)_4$ - 0.025 M.

The procedure described by Willard and Winter [54] was utilized. The solution remaining in the sample flask was transferred to a graduated cylinder and the volume determined. A 20 cm^3 aliquot was measured with a hypodermic syringe and transferred to a graduated cylinder. Twenty cm^3 of ethyl alcohol were added to the cylinder along with three drops of alizarin Red S indicator (1%). The solution was titrated with thorium nitrate until the appearance of a faint pink color. The thorium nitrate precipitated thorium fluoride which is insoluble in ethyl alcohol, and the indicator detected the point where all the fluoride was precipitated. The titration was repeated for five twenty cm^3 samples. The following equation describes the process:



The number of moles of F^- present is four times the number of moles of $\text{Th}(\text{NO}_3)_4$ added multiplied by the ratio of the total solution volume to the sample volume.

D.2 Lithium Determination

Different methods were used to determine the lithium content of the product-rich and fuel-rich samples.

D.2.1 Product-Rich Samples. The method of determining the free lithium contained in the product-rich sample was based on the measurement of the H_2 released by the following reaction.



The combustor sample (approximately 10 grams) was accurately weighed and placed in a glass chamber with a volume of 9957 cm^3 . The chamber was evacuated and backfilled with argon gas to atmospheric pressure. The chamber pressure was measured with a Meriam Model 31EC10, 60 inch, mercury filled absolute manometer. A known quantity of distilled water (approximately 450 cm^3) was added to the chamber. After twenty minutes, the system pressure and temperature were recorded. The total number of moles of argon, water vapor, hydrogen sulfide and hydrogen present in the sample chamber were therefore known by the ideal gas law.

The hydrogen measurement system consisted of a Fisher-Hamilton Model 29 gas partitioner equipped with a 80/100 mesh 5-A molecular sieve. The gas sample was introduced to the partitioner through a 0.5 cm^3 sample loop which is integral with the device. The output from the thermal conductivity detector was recorded on a Leeds and Northrup Model W Speedomax recorder. The detection system was calibrated with prepared samples of H_2 in argon. Therefore, from the recorder output the ratio of the number of moles of H_2 to the number of moles of argon in the sample was determined.

The gas partitioner was connected to the sample chamber. The gas sample circuit was evacuated and then opened to the sample chamber. A gas sample of approximately 80 cm^3 was extracted from

the sample chamber. The gas sample pressure was reduced to atmospheric pressure and sent through the gas partitioner column for detection. The output gave the ratio of the number of moles of H_2 to the number of moles of argon, water vapor, and hydrogen sulfide. The gas sample pressure and temperature had to be corrected to that of the calibration standard. The information from the gas partitioner combined with the knowledge of the total number of moles of gas present in the sample chamber yielded the total number of moles of H_2 evolved. Employing Equation (D.5) yielded the total number of moles of free lithium in the sample.

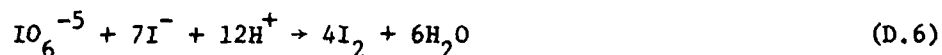
D.2.2 Fuel-Rich Samples. The free lithium content of the fuel-rich samples was obtained by subtracting the sum of the lithium fluoride and lithium sulfide weights from the total sample weight. The difference procedure was accurate for the samples analyzed because the samples were greater than 95% lithium on a mole fraction basis. A procedure was examined that permitted the direct measurement of the total Li^+ content of the sample. The procedure can be applied in situations where the difference method cannot be used accurately. The procedure is described by Rogers and Calley [55].

Reagents:

1. Periodate Reagent - 24.0 gm KOH, 10.0 gm KIO_4 , 100 ml H_2O .
2. Sodium Thiosulfate - $Na_2S_2O_3$ - 0.1 M.
3. Sulfuric Acid - H_2SO_4 - 1.0 N.
4. Potassium Hydroxide - KOH - 4.0 N.

A 5.0 cm^3 aliquot of the sample solution was measured with a hypodermic syringe and transferred to a 50 cm^3 beaker maintained at

60°-70°C by a heated water bath. The periodate reagent was added in a dropwise manner from a buret, and the lithium was precipitated as a complex periodate mixture ($\sim \text{Li}_5\text{IO}_6$). The precipitate was filtered and washed with KOH, and dissolved in H_2SO_4 . Sufficient KI was added to ensure complete conversion of the lithium periodate to I_2 . Starch indicator was added to indicate the presence of I_2 . The solution was titrated with $\text{Na}_2\text{S}_2\text{O}_3$ until the disappearance of the blue color. The following equations describe the process:



The number of moles of Li present is equal to 5/8 of the number of moles of $\text{Na}_2\text{S}_2\text{O}_3$ titrated to the solution multiplied by the ratio of the total solution volume to the sample volume. The process was calibrated with known lithium samples for a range of lithium concentrations, since the ratio can vary slightly with concentrations. The above analysis was repeated for five samples.

APPENDIX E

OXIDIZER UTILIZATION TESTS

E.1 Apparatus and Procedure

The oxidizer utilization efficiency tests were conducted on two radiatively cooled pot-type combustors of different size. The oxidizer was injected into the molten bath through a coaxial injector mounted at depths of 5.0 to 7.6 cm below the fuel surface. The utilization efficiency was determined by measuring the oxidizer concentration in the argon gas exhausted from the combustor at a known rate. The oxidizer flow rate from the combustor was then compared to the oxidizer flow rate injected into the bath.

Samples of the exhaust flow were collected in 125 cm³ evacuated sampling bulbs manufactured by the Arthur H. Thomas Company (P/N 5585-K15). The lithium vapor was removed from the sample prior to entry into the sampling bulb to protect the gas analysis system from contamination by passing the sample through a one-pass felt metal screen. Calibration tests revealed no measurable influence of the screen on the oxidizer concentration in the sample.

A Perkin-Elmer model 880 gas chromatograph was used for the analysis of the argon-oxidizer gas mixture. The separating column was stainless steel, 6.35 mm O.D. by 122 cm in length, and was packed with 80-100 mesh silica gel. The column was placed in an ice bath and operated at 0°C. The system was calibrated with prepared samples of SF₆-argon mixtures. The prepared samples had concentration

of SF_6 of 938, 1930, 5680 and 7050 parts per million. Preparation tolerances were estimated to be $\pm 10\%$ for the low concentrations and $\pm 3\%$ for the high concentrations. A commercially prepared sample of concentration 106 parts per million with a tolerance of $\pm 2\%$ was purchased from Matheson Gas Products. The calibration procedure indicated that the SF_6 concentration in the argon was a linear function of the SF_6 peak area in the concentration range of interest. Helium was used as the carrier gas. SF_6 concentrations as low as 10 parts per million could be detected with the apparatus.

E.2 Results

Samples were taken approximately every 10 to 20 minutes during the 1.5 to 2 hour period following ignition. No oxidizer could be detected in the exhaust flow after the second sample taken at the 20 minute mark. Bath temperatures at this time were in the range of 944 to 1061°K with ignition occurring at a bath temperature of 572°K. Small quantities of oxidizer were detected in samples taken during the first 15 minutes following ignition, but the oxidizer utilization efficiency exceeded 99.6% for all measurements. It was concluded from the tests that the oxidizer utilization efficiency is 100% during normal combustor operation with injector submergence depths exceeding 5 cm.

APPENDIX F

APPARATUS AND PROCEDURE FOR INVESTIGATING THE WET-TANK PRODUCT COLLECTION METHOD

F.1 Apparatus

A schematic of the apparatus used to investigate the feasibility of collecting and storing the reaction products in the fuel tank is shown in Figure 26. The product liquid was maintained at a temperature of 1227°K in the upper vessel, and the lithium fuel was maintained at a temperature of 505°K in the lower vessel. The temperature of the vessels were maintained by heaters independently controlled with variacs. The product liquid was forced from the upper vessel at a flow rate of 35-55 cm³/min. into the lower vessel by an inflow of argon gas into the upper vessel. Temperatures were measured with chromel-alumel thermocouples and recorded on a Leeds and Northrup Speedomax-H null-balance recorder.

F.2 Procedure

The apparatus was stabilized at the desired temperature levels with an argon purge supplied to the upper vessel. The purge flow was exhausted through vents in the upper and lower vessels. Product liquid outflow was initiated by isolating the ullage region of the upper vessel using a series of valves and pressurizing the upper vessel with the argon inflow. The flow rate was metered by metering the argon inflow and correcting the rate for thermal expansion in the vessel. An additional estimate of the flow rate was obtained by estimating the outflow period from the temperature-time curve of the

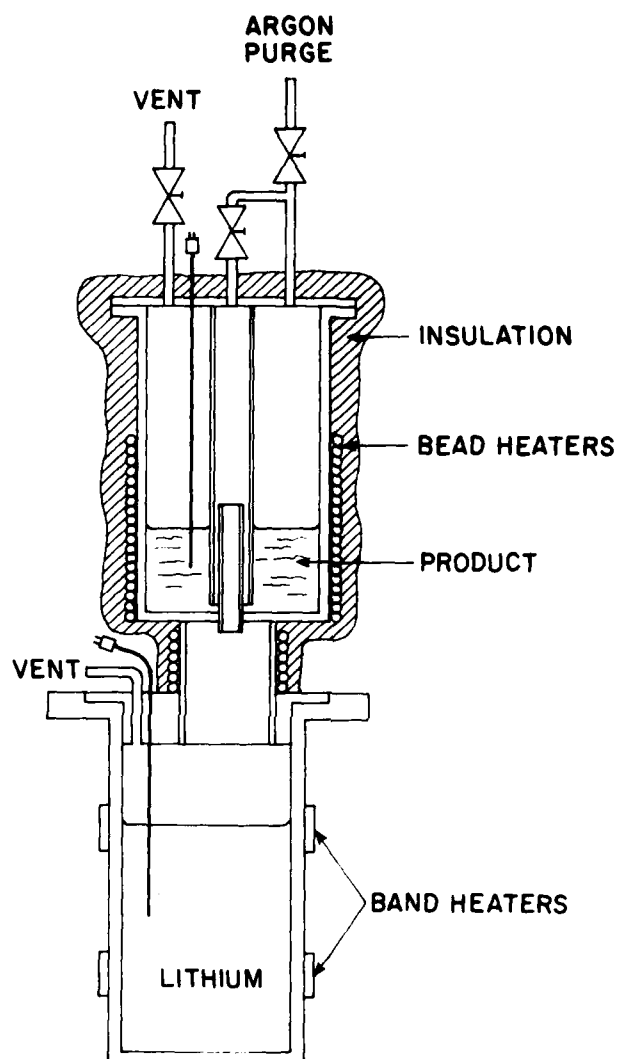


Figure 26 Wet-Tank Product Collection Apparatus

fuel bath and knowing the mass and density of the material exhausted. For tests where pure lithium fluoride was used to simulate the reaction products, the form of the exhausted material was observed by removing the lithium from the lower vessel. The lithium was removed by reacting it with water after the system had cooled. For tests where actual reaction products were used, the lithium could not be removed with water because the lithium sulfide component is soluble in water and the form of the exhausted products would be altered. The exhausted product was retrieved from the molten fuel bath with a stainless steel mesh basket placed in the bottom of the lower vessel.

F.3 Results

The results indicated that product liquid exhausted into a fuel tank at rates typical of the steady combustor examined in this study would form small spherical balls approximately 0.86 cm in diameter with a hollow core. Identical balls were found when either pure lithium fluoride or actual reaction products were used in the tests. The packing efficiency of the balls was found to be approximately 50% on a volume basis.

Distribution and Addressee Listing

<u>Addressee</u>	<u>Copies</u>
Director Advanced Research Projects Agency Architect Building 1400 Wilson Blvd. Arlington, VA 22209	3/0
Officer in Charge David W. Taylor Naval Ship Research and Development Center Annapolis Laboratory Annapolis, Maryland 21402 Attn: Mr. S. Cox, Code 2724	9/1
CDR C. E. Moore, OPNAV 233 Chief of Naval Operations, Off of the Room 5E577 Pentagon Washington, D.C. 20301	1/0
TACTEC Battelle Columbus Laboratories 505 King Avenue Columbus, Ohio 43201	1/0
Dr. Eugene C. Gritton The Rand Corporation 1700 Main Street Santa Monica, CA 90406	5/0